

# Superhydrophobic Fluorinated Carbons for the Microporous Layer of Polymer Electrolyte Fuel Cells

ジャン エネス ムハメット

<https://hdl.handle.net/2324/6787687>

---

出版情報：九州大学，2022，博士（工学），課程博士  
バージョン：  
権利関係：





# Superhydrophobic fluorinated carbon powders for improved water management in hydrogen fuel cells

E.M. Can<sup>a</sup>, A. Mufundirwa<sup>b</sup>, P. Wang<sup>c</sup>, S. Iwasaki<sup>c</sup>, T. Kitahara<sup>c,d</sup>, H. Nakajima<sup>c,d,e</sup>, M. Nishihara<sup>e</sup>, K. Sasaki<sup>c,d,e,f,g</sup>, S.M. Lyth<sup>a,f,g,h,\*</sup>

<sup>a</sup> Department of Automotive Science, Graduate School of Integrated Frontier Sciences, Kyushu University, 744 Motoooka, Nishi-ku, Fukuoka, 819-0395, Japan

<sup>b</sup> Japan Synchrotron Radiation Research Institute (JASRI)/SPRING-8, Sayo, Hyogo, 679-5198, Japan

<sup>c</sup> Department of Hydrogen Energy Systems, Graduate School of Engineering, Kyushu University, 744 Motoooka, Nishi-ku, Fukuoka, 819-0395, Japan

<sup>d</sup> Department of Mechanical Engineering, Faculty of Engineering, Kyushu University, 744 Motoooka, Nishi-ku, Fukuoka, 819-0395, Japan

<sup>e</sup> Next-Generation Fuel Cell Research Center (NEXT-FC), Kyushu University, 744 Motoooka, Nishi-ku, Fukuoka, 819-0395, Japan

<sup>f</sup> International Research Center for Hydrogen Energy, Kyushu University, 744 Motoooka, Nishi-ku, Fukuoka, 819-0395, Japan

<sup>g</sup> International Institute for Carbon-Neutral Energy Research, Kyushu University, 744 Motoooka, Nishi-ku, Fukuoka, 819-0395, Japan

<sup>h</sup> Department of Mechanical Engineering, Faculty of Engineering, University of Sheffield, Ella Armitage Building, Sheffield, S3 7RD, United Kingdom

## HIGHLIGHTS

- Fluorinated carbon nanoparticles were made and confirmed to be superhydrophobic.
- They were deposited as microporous layers onto carbon fiber gas diffusion layers.
- These electrodes were tested in polymer electrolyte membrane fuel cells.
- The I–V performance was significantly improved especially at high current density.
- This is attributed to enhanced water management due to the hydrophobic material.

## ARTICLE INFO

### Keywords:

Microporous layers  
Carbon nanomaterials  
Electrochemistry  
Water contact angle  
Fluorinated carbon  
PEFCs

## ABSTRACT

Under high current density operation, the efficiency of polymer electrolyte fuel cells (PEFCs) can dramatically decrease. This is due to water accumulation at the cathode side, preventing oxygen diffusion to the electrocatalyst. As such, effective water management is of vital importance by use of a suitable gas diffusion layer (GDL) and/or microporous layer (MPL). MPLs generally consist of carbon black as the porous electron conducting phase, and polytetrafluoroethylene (PTFE) as a hydrophobic binder. Here, we instead use superhydrophobic fluorinated carbon powder in the MPL as a novel material to decrease the required PTFE content. It is confirmed that the water contact angle of the MPL can be increased from 131° to 151° by using fluorinated carbon. Moreover, the fluorinated carbon MPL shows lower oxygen transport resistance at high humidity. Furthermore, in single fuel cell tests at various temperatures and relative humidity values, the I–V performance is significantly and consistently better than for the conventional MPL. These results confirm that fluorinated carbon is a promising new material for water management in the MPLs of PEFCs.

## 1. Introduction

Global heating, worsening air quality, and energy security issues mean that governments across the globe are striving to find alternatives to fossil fuels [1–3]. Renewable energy technologies such as wind and

solar power are in the process of revolutionizing the energy industry, but issues such as intermittency and long-term energy storage are hampering decarbonization efforts. Hydrogen could be the key to solving these issues, providing a versatile energy storage medium and fuel, with polymer electrolyte fuel cells (PEFCs) enabling direct conversion of

\* Corresponding author. Department of Automotive Science, Graduate School of Integrated Frontier Sciences, Kyushu University, 744 Motoooka, Nishi-ku, Fukuoka, 819-0395, Japan.

E-mail address: [lyth@kyudai.jp](mailto:lyth@kyudai.jp) (S.M. Lyth).

<https://doi.org/10.1016/j.jpowsour.2022.232098>

Received 9 June 2022; Received in revised form 16 August 2022; Accepted 6 September 2022

Available online 16 September 2022

0378-7753/© 2022 Elsevier B.V. All rights reserved.

hydrogen to electricity. PEFCs are electrochemical energy conversion devices where hydrogen and oxygen react to efficiently generate a voltage, and can operate with high power density [4]. Recently, PEFCs have been commercialized in fuel cell electric vehicles (FCEVs) such as the Toyota MIRAI in Japan. However, for global scale up of PEFC systems, a significant reduction in cost is necessary. This can be achieved in three ways: (i) reducing the component cost; (ii) improving system durability; or (iii) increasing system efficiency [5–8].

In PEFCs, the gas diffusion layer (GDL) is located between the catalyst layer and the flow channel. This component is primarily made of carbon fiber, and has several roles including: (i) the supply of reactant gases; (ii) the exhaust of products; (iii) electrical connectivity; and (iv) water management [9]. At the cathode side of the membrane electrode assembly (MEA), oxygen is supplied through the GDL to the catalyst layer, where water is formed via the oxygen reduction reaction (ORR). The water generated in the catalyst layer is then ideally transported back through the GDL to the flow channel, eventually leaving the system via the exhaust. However, in circumstances where high power output is required, the rate of water generation in the catalyst layer increases. This can lead to water accumulation, preventing oxygen diffusion to the platinum catalyst surface, and causing a significant voltage drop. This phenomenon is called ‘flooding’, and decreases PEFC efficiency under high current density conditions [10].

To minimize flooding and improve water management, the carbon fibers in GDLs are generally coated with a thin layer of polytetrafluoroethylene (PTFE) to render them hydrophobic. In addition, a microporous layer (MPL) is used at the interface with the catalyst layer to aid water transport [11–15]. The MPL usually consists of carbon black with a hydrophobic binder such as PTFE. In the absence of an MPL, GDLs is prone to severe flooding under high current density operation [15–17]. Therefore, the choice of an MPL with suitable properties is critical for water management in PEFCs.

There have been numerous studies on MPLs investigating the type of material used, the pore structure, the thickness, the PTFE content, and different wettability designs [1,10,11,13–26]. The PTFE content in the MPL is reported to significantly affect PEFC performance, with lower PTFE content leading to a greater likelihood of flooding. Higher PTFE content is reported to reduce the pore size, leading to lower gas permeability and thus higher diffusion losses [28]. In addition, PTFE is electronically insulating, so higher PTFE loadings can lead to increased ohmic losses [29]. As such alternatives solutions to water management in PEFCs in which the amount of PTFE used is reduced could be highly advantageous.

Fluorination is an effective method for enhancing the hydrophobic properties of carbon materials [30–32]. Fluorination of carbon can be achieved directly via heat treatment in the presence of pressurized fluorine gas. Indirect fluorination involves thermal decomposition of a fluorine source such as xenon difluoride ( $\text{XeF}_2$ ) generating fluorine radicals which react with the carbon surface. Alternatively, surface functionalization can be achieved via plasma treatment in  $\text{CF}_4$ . Direct fluorination and indirect fluorination both involve toxic gases or solvents. In addition, direct fluorination is highly exothermic, and great care must be taken over safety. Furthermore, plasma treatment can only functionalize the surface of carbon exposed to the plasma, making it difficult to apply this method to bulk carbon materials. Various related materials have been reported, including fluorinated carbon nanotubes [33–35], fluorinated carbon fibers [36–38], fluorinated graphene [39–42], and fluorinated carbon black [30,43–45]. These have been used in applications such as water-repellent sprays [46], gas sensors [47], lubricants, and lithium-ion batteries [48,49].

Fluorinated carbon materials have also been explored in PEFCs in several reports. For example, Nguyen et al. investigated fluorination of carbon fibers in the GDL via direct fluorination in fluorine gas and reported improved I–V performance in the mass diffusion limited current density region [13]. Carbon monofluoride decorated with platinum has been reported to be an effective electrocatalyst with high mass activity

in PEFCs and enhanced mass diffusion in direct methanol fuel cells (DMFCs) [50]. Similarly, fluorinated carbon decorated with platinum as a cathode catalyst has been reported to improve durability by suppressing carbon corrosion [51,52]. However, to the best of our knowledge there are no reports on the utilization of fluorinated carbons in the MPL of PEFCs.

In previous work, our group synthesized superhydrophobic fluorinated carbon nanoparticles at gram scale, using a unique solvothermal synthesis technique [27]. Here, this class of fluorinated carbon is employed as an alternative material for the MPL in PEFCs, as an attempt to improve water management and PEFC performance at high current density.

## 2. Experimental

### 2.1. Synthesis and characterization of fluorinated carbon

2 g of sodium lumps (Sigma-Aldrich, Japan) and 5 ml (8.25 g) of tridecafluorooctan-1-ol (Funakoshi Co, Ltd) were added to a 100 ml PTFE-lined pressure vessel (Flon Industry) which was sealed in a stainless-steel protective jacket. The reaction vessel was then placed in an oven at 150 °C for 24 h before being cooled completely and carefully opened. After the reaction, the product was collected and sonicated in a mixture of 50 vol% deionized water and 50 vol% ethanol for 30 min, then stirred for 24 h to remove byproducts. After this, the product was vacuum filtered using an Omnipore™ 0.2 µm membrane filter. Finally, the product was dried for 24 h in an oven at 65 °C. The final mass of product obtained was 1.53 g, corresponding to a yield of 18.5% (relative to the tridecafluorooctan-1-ol precursor).

The product was characterized by X-ray photoelectron spectroscopy (XPS, PHI 5000 Versa probe (II) ULVAC); transmission electron microscopy (JEM-2100HC); scanning electron microscopy and energy dispersive X-ray analysis (FE-SEM, JSM-7900F); nitrogen adsorption analysis (Belsorp Mini X, Microtrac MRB) and water contact angle measurement (DMS-401, Kyowa Interface Science Co., Ltd, Japan). Furthermore, thermogravimetric analysis (TGA, Rigaku Thermo plus EVO2 TG8121) was conducted in air.

### 2.2. Preparation of the MPL

Carbon black (Sigma-Aldrich, Japan) [53] MPLs (CB-MPL) and fluorinated carbon MPLs (FC-MPL) were manufactured using identical processes. An MPL slurry was prepared by adding 2 g of carbon (either CB or FC), 0.5 g of methyl cellulose pore forming agent (Fujifilm Wako Chemicals, Japan), 14 ml of deionized water (Milli-Q, 18 MΩ cm), and 0.1 ml of Triton X-100 (Sigma-Aldrich, Japan) surfactant to a 100 ml polypropylene beaker. This mixture was homogenized for 15 min at 2000 rpm (Thinky Mixer AR-100). Then, 0.059 ml (corresponding to 0.089 g) of PTFE dispersion (60 wt%, Teflon™ 30B from Polysciences, Inc) [54] was added to the mixture as a binder, followed by a second homogenization step for 15 min at 2000 rpm. To coat the MPL onto the Toray-GDL (5 wt% wetproofed TGP-H-060 Toray Paper), a 5 cm × 5 cm square of GDL was placed on a glass plate, and a 75 µm thick stainless-steel mask with 3 cm × 3 cm opening was placed on top of the GDL. The MPL slurry was then coated onto the GDL using a doctor blade, then dried at 65 °C for 1 h. Finally, the MPL-coated GDLs were heat-treated at 400 °C for 1 h under air, to sinter the PTFE binder and decompose the methyl cellulose pore forming agent as well as any remaining Triton-X surfactant. Decomposition of these materials is confirmed by TGA in Fig. S1.

In addition, free-standing MPLs were fabricated to aid with calculation of the porosity, by coating the slurry directly on a glass plate instead of a GDL, followed by the same drying and sintering steps. Several studies have reported an optimized PTFE loading in MPLs of about 20% [29,55,56]. One purpose of this study is to minimize the PTFE loading. Through trial-and-error, we determined that ~5 wt%

PTFE loading was the minimum limit required to create mechanically stable free-standing MPLs. Thus, all the MPLs investigated here have a thickness of  $\sim 35 \mu\text{m}$  and 5 wt% PTFE content. The MPL porosities were calculated from the thickness, area, mass, and density of the different components using the following equation [57]:

$$\phi = 1 - \frac{V_s}{V_{MPL}} = 1 - \frac{m_{MPL} \cdot (\omega_c/\rho_c + \omega_B/\rho_B)}{d_{MPL} \cdot A} \quad (1)$$

where  $\phi$  is the porosity of the MPL;  $V_s$  is the volume of the solid components (i.e. either PTFE and CB or PTFE and superhydrophobic fluorinated carbon (SHFC));  $V_{MPL}$  is the geometric volume of the MPL;  $m_{MPL}$  is the mass of the MPL;  $\omega_c$  is the mass fraction of the carbon component (0.95);  $\omega_B$  is the mass fraction of the PTFE binder (0.05);  $\rho_c$  is the density of the carbon component;  $\rho_B$  is the density of the PTFE binder;  $d_{MPL}$  is the thickness of the MPL; and  $A$  is the area of the MPL ( $1 \text{ cm} \times 1 \text{ cm}$ ).

### 2.3. Preparation of the membrane electrode assembly (MEA)

The catalyst ink was prepared by mixing Pt/C (TEC10E50E, lot 1019-8581, 46.8 wt% Pt, Tanaka, Japan) with 5 wt% Nafion solution (Wako, Japan), deionized water, and super-dehydrated ethanol (99.5 vol%, Wako, Japan). The catalyst ink was stirred overnight, then sonicated for 30 min just before use (SMT Corporation, Ultra Sonic Homogenizer UH-600). Nafion 212 membranes were placed onto movable-hot plate and masked, leaving an exposed area of  $1 \text{ cm}^2$ . The catalyst ink was then sprayed directly onto the Nafion membrane using pulsed spray mode from an automated spraying device (Nordson K.K., C3J), with a catalyst loading of  $0.3 \text{ mg}_{\text{Pt}}/\text{cm}^2$  and a Nafion content of 28 wt% [58], at both the anode and cathode. The resulting MEAs were finally hot pressed at  $132^\circ\text{C}$  and  $0.3 \text{ kN}$  for 180 s (Sinto Digital Press CRYPT-10).

### 2.4. Thermogravimetric analysis tests

During preparation the MPL, a slurry was prepared with methyl cellulose and Triton-X to improve the dispersibility and rheological properties for printing onto the GDL. These are assumed to decompose during heat treatment of the resulting MPL-coated GDL at  $400^\circ\text{C}$ . To confirm this, TGA was conducted on methyl cellulose and Triton-X under similar heat treatment conditions (Fig. S1).

### 2.5. Fuel cell polarization tests

Fuel cell tests were performed using a  $1 \text{ cm}^2$  active area single cell obtained from the Japanese Automotive Research Institute (JARI) with serpentine type flow fields. The performance of the different MPL-coated GDLs was investigated by measuring polarization curves at two different cell temperatures ( $45^\circ\text{C}$  and  $80^\circ\text{C}$ ). The temperature of  $80^\circ\text{C}$  was selected to reproduce conventional PEFCs operating conditions. The lower temperature of  $45^\circ\text{C}$  was selected as an extreme condition in which water condensation readily causes flooding even at lower current density, to highlight the effect of using superhydrophobic MPLs. Three different conditions of relative humidity (RH) were also tested (80%, 100%, 120%) at both the anode and cathode. To reach 120% relative humidity with a cell temperature of  $80^\circ\text{C}$ , the humidifier temperature was maintained at  $85^\circ\text{C}$ . For a cell temperature of  $45^\circ\text{C}$ , the humidifier was held at  $49^\circ\text{C}$ . Fuel cell performance tests at 120% RH and  $80^\circ\text{C}$  are not shown because of water condensation in uninsulated sections of the pipes between the cell and the humidifier ( $85^\circ\text{C}$ ), disrupting the gas flow and preventing stable cell I-V performance from being measured.

The constant volumetric flow rates were  $0.139 \text{ L/min}$  hydrogen and  $0.332 \text{ L/min}$  oxygen at anode and cathode, respectively (counter flow conditions). A fuel cell test station (AUTOPEM-CVZ01, Toyo Corporation, Japan) was used to control the humidification, cell temperature, and gas flow. Polarization curves were measured using an electrochemical interface impedance analyzer (Solartron SI-1287). Prior to the

polarization curve measurement, each cell was conditioned at  $0.6 \text{ V}$  for 5 h.

### 2.6. Air permeability tests

Through-plane (transverse) air permeability tests were conducted under ambient conditions with dry air flow, using the set up summarized in Ref. [59], applying Darcy's law (Eq. (2)): [60]

$$Q = \frac{K \cdot A \cdot \Delta P}{\mu \cdot L} \quad (2)$$

where  $Q$  is the volumetric flow rate ( $\text{m}^3\text{s}^{-1}$ );  $K$  is the air permeability ( $\text{m}^2$ );  $A$  is the area of GDL or MPL coated GDL ( $0.5 \text{ cm}^2$ );  $\Delta P$  is the pressure difference between the inlet and outlet;  $\mu$  is Newtonian viscosity ( $18.37 \text{ kgm}^{-1}\text{s}$ ); and  $L$  is the sample thickness (m). To measure air permeability, a  $1 \text{ cm} \times 1 \text{ cm}$  GDL sample was placed between two plates, each with a  $0.5 \text{ cm}^2$  diameter hole for air flow. To avoid leakage, PTFE gaskets were also used. The compression was set to  $1 \text{ MPa}$ , similar to the pressure used in PEFC polarization measurements. The air pressure was set by the volumetric flow rate to be  $1.23 \text{ kPa}$ , as suggested in the Gurley Method [61].

### 2.7. Water contact angle measurements

The water contact angles (WCAs) of the different MPLs were measured in two different ways. In the first method, the surface contact angle was measured using the pendant drop method with an automated analyzer (DMs-401, Kyowa Interface Science Co., Ltd, Japan). All GDLs have a PTFE loading of 5 wt%. Contact angles were measured using the pendant drop method. To minimize the effect of gravity, the droplet size was fixed at around  $1 \mu\text{L}$ . To measure the contact angle of the as-synthesized fluorinated carbon powder, it was first pressed between two glass plates to create a relatively smooth surface.

In the second method, the internal contact angle of the pores was measured using the set up summarized in Ref. [59], and by applying the Young-Laplace equation (Eq. (3)):

$$d = \frac{4 \cdot \sigma \cdot \cos \theta}{P_c} \quad (3)$$

where  $d$  is the pore diameter;  $\sigma$  is the surface tension of the liquid;  $\theta$  is the contact angle, and  $P_c$  is the capillary pressure. To measure the contact angle within the largest pore, first the maximum pore size of the MPL was calculated using Eq. (3). To measure the maximum pore size, samples were immersed in a low surface tension liquid (Galpore,  $\sigma = 0.0156 \text{ Nm}^{-1}$ , contact angle =  $0^\circ$ ) in a vacuum desiccator for 2 h. Then, the MPL sample was carefully removed, placed in the sample holder, and sealed with a PTFE gasket. Then, air flow was supplied through the plane of the sample, and the inlet air pressure recorded. Since the largest pore has the lowest capillary pressure, it can be assumed that this will be the first to be blown out. The pressure at which this first occurs is then used in Eq. (3) to estimate the maximum pore diameter [60]. After this maximum pore size calculation, pressurized water was then supplied to the same sample. The pressure at which water starts to flow through the largest pore of the GDL corresponds to the water breakthrough pressure. After determination of water breakthrough pressure, the contact angle of the pores can be calculated via Eq. (3). Here, the surface tension of water at  $25^\circ\text{C}$  is assumed to be  $0.0720 \text{ Nm}^{-1}$ , and samples size was  $0.5 \text{ cm}^2$ .

### 2.8. Oxygen transport resistance

The total oxygen transport resistance was calculated from the limiting current density under the differential relative humidity conditions of the supplied gasses, using the following equation [62]:

$$R_T = \frac{4 \cdot F \cdot P_{O_2}}{i_{lim} \cdot R \cdot T} \quad (4)$$

Where  $R_T$  is the total oxygen transport resistance of the cell ( $\text{sm}^{-1}$ ),  $F$  is the Faraday constant ( $96485 \text{ C mol}^{-1}$ ),  $P_{O_2}$  is the oxygen partial pressure (Pa),  $R$  is the gas constant ( $8314 \text{ J mol}^{-1}\text{K}^{-1}$ ),  $T$  is the cell temperature (K) and  $i_{lim}$  is the limiting current density at 0.2 V.

The oxygen transport resistance was calculated at both 80 °C and 45 °C cell temperature conditions for each different MPL. At high cell temperature, the oxygen transport resistance was measured at relative humidity of 80, 100, and 120%. At low cell temperature, the oxygen transport resistance was measured at 80, 100, 120, 160, and 200% relative humidity. The flow rate of the supplied gases at both the anode and cathode was 1 L/min. The oxygen concentration was 2 vol% at the cathode side, and nitrogen was used as the balance gas.

### 3. Results and discussion

#### 3.1. Material characterization

The synthesized product was a dry black powder (fluorinated carbon) mixed with a white residue, confirmed by XPS to be sodium fluoride. This NaF was almost completely removed during the washing step. When added to water, the final product was clearly highly hydrophobic, floating readily on the surface. The microstructure of the powder was investigated by SEM and TEM (Fig. 1), revealing a spheroidal microstructure similar to carbon black (Fig.S3) [17]. The nanoparticles are clustered together with a flocculent structure, leaving micron-scale voids. The TEM images show that the particles are spheroidal and solid, with most particle sizes varying between around 50 and 100 nm in diameter. These SEM and TEM images are representative, although several much larger particles around 500 nm in diameter were also observed in some images (Fig. S2).

EDX reveals a carbon content of 91.6 at.%, an oxygen content of 6.3

at.%, a fluorine content of 1.9 at.%, and a sodium content of 0.2 at.%. These results confirm that this synthesis method can be used to successfully generate fluorinated carbon with relatively high fluorine content. Fig. 2 shows representative elemental EDX mapping of the fluorinated carbon powder. The presence of fluorine is confirmed throughout the whole structure, indicating that it is uniformly bonded to the carbon atoms. Meanwhile, in some areas, fluorine and sodium signals have overlapping and high intensity signals, indicating the presence of sodium fluoride. It is likely that this sodium fluoride is encapsulated within the fluorinated carbon particles, preventing it from being removed during the washing step, as observed in our previous study [30]. Increasing the length of the washing step to 3 days had no significant effect on the sodium content. Since the sodium content is so low (0.2 at.%) and the NaF is encapsulated, its presence is not expected to have a significant impact on the initial PEFC results. However, in the case of severe carbon corrosion the effect of leaching of sodium and fluoride ions on PEFC performance should be considered. Durability will be the topic of a future study.

Nitrogen adsorption/desorption isotherms of the fluorinated carbon compared with graphitized carbon black are shown in Fig. S4. Brunauer-Emmett-Teller (BET) and Barrett-Joyner-Halenda (BJH) methods were used to calculate the specific surface area and pore size distribution. Both samples have Type III isotherms, characteristic of nonporous materials [63]. The specific surface area of the fluorinated carbon is  $40 \text{ m}^2/\text{g}$ . This is much lower compared to non-fluorinated porous carbons prepared in a similar manner and previously reported by our group [7, 45]. This is mainly attributed to the preferential formation of NaF in this case over NaOH, which acts as an activation agent in our unfluorinated carbons. Meanwhile, differences in pressure within the PTFE crucible and the viscosity of the melting precursors as they decompose may also be a factor. Furthermore, fluorination has been previously reported to decrease surface area and pore volume by blocking micropores [31]. Nevertheless, the surface area is of a similar order to that of the graphitized carbon black reference sample ( $115 \text{ m}^2/\text{g}$ ), suggesting that

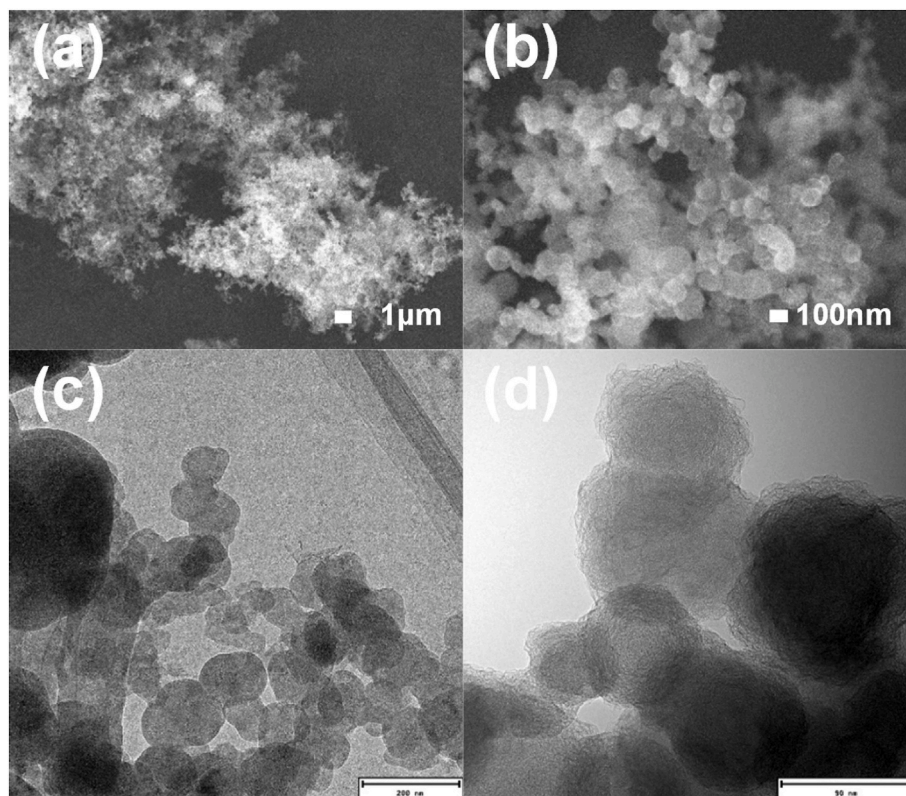


Fig. 1. Electron microscopy showing the microstructure of the fluorinated carbons used in this study: (a–b) SEM images, (c–d) TEM images.

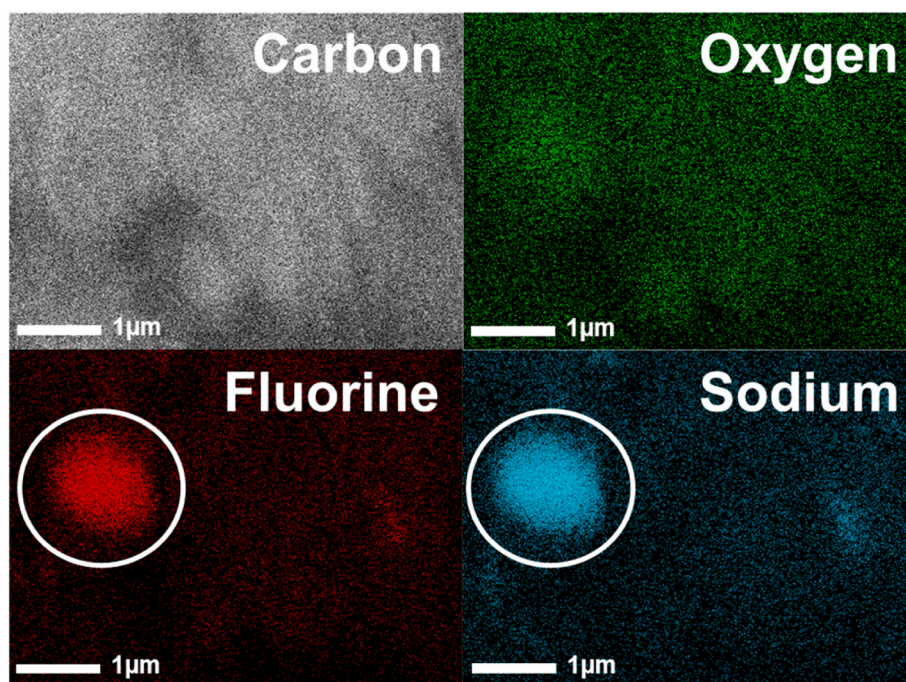


Fig. 2. EDX elemental maps of fluorinated carbon.

this relatively low surface area is not necessarily an issue for MPL-related applications. BJH results also confirm that the fluorinated carbon is non-porous. On the other hand, graphitized carbon black shows a certain pore size distribution between 20 and 100 nm. However, when compared with other porous carbon materials, graphitized carbon black can also effectively be considered as non-porous [6,46].

The skeletal density of the samples was measured by adding 5 ml of ethanol into a graduated cylinder, and then sample powder was added until the volume increased by exactly 0.1 ml. The increase in mass was measured and the density calculated by dividing this number by the volume displaced. Using this method, the skeletal density of graphitized carbon black was measured to be  $1.9 \text{ g cm}^{-3}$  which is within the range quoted by the manufacturer (i.e.  $1.5\text{--}1.9 \text{ g cm}^{-3}$ ) [64]. The density of the fluorinated carbon was measured to be  $2.04 \text{ g cm}^{-3}$ . This higher density compared to carbon black is attributed to the fact that fluorine has a higher atomic mass compared to carbon.

Assuming that the carbon particles are spherical and non-porous (as discussed in the previous paragraph), the mean particle size can be calculated using the following equation [65]:

$$L_D = 6000 / (\rho_s \cdot \alpha_{s,BET}) \quad (5)$$

Where,  $L_D$  is mean particle diameter,  $\rho_s$  is the density of the adsorbent, and  $\alpha_{s,BET}$  is the BET specific surface area. According to this equation, the mean particle diameter of carbon black 27.4 nm, in close agreement with data quoted by the manufacturer (24 nm) [53], confirming that this method is reliable. Meanwhile, the mean particle size of the fluorinated carbon sample is calculated to be 74.4 nm, which is in close agreement with the particle size observed in the SEM and TEM images (Fig. 1.).

XPS analysis of the fluorinated carbon (Fig. 3) confirms the presence of carbon at 284.5 eV (88.5 at.%), fluorine at 688 eV (9.8 at.%), oxygen at 532 eV (1.5 at.%), and trace amounts of sodium at 1073 eV (0.2 at.%). Two F KLL Auger peaks are also observed at 632 eV and 658 eV. The C1s narrow scan spectrum is deconvoluted into peaks corresponding to:  $\text{sp}^2$  carbon at 284.5 eV;  $\text{sp}^3$  carbon bond at 285.2 eV; C–O bonds at 287.5 eV; C–F bonds at 289.6 eV;  $\text{CF}_2$  bonds at 291.5 eV; and  $\text{CF}_3$  bonds (or C 1s shake-up) at 294.0 eV [32–36]. The F1s spectrum is deconvoluted into covalently bonded fluorine at 688.5 eV and 692.0 eV [66]. The O1s spectrum is deconvoluted into two main peaks corresponding to C–O

bonds at 532.5 eV, and possibly a sodium auger peak at 537.5 eV. Finally, the Na 1s spectrum can be fitted by a single peak at 1072.4 eV, corresponding to sodium-fluorine bonds. This analysis confirms that fluorine atoms were successfully covalently doped into the carbon structure.

The atomic concentration of fluorine obtained from XPS analysis (9.8 at.%) is significantly higher than that measured by EDX (1.9 at.%). This discrepancy is attributed to the fact that XPS is a quasi-surface sensitive analysis technique with a penetration depth of  $\sim 5\text{--}10 \text{ nm}$ , and EDX is a bulk measurement technique with a penetration depth of  $1\text{--}2 \mu\text{m}$ . The difference in measured values can be explained by the fact that the fluorination mostly occurs near the surface of the carbon, so XPS detects a high fluorine content, but EDX detects the average fluorine content throughout the whole sample, which is much lower. This may be advantageous for electronic applications. Since fluorine is a highly electronegative element, high levels of fluorine doping are expected to dramatically decrease the electronic conductivity of carbon. However, surface fluorination means that the bulk carbon retains high conductivity whilst the surface can take on the advantageous hydrophobic properties. This is especially important in the MPL in which high electrical conductivity is required. Furthermore, the oxygen content is higher according to EDX (6.3 at.%) compared to XPS (1.5 at.%). Again, this suggests that oxygen is not concentrated at the surface, as would be expected for hydrophilic surface functional groups or adsorbed water. As such, the oxygen content should not significantly affect the hydrophobicity of the material.

Fig. 4 shows thermogravimetric analysis (TGA) of the fluorinated carbon sample and graphitized carbon black, measured under constant air flow. The results show that the fluorinated carbon is thermally stable in air up until  $500^\circ\text{C}$ , above which the material decomposes. Graphitized carbon black has slightly higher thermal stability, attributed to the lower thermodynamic stability of covalent C–F bonds compared to the C=C bonds in graphitized carbon black [31]. This confirms that this fluorinated carbon is resilient to thermal decomposition at typical temperatures used in PEFCs.

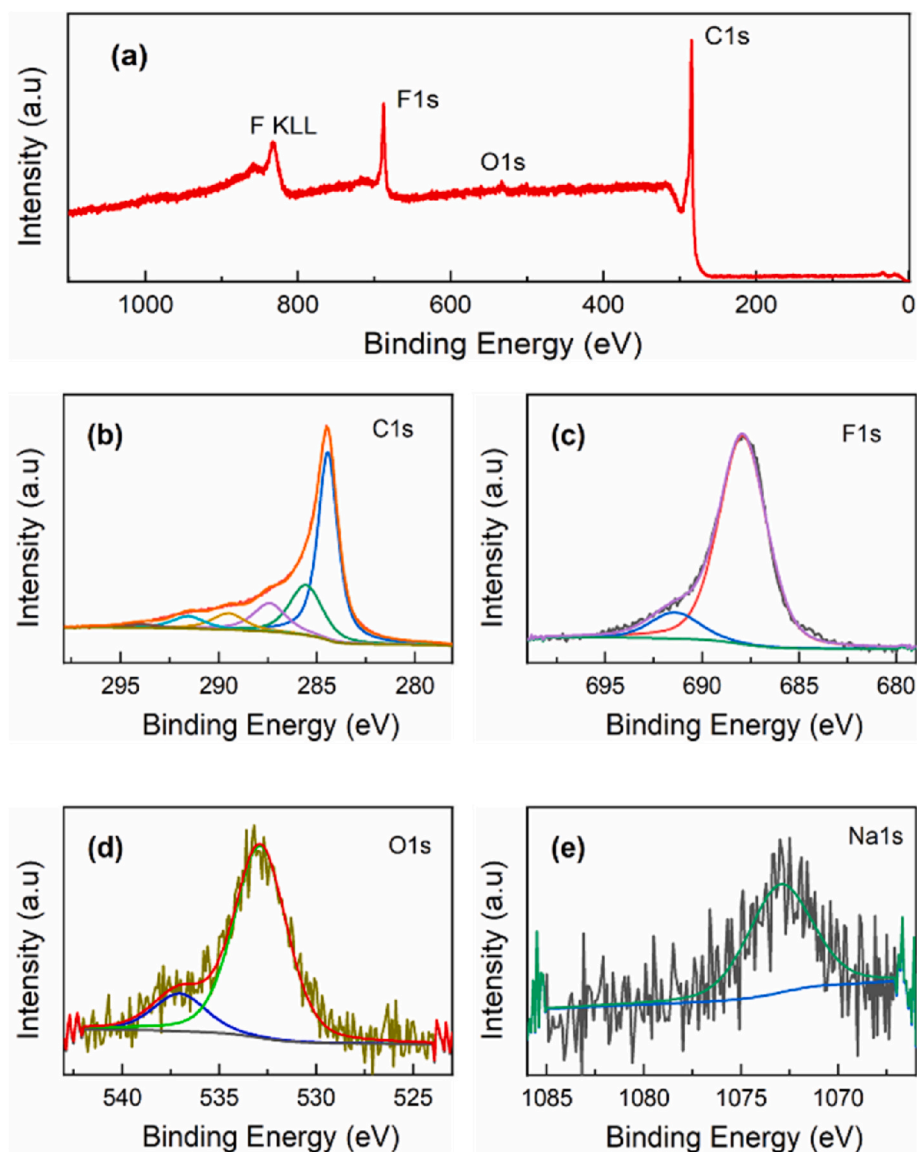


Fig. 3. XPS of the fluorinated carbon sample: (a) survey spectrum; (b) C 1s; (c) F 1s; (d) O 1s; and (e) Na 1s regions.

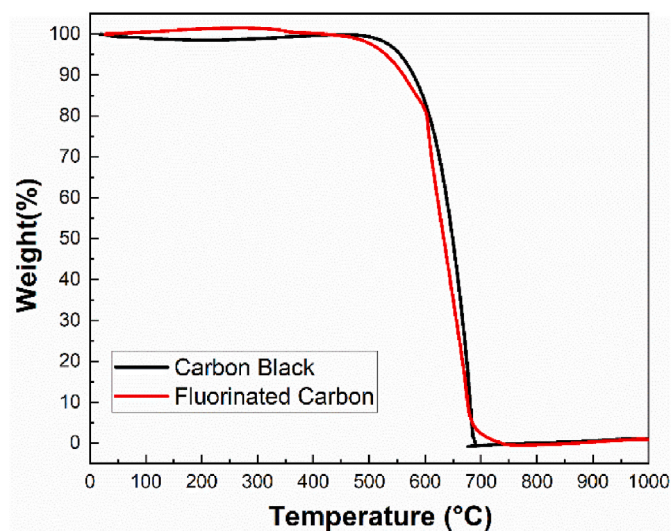


Fig. 4. TGA of fluorinated carbon and graphitized carbon black in air.

### 3.2. Microporous layer characterization

The different microstructures of MPLs fabricated using fluorinated carbon (FC-MPL) and graphitized carbon black (CB-MPL) were investigated by SEM (Fig. 5). In both cases, pores of several microns in size are observed, which is attributed to decomposition of the methyl cellulose pore forming agent, as expected. Meanwhile, the surface of the CB-MPL appears to be relatively smooth and uniform compared to that of the FC-MPL. This is attributed to the smaller particle diameter.

To confirm if fluorination of carbon can affect the water repelling properties of the resulting MPLs, the water contact angle (WCA) was measured and compared with other MPL-coated GDLs (Fig. 6). The WCA of the as-synthesized fluorinated carbon sample (FC) after pressing is  $160^\circ$ , confirming that the synthesized material is indeed super-hydrophobic (i.e.  $\theta > 150^\circ$ ). After incorporating the fluorinated carbon into an MPL (FC-MPL), the WCA is  $151^\circ$  (Fig. 6 (b)). This slight decrease is attributed to the effect of residual pore forming agent (methyl cellulose) added during slurry preparation, which does not completely decompose during the heating step (see TGA, Fig S3). Meanwhile, the WCA of the identically prepared CB-MPL is much lower at  $131^\circ$  (Fig. 6 (c)). Finally, the WCA of a commercial Toray-GDL (TGP-H-060, Toray,

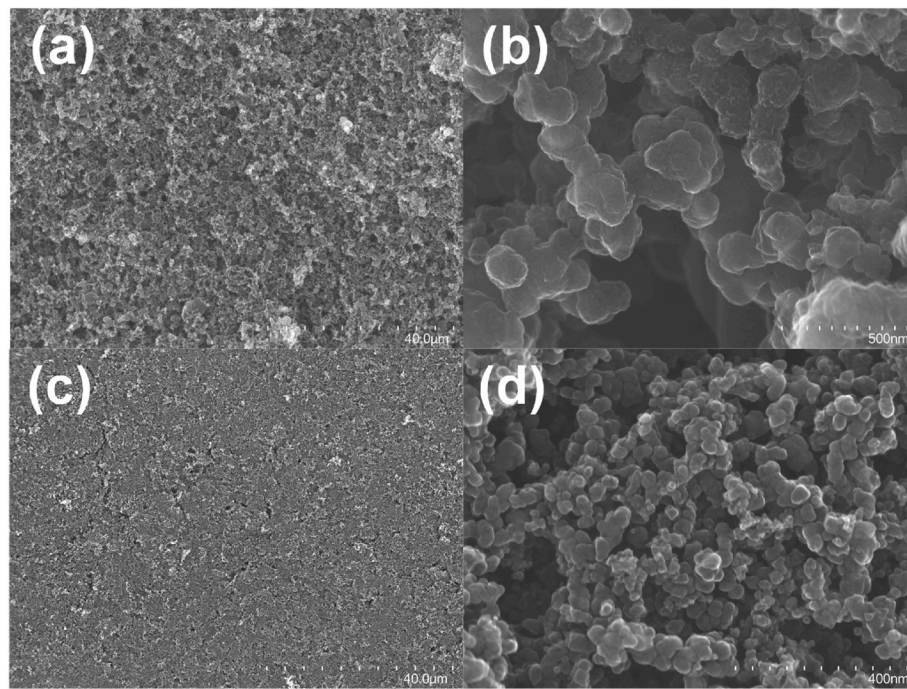


Fig. 5. SEM images of MPL surface at different magnifications: (a–b) FC-MPL; (c–d) CB-MPL.

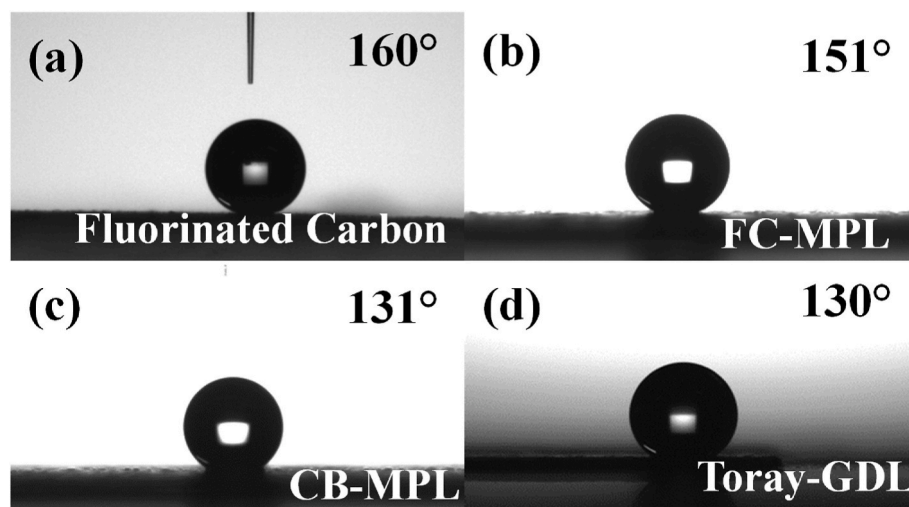


Fig. 6. Surface water contact angle (WCA) measurements for: (a) pressed fluorinated carbon (FC); (b) FC-MPL; (c) CB-MPL; and (d) Toray-GDL (TGP-H-060).

Japan) was measured to be  $130^\circ$  (Fig. 6 (d)). These results confirm that the high WCA of the fluorinated carbon translates to significantly improved WCA in MPLs incorporating this material. The results also suggest that the WCA of the MPL is not dominated by the presence of the PTFE binder when the PTFE loading is sufficiently low (e.g. 5 wt%), but mainly instead on the properties of the carbon itself. This may not be the case for higher PTFE loading.

Porosity is an important factor which affects mass transport resistance significantly. When porosity is increased, the total resistance to molecular diffusion in the system decreases. Here, the porosities of the free-standing FC-MPL and CB-MPL samples were calculated according to Eq. (1) to be 76% and 83%, respectively, and the maximum pore diameters were similar at  $42.5$  and  $40.5$   $\mu\text{m}$  (Fig. 7(a)). Meanwhile, Toray-GDL had a larger maximum diameter of  $61.7$   $\mu\text{m}$ , primarily because it does not include an MPL, exposing the larger pores defined by the spaces between carbon fibers.

The experimentally determined WCA above can be described as the *apparent contact angle*, which is dependent on both the surface interaction energy and the surface roughness of the sample. Once the maximum pore size has been determined, *Young's contact angle* can be estimated using the Young-Laplace Equation (Eq. (3)), and this value is independent of the surface roughness. Especially in this composite material, the Young's contact angle is an important parameter to confirm to what extent the apparent contact angle is due to the hydrophobic nature of the fluorinated carbon and what extent to the surface roughness. Both the Toray-GDL and the CB-MPL have similar Young's WCA of around  $130^\circ$  (Fig. 7(b)), consistent with the surface WCA measurement, and in agreement with prior studies [13]. In contrast, the Young's WCA for the FC-MPL is much higher at  $151^\circ$ . This agrees with the apparent WCA, confirming that the superhydrophobic nature of these MPLs is due to the nature of the material, rather than any change in surface roughness.

The through-plane air permeability was also measured (Fig. 7(c)).

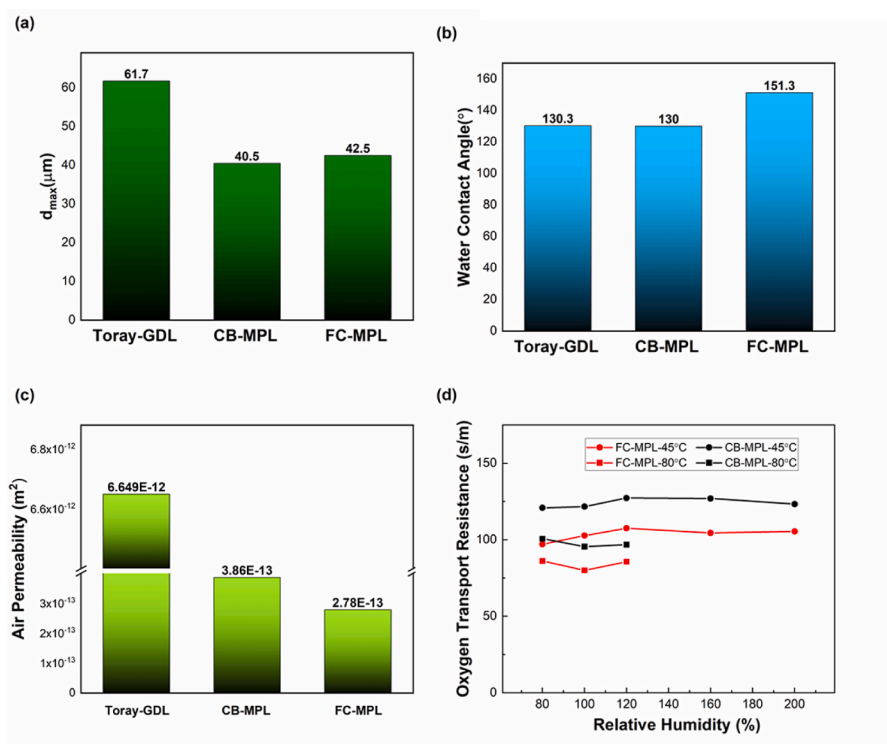


Fig. 7. (a) Maximum pore diameter; (b) internal water contact angle; (c) air permeability; and (d) oxygen transport resistance for Toray-GDL, CB-MPL and FC-MPL.

FC-MPL has the lowest permeability, and CB-MPL has slightly higher permeability. Since the maximum pore diameter and the thickness of the CB-MPL and the FC-MPL are similar, the lower air permeability in FC-MPL may be the result of higher tortuosity due to lower porosity, and/or the smaller mean pore diameter. In contrast, the air permeability of Toray-GDL is over an order of magnitude higher, due to the much larger pores in the absence of an MPL. These results show that the air permeability is dominated by the MPL rather than the GDL.

Meanwhile, the oxygen transport resistance through the MPL-coated GDLs was measured in situ in a PEFC single cell (Fig. 7(d)), as summarized in the experimental section. The results clearly show that the FC-MPL has significantly lower oxygen transport resistance compared to CB-MPL. For example, the oxygen transport resistance for the CB-MPL was measured to be 125 s/m at 80 °C and 100 s/m at 45 °C, compared to 105 s/m and 85 s/m for the FC-MPL under the same conditions. This is attributed to the superior water-repellent characteristics of FC-MPL, resulting in a faster rate of water removal. In all cases, the total oxygen transport resistance does not significantly vary with relative humidity, indicating that water accumulation in the MPL-coated GDLs and the catalyst layers does not change significantly under high humidity conditions [59,67].

### 3.3. Single cell characterization

Finally, PEFCs were fabricated incorporating the FC-MPL, and compared to identically prepared cells using the CB-MPL, at cell temperatures of 45 °C and 80 °C. At 45 °C, the performance of the cell was measured at 80, 100 and 120% RH, whilst at 80 °C the cell was measured at 80 and 100% RH.

The IR-free polarization curves reveal a clear difference in the mass diffusion limited current density region between the two MPLs, regardless of measurement temperature, with the FC-MPL cell having significantly higher cell voltage compared to the CB-MPL (Fig. 8(a and b)). For example, at 80 °C and 80% RH, the limiting current densities were measured to be 1.61 A/cm<sup>2</sup> and 1.72 A/cm<sup>2</sup> for the CB-MPL and the FC-MPL, respectively. Similarly, at 45 °C and 80% the limiting

current densities were measured to be ~1.03 A/cm<sup>2</sup> and 1.14 A/cm<sup>2</sup>, respectively. This high current density region is where flooding normally occurs and disrupts oxygen diffusion to the catalyst surface, resulting in the observed voltage drop. However, the use of superhydrophobic fluorinated carbon in the MPL appears to improve removal of water from the cathode side of the cell, suppressing this voltage drop. This is confirmed and highlighted when the concentration overvoltage is separated from the polarization curves (Fig. 8(c and d)).

Furthermore, when the ohmic regions of the polarization curves are compared, there is little difference between FC-MPL and CB-MPL (Fig. 8(e and f)). This indicates that the doping of electronegative fluorine atoms into the carbon structure does not significantly lower the electronic conductivity of the material, and therefore that ohmic losses can be avoided. As discussed in the elemental analysis section, this may be because the fluorine atoms are mainly concentrated at the surface of the carbon nanoparticles rather than throughout the bulk.

The effect of humidity on the polarization curves was also investigated. At the relatively low temperature of 45 °C, the limiting current density does not change significantly with increasing humidity for either MPL-coated GDL. This may be because the amount of water which condenses at the cathode side of the cell does not change significantly between 80 and 120% RH (as also inferred from oxygen transport resistance test results in Fig. 7(d)). Meanwhile, at higher cell temperature (80 °C), there is a clear decrease in cell voltage as the relative humidity increase, especially in the mass diffusion limited current density region. This is attributed to a greater degree of water condensation at the cathode side of the cell at higher humidity, resulting in flooding and a corresponding voltage drop due to restriction of oxygen supply to the catalyst.

## 4. Conclusions

In this paper, superhydrophobic fluorinated carbon nanoparticles were uniquely synthesized from fluorinated alcohol. The resulting superhydrophobic fluorinated carbon powder had similar microstructure and morphology to commercially available carbon black, but with a

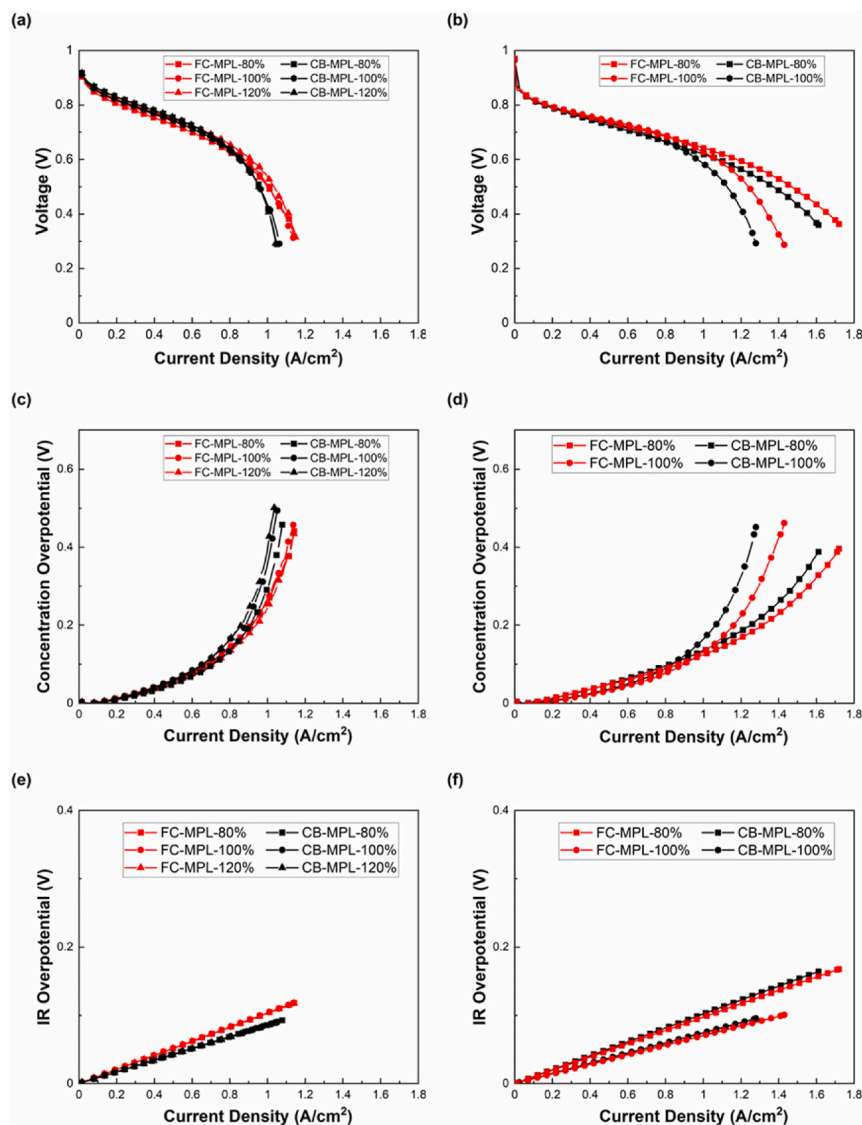


**Fig. 8.** Single cell PEFC measurements under different relative humidity conditions. Polarization curves (IR-free) at cell temperatures of (a) 45 °C and (b) 80 °C. Concentration overvoltage at (c) 45 °C (d) 80 °C. IR overpotential at (e) 45 °C and (f) 80 °C.

fluorine content of 1.9 at.%. This powder was applied to a GDL to create a superhydrophobic MPL with a water contact angle of 151°, despite the relatively low PTFE loading of 5 wt%. The FC-MPL displayed reproducibly superior I–V performance in a fuel cell at high current density. For example, at 80 °C and 80% RH the limiting current density was 1.61 A/cm<sup>2</sup> for the carbon black-based MPL, increasing to 1.72 A/cm<sup>2</sup> for the FC-MPL. These improvements in performance are attributed to lower oxygen transport resistance in the case of the FC-MPL (105 s/m at 80 °C) compared to CB-MPL (125 s/m at 80 °C). Therefore, the improved I–V performance is directly attributed to enhanced water removal from the microporous layer due to the superhydrophobic nature of the fluorinated carbon. This work is expected to result in the design of more efficient PEFCs which can operate at higher current density, with lower PTFE content.

#### Declaration of competing interest

The authors declare that they have no known competing financial interests or personal relationships that could have appeared to influence the work reported in this paper.

#### Data availability

Data will be made available on request.

#### Acknowledgements

Part of this study was supported by NEDO (Contract No. JPNP20003). Enes Muhammet Can acknowledges the Ph.D. scholarship funding provided by the Ministry of Education of Türkiye.

#### Appendix A. Supplementary data

Supplementary data to this article can be found online at <https://doi.org/10.1016/j.jpowsour.2022.232098>.

#### References

- [1] T. Abbasi, S.A. Abbasi, Is the use of renewable energy sources an answer to the problems of global warming and pollution? *Crit. Rev. Environ. Sci. Technol.* 42 (2012) 99–154, <https://doi.org/10.1080/10643389.2010.498754>.
- [2] S. Bilgen, S. Keleş, A. Kaygusuz, A. Sari, K. Kaygusuz, Global warming and renewable energy sources for sustainable development: a case study in Turkey,

- Renew. Sustain. Energy Rev. 12 (2008) 372–396, <https://doi.org/10.1016/j.rser.2006.07.016>.
- [3] I. Yüksel, Global warming and renewable energy sources for sustainable development in Turkey, *Renew. Energy* 33 (2008) 802–812, <https://doi.org/10.1016/j.renene.2007.05.040>.
  - [4] K. Sasaki, H.-W. Li, A. Hayashi, J. Yamabe, T. Ogura, *Hydrogen Energy Engineering*, 2016, <https://doi.org/10.1007/978-4-431-56042-5>.
  - [5] J.O. Park, K. Kwon, M.D. Cho, S.-G. Hong, T.Y. Kim, D.Y. Yoo, Role of binders in high temperature PEMFC electrode, *J. Electrochem. Soc.* 158 (2011) B675, <https://doi.org/10.1149/1.3573773>.
  - [6] S.M. Lyth, *Doped and Decorated Carbon Foams for Energy Applications*, Springer International Publishing, 2019, [https://doi.org/10.1007/978-3-319-92917-0\\_8](https://doi.org/10.1007/978-3-319-92917-0_8).
  - [7] A. Mufundirwa, G.F. Harrington, B. Smid, B.V. Cunnings, K. Sasaki, S.M. Lyth, Durability of template-free Fe-N-C foams for electrochemical oxygen reduction in alkaline solution, *J. Power Sources* 375 (2018) 244–254, <https://doi.org/10.1016/j.jpowsour.2017.07.025>.
  - [8] M. Breitwieser, T. Bayer, A. Büchler, R. Zengerle, S.M. Lyth, S. Thiele, A fully spray-coated fuel cell membrane electrode assembly using Aquivion ionomer with a graphene oxide/cerium oxide interlayer, *J. Power Sources* 351 (2017) 145–150, <https://doi.org/10.1016/j.jpowsour.2017.03.085>.
  - [9] P.T. Moseley, *Fuel Cell Systems Explained*, 2001, [https://doi.org/10.1016/s0378-7753\(00\)00571-1](https://doi.org/10.1016/s0378-7753(00)00571-1).
  - [10] H. Li, Y. Tang, Z. Wang, Z. Shi, S. Wu, D. Song, J. Zhang, K. Fatih, J. Zhang, H. Wang, Z. Liu, R. Abouatallah, A. Mazza, A review of water flooding issues in the proton exchange membrane fuel cell, *J. Power Sources* 178 (2008) 103–117, <https://doi.org/10.1016/j.jpowsour.2007.12.068>.
  - [11] U. Pasaogullari, C.Y. Wang, Two-phase transport and the role of micro-porous layer in polymer electrolyte fuel cells, *Electrochim. Acta* 49 (2004) 4359–4369, <https://doi.org/10.1016/j.electacta.2004.04.027>.
  - [12] M.S. Ismail, T. Damjanovic, D.B. Ingham, M. Pourkashanian, A. Westwood, Effect of polytetrafluoroethylene-treatment and microporous layer-coating on the electrical conductivity of gas diffusion layers used in proton exchange membrane fuel cells, *J. Power Sources* 195 (2010) 2700–2708, <https://doi.org/10.1016/j.jpowsour.2009.11.069>.
  - [13] T. Van Nguyen, A. Aghosseini, X. Wang, V. Yarlagadda, A. Kwong, A.Z. Weber, P. Deevanhay, S. Tushima, S. Hirai, Hydrophobic gas-diffusion media for polymer-electrolyte fuel cells by direct fluorination, *J. Electrochem. Soc.* 162 (2015) F1451, <https://doi.org/10.1149/2.041151jes>. –F1460.
  - [14] J. Zhang, B. Wang, J. Jin, S. Yang, G. Li, A review of the microporous layer in proton exchange membrane fuel cells: materials and structural designs based on water transport mechanism, *Renew. Sustain. Energy Rev.* 156 (2022), 111998, <https://doi.org/10.1016/j.rser.2021.111998>.
  - [15] R. Lin, X. Yu, L. Chen, S. Tang, X. Yin, Z. Hao, Structure majorization on the surface of microporous layer in polymer electrolyte membrane fuel cells to optimize performance and durability, *Energy Convers. Manag.* 243 (2021), 114319, <https://doi.org/10.1016/j.enconman.2021.114319>.
  - [16] L. Chen, R. Lin, S. Tang, D. Zhong, Z. Hao, Structural design of gas diffusion layer for proton exchange membrane fuel cell at varying humidification, *J. Power Sources* 467 (2020), 228355, <https://doi.org/10.1016/j.jpowsour.2020.228355>.
  - [17] Y. Tabe, Y. Aoyama, K. Kadowaki, K. Suzuki, T. Chikahisa, Impact of micro-porous layer on liquid water distribution at the catalyst layer interface and cell performance in a polymer electrolyte membrane fuel cell, *J. Power Sources* 287 (2015) 422–430, <https://doi.org/10.1016/j.jpowsour.2015.04.095>.
  - [18] F. Aldakheel, M.S. Ismail, K.J. Hughes, D.B. Ingham, L. Ma, M. Pourkashanian, D. Cumming, R. Smith, Gas permeability, wettability and morphology of gas diffusion layers before and after performing a realistic ex-situ compression test, *Renew. Energy* 151 (2020) 1082–1091, <https://doi.org/10.1016/j.renene.2019.11.109>.
  - [19] O.M. Orogbeni, D.B. Ingham, M.S. Ismail, K.J. Hughes, L. Ma, M. Pourkashanian, On the gas permeability of the microporous layer used in polymer electrolyte fuel cells, *J. Energy Inst.* 91 (2018) 894–901, <https://doi.org/10.1016/j.joei.2017.09.006>.
  - [20] M.S. Ismail, D. Borman, T. Damjanovic, D.B. Ingham, M. Pourkashanian, On the through-plane permeability of microporous layer-coated gas diffusion layers used in proton exchange membrane fuel cells, *Int. J. Hydrogen Energy* 36 (2011) 10392–10402, <https://doi.org/10.1016/j.ijhydene.2010.09.012>.
  - [21] O.M. Orogbeni, D.B. Ingham, M.S. Ismail, K.J. Hughes, L. Ma, M. Pourkashanian, The effects of the composition of microporous layers on the permeability of gas diffusion layers used in polymer electrolyte fuel cells, *Int. J. Hydrogen Energy* 41 (2016) 21345–21351, <https://doi.org/10.1016/j.ijhydene.2016.09.160>.
  - [22] C. Simon, D. Kartouzian, D. Müller, F. Wilhelm, H.A. Gasteiger, Impact of microporous layer pore properties on liquid water transport in PEM fuel cells: carbon black type and perforation, *J. Electrochem. Soc.* 164 (2017) F1697, <https://doi.org/10.1149/2.132171jes>. –F1711.
  - [23] C.M. Long, M.A. Nascarella, P.A. Valberg, Carbon black vs. black carbon and other airborne materials containing elemental carbon: physical and chemical distinctions, *Environ. Pollut.* 181 (2013) 271–286, <https://doi.org/10.1016/j.envpol.2013.06.009>.
  - [24] J.T. Gostick, M.A. Ioannidis, M.W. Fowler, M.D. Pritzker, On the role of the microporous layer in PEMFC operation, *Electrochem. Commun.* 11 (2009) 576–579, <https://doi.org/10.1016/j.elecom.2008.12.053>.
  - [25] C. Li, D. Si, Y. Liu, J. Zhang, Y. Liu, Water management characteristics of electrospun micro-porous layer in PEMFC under normal temperature and cold start conditions, *Int. J. Hydrogen Energy* 46 (2021) 11150–11159, <https://doi.org/10.1016/j.ijhydene.2020.05.271>.
  - [26] C.J. Tseng, S.K. Lo, Effects of microstructure characteristics of gas diffusion layer and microporous layer on the performance of PEMFC, *Energy Convers. Manag.* 51 (2010) 677–684, <https://doi.org/10.1016/j.enconman.2009.11.011>.
  - [27] A.T. Najafabadi, M.J. Leeuwener, D.P. Wilkinson, E.L. Gyenge, Electrochemically produced graphene for microporous layers in fuel cells, *ChemSusChem* 9 (2016) 1689–1697, <https://doi.org/10.1002/cssc.201600351>.
  - [28] G. Lin, T. Van Nguyen, Effect of thickness and hydrophobic polymer content of the gas diffusion layer on electrode flooding level in a PEMFC, *J. Electrochem. Soc.* 152 (2005) A1942, <https://doi.org/10.1149/1.2006487>.
  - [29] M.S. Ismail, K.J. Hughes, D.B. Ingham, L. Ma, M. Pourkashanian, Effect of PTFE loading of gas diffusion layers on the performance of proton exchange membrane fuel cells running at high-efficiency operating conditions, *Int. J. Energy Res.* 37 (2013) 1592–1599, <https://doi.org/10.1002/er.2968>.
  - [30] S.M. Lyth, W. Ma, J. Liu, T. Daio, K. Sasaki, A. Takahara, B. Ameduri, Solvothermal synthesis of superhydrophobic hollow carbon nanoparticles from a fluorinated alcohol, *Nanoscale* 7 (2015) 16087–16093, <https://doi.org/10.1039/c5nr03484a>.
  - [31] O.V. Boltalina, T. Nakajima, *New Fluorinated Carbons: Fundamentals and Applications Progress in Fluorine Science Series*, 2016, <https://doi.org/10.1016/C2014-0-04885-X>.
  - [32] C. Te Hsieh, W.Y. Chen, F.L. Wu, Fabrication and superhydrophobicity of fluorinated carbon fabrics with micro/nanoscaled two-tier roughness, *Carbon N.Y.* 46 (2008) 1218–1224, <https://doi.org/10.1016/j.carbon.2008.04.026>.
  - [33] E.T. Mickelson, C.B. Huffman, A.G. Rinzier, R.E. Smalley, R.H. Hauge, J. L. Margrave, Fluorination of single-wall carbon nanotubes, *Chem. Phys. Lett.* 296 (1998) 188–194, [https://doi.org/10.1016/S0009-2614\(98\)01026-4](https://doi.org/10.1016/S0009-2614(98)01026-4).
  - [34] N.O.V. Plank, L. Jiang, R. Cheung, Fluorination of carbon nanotubes in CF<sub>4</sub> plasma, *Appl. Phys. Lett.* 83 (2003) 2426–2428, <https://doi.org/10.1063/1.1611621>.
  - [35] M. Adamska, U. Narkiewicz, Fluorination of carbon nanotubes – A review, *J. Fluor. Chem.* 200 (2017) 179–189, <https://doi.org/10.1016/j.jfluchem.2017.06.018>.
  - [36] Y.S. Lee, *Synthesis and Characterization of Fluorinated Carbon Fibers and Nanotubes*, Elsevier Inc., 2017, <https://doi.org/10.1016/B978-0-12-803479-8.00006-1>.
  - [37] S.J. Park, M.K. Seo, Y.S. Lee, Surface characteristics of fluorine-modified PAN-based carbon fibers, *Carbon N.Y.* 41 (2003) 723–730, [https://doi.org/10.1016/S0008-6223\(02\)00384-6](https://doi.org/10.1016/S0008-6223(02)00384-6).
  - [38] F. Chamsseddine, M. Dubois, K. Guérin, J. Giraudet, F. Masin, D.A. Ivanov, L. Vidal, R. Yazami, A. Hamwi, Reactivity of carbon nanofibers with fluorine gas, *Chem. Mater.* 19 (2007) 161–172, <https://doi.org/10.1021/cm061731m>.
  - [39] W. Kang, S. Li, Preparation of fluorinated graphene to study its gas sensitivity, *RSC Adv.* 8 (2018) 23459–23467, <https://doi.org/10.1039/C8RA03451F>.
  - [40] B. Shen, J. Chen, X. Yan, Q. Xue, Synthesis of fluorine-doped multi-layered graphene sheets by arc-discharge, *RSC Adv.* 2 (2012) 6761–6764, <https://doi.org/10.1039/c2ra20593a>.
  - [41] A. Hamwi, M. Daoud, J.C. Cousseins, Graphite fluorides prepared at room temperature 1. Synthesis and characterization, *Synth. Met.* 26 (1988) 89–98, [https://doi.org/10.1016/0379-6779\(88\)90338-4](https://doi.org/10.1016/0379-6779(88)90338-4).
  - [42] B. Wang, J. Wang, J. Zhu, Fluorination of graphene: a spectroscopic and microscopic study, *ACS Nano* 8 (2014) 1862–1870, <https://doi.org/10.1021/nm406333f>.
  - [43] G. Nansé, E. Papirer, P. Fioux, F. Moguet, A. Tressaud, Fluorination of carbon blacks: an X-ray photoelectron spectroscopy study: I. A literature review of XPS studies of fluorinated carbons. XPS investigation of some reference compounds, *Carbon N.Y.* 35 (1997) 175–194, [https://doi.org/10.1016/S0008-6223\(96\)00095-4](https://doi.org/10.1016/S0008-6223(96)00095-4).
  - [44] N. Watanabe, Y. Kita, O. Mochizuki, Fluorination of carbon black, *Carbon N.Y.* 17 (1979) 359–363, [https://doi.org/10.1016/0008-6223\(79\)90009-5](https://doi.org/10.1016/0008-6223(79)90009-5).
  - [45] K. Guérin, M. Dubois, A. Houdayer, A. Hamwi, Applicative performances of fluorinated carbons through fluorination routes: a review, *J. Fluor. Chem.* 134 (2012) 11–17, <https://doi.org/10.1016/j.jfluchem.2011.06.013>.
  - [46] C.A.S. Hall, K.A. Klitgaard, *Energy and the Wealth of Nations: Understanding the Biophysical Economy*, 2012, <https://doi.org/10.1007/978-1-4419-9398-4>.
  - [47] J.S. Im, S.C. Kang, S.H. Lee, Y.S. Lee, Improved gas sensing of electrospun carbon fibers based on pore structure, conductivity and surface modification, *Carbon N.Y.* 48 (2010) 2573–2581, <https://doi.org/10.1016/j.carbon.2010.03.045>.
  - [48] Z. Fang, Y. Peng, X. Zhou, L. Zhu, Y. Wang, X. Dong, Y. Xia, Fluorinated carbon materials and the applications in energy storage systems, *ACS Appl. Energy Mater.* (2021), <https://doi.org/10.1021/acsaem.1c03476>.
  - [49] Q. Zhang, K.J. Takeuchi, E.S. Takeuchi, A.C. Marschillok, Progress towards high-power Li/CF<sub>x</sub> batteries: electrode architectures using carbon nanotubes with CF<sub>x</sub>, *Phys. Chem. Chem. Phys.* 17 (2015) 22504–22518, <https://doi.org/10.1039/c5cp03217b>.
  - [50] F.A. Viva, G.A. Olah, G.K.S. Prakash, Characterization of Pt supported on commercial fluorinated carbon as cathode catalysts for Polymer Electrolyte Membrane Fuel Cell, *Int. J. Hydrogen Energy* 42 (2017) 15054–15063, <https://doi.org/10.1016/j.ijhydene.2017.04.255>.
  - [51] J.L. Bott-Neto, T. Asset, F. Maillard, L. Dubau, Y. Ahmad, K. Guérin, S. Berthon-Fabry, A. Mosdale, R. Mosdale, E.A. Ticianelli, M. Chatenet, Utilization of graphitized and fluorinated carbon as platinum nanoparticles supports for application in proton exchange membrane fuel cell cathodes, *J. Power Sources* 404 (2018) 28–38, <https://doi.org/10.1016/j.jpowsour.2018.10.004>.
  - [52] S. Berthon-Fabry, L. Dubau, Y. Ahmad, K. Guérin, M. Chatenet, First insight into fluorinated Pt/carbon aerogels as more corrosion-resistant electrocatalysts for proton exchange membrane fuel cell cathodes, *Electrocatalysis* 6 (2015) 521–533, <https://doi.org/10.1007/s12678-015-0267-9>.

- [53] Carbon black CP 1333-86-4. <https://www.sigmaaldrich.com/JP/en/product/saj/051530>. (accessed July 28, 2022).
- [54] Polytetrafluoroethylene (Teflon<sup>TM</sup> 30B) 60 wt % Dispersion. <https://www.polysciences.com/india/poly-teflon-30b> (accessed July 28, 2022).
- [55] C. Simon, D. Kartouzian, D. Müller, F. Wilhelm, H.A. Gasteiger, Impact of microporous layer pore properties on liquid water transport in PEM fuel cells: carbon black type and perforation, *J. Electrochem. Soc.* 164 (2017) F1697, <https://doi.org/10.1149/2.1321714jes>. –F1711.
- [56] C. Simon, J. Endres, B. Nefzger-Loders, F. Wilhelm, H.A. Gasteiger, Interaction of pore size and hydrophobicity/hydrophilicity for improved oxygen and water transport through microporous layers, *J. Electrochem. Soc.* 166 (2019), <https://doi.org/10.1149/2.1111913jes>. F1022–F1035.
- [57] L. Cindrella, A.M. Kannan, J.F. Lin, K. Saminathan, Y. Ho, C.W. Lin, J. Wertz, Gas diffusion layer for proton exchange membrane fuel cells-A review, *J. Power Sources* 194 (2009) 146–160, <https://doi.org/10.1016/j.jpowsour.2009.04.005>.
- [58] M. Okumura, Z. Noda, J. Matsuda, Y. Tachikawa, M. Nishihara, S.M. Lyth, A. Hayashi, K. Sasaki, Correlating cathode microstructure with PEFC performance using FIB-SEM and TEM, *J. Electrochem. Soc.* 164 (2017) F928, <https://doi.org/10.1149/2.0581709jes>. –F934.
- [59] T. Kitahara, H. Nakajima, Microporous layer-coated gas diffusion layer to reduce oxygen transport resistance in a polymer electrolyte fuel cell under high humidity conditions, *Int. J. Hydrogen Energy* 41 (2016) 9547–9555, <https://doi.org/10.1016/j.ijhydene.2016.04.117>.
- [60] M.F. Mathias, J. Roth, J. Fleming, W. Lehnert, Diffusion media materials and characterisation, *Handb. Fuel Cells* (2010), <https://doi.org/10.1002/9780470974001.f303046>.
- [61] J.I.S.C.P. and board D. of air permeance-G. method J.P. 8117, *GURLEY Method for Air permeability.Pdf*, 1998 n.d.
- [62] H. Yasuda, K. Kobayashi, A. Daimaru, M. Hori, Measurement of oxygen gas transport resistance in cathode catalyst layers of PEFC, *ECS Meet. Abstr.* (2014), <https://doi.org/10.1149/ma2014-01/18/811>. MA2014-01, 811–811.
- [63] M. Thommes, K. Kaneko, A.V. Neimark, J.P. Olivier, F. Rodriguez-Reinoso, J. Rouquerol, K.S.W. Sing, Physisorption of gases, with special reference to the evaluation of surface area and pore size distribution (IUPAC Technical Report), *Pure Appl. Chem.* 87 (2015) 1051–1069, <https://doi.org/10.1515/pac-2014-1117>.
- [64] J.H. Chun, D.H. Jo, S.G. Kim, S.H. Park, C.H. Lee, S.H. Kim, Improvement of the mechanical durability of micro porous layer in a proton exchange membrane fuel cell by elimination of surface cracks, *Renew. Energy* 48 (2012) 35–41, <https://doi.org/10.1016/j.renene.2012.04.011>.
- [65] G. Thiele, M. Poston, R. Brown, A case study sizing Nanoparticles, in: *234th ACS Natl. Meet.*, 2007, p. 316.
- [66] K.H. An, J.G. Heo, K.G. Jeon, D.J. Bae, C. Jo, C.W. Yang, C.Y. Park, Y.H. Lee, Y. S. Lee, Y.S. Chung, X-ray photoemission spectroscopy study of fluorinated single-walled carbon nanotubes, *Appl. Phys. Lett.* 80 (2002) 4235–4237, <https://doi.org/10.1063/1.1482801>.
- [67] N. Nonoyama, S. Okazaki, A.Z. Weber, Y. Ikogi, T. Yoshida, Analysis of oxygen-transport diffusion resistance in proton-exchange-membrane fuel cells, *J. Electrochem. Soc.* 158 (2011) B416, <https://doi.org/10.1149/1.3546038>.

# Superhydrophobic Fluorinated Carbons for the Microporous Layer of Polymer Electrolyte Fuel Cells

A dissertation submitted to the Kyushu University in partial fulfillment  
of the requirements for the degree of Doctor of Engineering

By

**Enes Muhammet Can**



Department of Automotive Science  
Graduate School of Integrated Frontier Science  
Kyushu University

Approved by:

Professor Stephen Matthew Lyth (examiner/supervisor)  
*Department of Automotive Science, Kyushu University*

Professor Keiji Tanaka (co-examiner)  
*Department of Automotive Science, Kyushu University*

Professor Seong-Ho Yoon (co-examiner)  
*Department of Automotive Science, Kyushu University*

Fukuoka, Japan  
2023

## **i. Abstract**

Polymer electrolyte fuel cells (PEFCs) are a highly efficient hydrogen based clean energy conversion technology. PEFCs show impressive potential to take down the long ruling internal combustion engine hegemony in the transportation sector. However, the problem of water management at high current density PEFC operations decreases the system efficiency drastically. It is thus important to create and design new materials for the gas diffusion layer (GDL) and/or the microporous layer (MPL) to improve water management as well as PEFC performance. Fluorinated carbons can be a promising alternative as MPL material due to their superior water repellent properties. Therefore, the main objective of this thesis is to increase the PEFC system performance under high current density operations by employing superhydrophobic fluorinated carbons with suitable properties as MPL material.

In Chapter 1, types of fuel cells are briefly explained with the general historical information of fuel cell technology. The general information about PEFCs is provided and its limitations are discussed with the focus on its wide-spread commercialization. The importance and the issue of water management in PEFCs are highlighted. Fluorinated carbon black is proposed as an alternative material for the MPL to improve water drainage speed under high current PEFC operations as well as the system performance. Examples of the usage of the fluorinated carbons in PEFC are given and the lack of investigating fluorinated carbon as MPL material is illustrated.

In Chapter 2, the various experimental methods used in this research are explained in detail.

In Chapter 3, superhydrophobic fluorinated carbons are synthesized and characterized intensively. A new unique synthesis of synthesized fluorinated carbons with a unique solvothermal thermal method with fluorotelomer alcohol precursors and sodium metal is presented. The effect of different fluorotelomer alcohols on chemical structure and microstructure is elucidated. Results show that a higher fluorine content of the fluorotelomer alcohol precursor results in a higher fluorine content in the final product. Interestingly, all four samples show similar microstructures with non-porous graphitized carbon black. The WCA measurement of materials shows the superhydrophobic nature of the products. Surprisingly, synthesized fluorinated carbons show highly graphitic structures even though there is not a catalyst nor high reaction temperature involved during the synthesis process. Thus, a new HF related catalytic reaction for this graphitic formation is proposed. Additionally, fluorinated carbons are defluorinated with a heat treatment process under an inert atmosphere. Then the effect of fluorination on the graphitic structure and WCA angle is investigated. It is concluded that with fluorination the defect in the graphitic domain increases due to the  $sp^3$  bonding of fluorine atoms. After defluorination, due to the absence of fluorine atoms, products become more hydrophilic.

In Chapter 4, the effect of superhydrophobic fluorinated carbon black as MPL material is investigated and its performance is compared with commercially used graphitized carbon black. The slurry of MPLs were prepared with a low amount of PTFE binder (5 wt.%) and the slurry was coated onto a GDL with a doctor blade method, followed by a heat treatment process to decompose additives as well as sintering the PTFE. To calculate porosity free standing, MPLs were manufactured by coating the slurry onto a glass plate. Carbon black

based MPL (CB-MPL) showed a higher porosity with 83% compared to fluorinated carbon based MPL (FC-MPL) with 78% porosity. Water contact angle (WCA) measurement results elucidated the superior water repellent characteristic of FC-MPL with 151° WCA compared to CB-MPL with 131° WCA. Prepared MPLs performance were compared with an in situ PEFC single test. Results clearly showed higher PEFC performance as well as lower oxygen transport resistance in the structure due to the superior water repellent properties of FC-MPL.

In Chapter 5, the findings of the previous chapters are summarized, and future direction of this research is explained.

## **ii. Acknowledgments**

The writing of a PhD thesis is an exciting yet significant and at times a lone endeavor that simply cannot be achieved on a straight road. Before we head into my research and results, into which I have poured my heart and time over the past three years, I would like to thank those who helped to straighten out the road to my dissertation. I am humbled to have met such wonderful people to share my passion for fuel cell technology with, reminding me over and over again of why I fell in love with it in the first place.

Firstly, I would like to thank my supervisor, Professor Stephen M. Lyth, who has been as excited about my research theme as I've been. I genuinely enjoyed the countless intriguing and fruitful discussions that often led me to reflect on new angles of my research. Thank you for believing in me and for encouraging me during times when things didn't go as smoothly. I'd also like to express my gratitude to Professor Kazunari Sasaki and Professor Masamichi Nishihara, who haven't hesitated to provide valuable insights and support despite their ever-busy schedules.

My time at Kyushu University wouldn't be as valuable without the presence of my likewise passionate colleagues at The Lyth Lab. I will reflect on my time in Kyushu as a period that has brought along many friendships, which I hope will last a lifetime. Special thanks must also be given to the wonderful supporting staff at Kyushu University. I appreciate you, Uchida-san Uryu-san, Itagaki-san, Zaitzu-san, and many others for helping me out with countless puzzling administrative tasks.

I would also like to thank the Republic of Türkiye. Without the financial support I've received as a Government Scholar, I wouldn't have been able to study in Japan, let alone come to this exciting chapter of closing my PhD research at Kyushu University.

And finally, but certainly not least, I'd like to thank my family, who has continuously encouraged me from tens and thousands of kilometers away, as well as my wife, Esma Esra, who has stood by me through all my travails and supported me with humour, patience, and love.

### iii. Peer Reviewed Publications

1. **E.M. Can**, A. Mufundirwa, P. Wang, S. Iwasaki, T. Kitahara, H. Nakajima, M. Nishihara, K. Sasaki, S.M. Lyth, *Superhydrophobic fluorinated carbon powders for improved water management in hydrogen fuel cells*, J. Power Sources. 548 (2022) 232098. <https://doi.org/10.1016/j.jpowsour.2022.232098>
2. **E.M. Can**, M. Nishihara, J. Matsuda, K. Sasaki, *Tailored Wettability in Fluorinated Carbon Nanoparticles Synthesized from Fluorotelomer Alcohols*, J. Appl. Surf. Sci. (2023). (Under review)

### iv. Conference Proceedings

1. **Enes M.CAN**, Kazunari Sasaki, Stephen M. Lyth, *Superhydrophobic Fluorinated Carbons for Improved Microporous Layers In Polymer Electrolyte Fuel Cells*, Vol.1 , No. 1464, pp 769~771, 23rd World Hydrogen Energy Conference, 2022
2. **Enes Muhammet Can**, 田部 豊, 近久 武美, 境田 悟志、*Study on wettability effect in water transport in gas diffusion layer of PEFC by scale model experiment and LBM simulation*, マイクロ・ナノ工学シンポジウム 2018  
<https://doi.org/10.1299/jsmemnm.2018.9.31am3PN85>

## **v. Awards**

1. Awarded Turkish Government Special Scholarship for master and doctoral course education in abroad, Ministry of National Education Turkiye, 2014
2. Encouragement award, Support Program for Doctoral Students and Overseas Students, awarded by Kyushu University Platform of Inter-/Transdisciplinary Energy Research (Q-PIT), 2021.
3. Encouragement award, Support Program for Doctoral Students and Overseas Students, awarded by Kyushu University Platform of Inter-/Transdisciplinary Energy Research (Q-PIT), 2022.

## **vi. Presentations**

1. June – 2022, The 23rd World Hydrogen Energy Conference, Superhydrophobic fluorinated carbon for improved microporous layer in Polymer Electrolyte fuel cells, Istanbul Turkiye, Poster Presenter.
2. January – 2022, Kyushu University Platform of Inter-/Transdisciplinary Energy Research (Q-PIT) Energy Week 2022, Superhydrophobic Microporous Layers for Improved Water Management in PEFCs Japan, Poster Presenter

3. December – 2021, The 1st UK-Japan Symposium on Advanced Materials for Hydrogen and Fuel Cells, Superhydrophobic Microporous Layer for Improved Water Management in Polymer Electrolyte Fuel Cells, University of Sheffield, United Kingdom, Oral Presenter.
4. December – 2021, The 62nd Battery Symposium in Japan, Superhydrophobic microporous layer for improved water management in polymer electrolyte fuel cells, Yokohama, Japan, Oral Presenter.
5. August – 2021, The 2021 World Fuel Cell Conference, Superhydrophobic fluorinated carbon for microporous layer in polymer electrolyte fuel cell, Waterloo, ON, Canada, Oral Presenter.
6. January – 2020, Kyushu University Platform of Inter-/Transdisciplinary Energy Research (Q-PIT) Energy Week 2020, Superhydrophobic fluorinated carbons for water management in PEFCs, Kyushu University, Japan, Poster Presenter.
7. October – 2018, The 9th Symposium on Micro-Nano Science and Technology, The Japan Society of Mechanical Engineers, Effect of Wettability Design on Water Transport in GDL of PEFCs Analyzed by Scale Model Experiment and LBM simulation, Poster Presenter.

8. October – 2018, The 56th meeting of Hokkaido Branch of The Japan Society of Mechanical Engineers, Study on wettability effect in water transport in Gas Diffusion Layer of PEFC analyzed by scale model experiment and LBM simulation, Hokkaido, Japan, Oral Presenter.

## Contents

Chapter 1. Introduction .....	1
1.1 Energy, Energy Security & Pollution .....	1
1.2 Fuel Cells .....	4
1.3 Polymer Electrolyte Fuel Cells (PEFCs) .....	7
1.4 Application and Challenges of PEFCs.....	11
1.5 Water Management in PEFCs.....	15
1.6 The role of the MPL in PEFC Water Management .....	17
1.7 Fluorinated Carbons in PEFCs .....	19
1.8 Objectives of this Study .....	20
1.9 References.....	22
Chapter 2. Experimental Methods.....	31
2.1 Synthesis of Fluorinated Carbon Powders .....	31
2.2 Material Characterization Techniques .....	32
2.2.1 Scanning Electron Microscopy (SEM).....	32
2.2.2 X-ray Photoelectron Spectroscopy (XPS) .....	33
2.2.3 Energy Dispersive X-ray Analysis (EDX) .....	36
2.2.4 X-ray Diffraction (XRD) .....	37
2.2.5 Transmission Electron Microscopy (TEM) & Selected Area Electron Diffraction (SAED) .....	38
2.2.6 Raman Spectroscopy .....	40
2.2.7 Surface Area and Pore Size Distribution Analysis .....	41
2.2.8 Thermogravimetric Analysis (TGA) .....	42
2.3 Electrochemical Characterization Techniques.....	43
2.3.1 Microporous Layer (MPL) Manufacturing and Coating .....	43
2.3.2 Water Contact Angle Measurement of MPLs .....	45
2.3.3 Air Permeability Test of MPLs .....	46
2.3.4 Membrane Electrode Assembly Preparation (MEA).....	47
2.3.5 Polymer Electrolyte Fuel Cell (PEFC) Testing .....	49
2.3.6 Oxygen Transport Resistance Test .....	52
2.4 References.....	54
Chapter 3. Synthesis and Characterization of Fluorinated Carbon Powder .....	56

3.1	Introduction.....	56
3.2	Experimental Methods .....	58
3.3	Results and Discussion .....	61
3.3.1	Scanning Electron Microscopy (SEM).....	63
3.3.2	Surface Area and Porosity .....	65
3.3.3	X-ray Photoelectron Spectroscopy (XPS) .....	67
3.3.4	Energy Dispersive X-Ray Analysis (EDX) .....	73
3.3.5	X-ray Diffraction (XRD) .....	76
3.3.6	Raman Spectroscopy .....	78
3.3.7	Transmission Electron Microscopy (TEM) and Selected Area Electron Diffraction (SAED) .....	81
3.3.8	New Catalytic Mechanism for Graphitic Structure .....	83
3.3.9	Thermogravimetric Analysis (TGA), Differential Thermal Analysis (DTA), and Differential Thermogravimetry (DTG).....	84
3.3.10	Water Contact Angle (WCA) Measurement .....	86
3.3.11	Secondary Heat Treatment and Removal of Fluorine .....	88
3.4	Summary and Conclusion .....	92
3.5	References.....	93
Chapter 4.	Application of Fluorinated Carbons in Microporous Layers .....	102
4.1	Introduction.....	102
4.2	Experimental.....	104
4.2.1	Preparation of the MPL .....	104
4.2.2	Preparation of the Membrane Electrode Assembly (MEA) .....	108
4.2.3	Thermogravimetric Analysis Tests.....	108
4.2.4	Fuel Cell Polarization Tests.....	108
4.2.5	Air Permeability Tests .....	110
4.2.6	Water Contact Angle Measurements .....	110
4.2.7	Oxygen Transport Resistance.....	112
4.3	Results and Discussions.....	113
4.3.1	Scanning Electron Microscopy (SEM) and Transmission Electron Microscopy (TEM) Imaging.....	113
4.3.2	Surface Area and Porosity .....	116
4.3.3	Density Measurement and Calculation.....	117
4.3.4	Thermogravimetric Analysis (TGA) .....	118

4.4	Microporous Layer Characterization .....	119
4.4.1	Scanning Electron Microscopy Imaging .....	119
4.4.2	Water Contact Angle Measurement and Porosity Calculation of MPLs.....	120
4.4.3	Air permeability and Oxygen Transport Resistance Tests .....	122
4.4.4	Single Cell Characterization .....	124
4.5	Summary and Conclusions .....	128
4.6	References.....	129
Chapter 5.	Summary, Conclusion and Future Outlook .....	136

## List of Figures

Figure 1.1	Share of electricity production from fossil fuels, 2021 [2]. .....	2
Figure 1.2	Schematic diagram of a PEFC. ....	9
Figure 1.3	Components of a single PEMFC [3]. ....	10
Figure 1.4	Series arrangement of typical hydrogen PEMFC [4]. ....	11
Figure 1.5	Photo of fuel cell vehicle Toyota Mirai. ....	13
Figure 1.6	Photo of PEFC-powered unmanned aerial vehicle [15]. ....	13
Figure 1.7	(a) Schematic diagram of PEFC, (b) Illustration of cathode GDL under the normal PEFC operation, (c) Illustration of cathode GDL under the high current density PEFC operation. ....	17
Figure 2.1	Photos of (a) PTFE crucible, (b) stainless-steel jacket. ....	32
Figure 2.2	Principle of X-ray photoelectron spectroscopy (XPS) [3]. ....	34
Figure 2.3	Photo of XPS analysis equipment. ....	35
Figure 2.4	Principle of XRD according to Bragg's law [7]. ....	37
Figure 2.5	Rigaku Smartlab X-Ray Diffractometer. ....	38

Figure 2.6 A simplified diagram of a TEM [8]. .....	39
Figure 2.7 Renishaw inVia Raman Microscope.....	40
Figure 2.8 Photo of the nitrogen gas adsorption/desorption equipment (Belsorp-mini, BEL Japan).....	42
Figure 2.9 Thermogravimetric analysis Equipment. ....	43
Figure 2.10 Photo of the stainless-steel frame used for MPL coating using the doctor blade technique.....	44
Figure 2.11 Photo of a MPL coated GDL. ....	45
Figure 2.12 Photo of WCA measurement equipment. ....	46
Figure 2.13 Schematic diagram of air permeability test equipment [11]. ....	47
Figure 2.14 (a) Nordson K.K. Spraying Device, (b) Sinto Digital Press CYPT-10.....	48
Figure 2.15 Photo of catalyst coated membrane. ....	49
Figure 2.16 Photos of a single cell for PEFC performance test, (a-b) assembled single cell, (c) graphite flow channel, gold coated current collector, and end plate, (d) gold coated current collector and end plate, (e) gasket with 150 $\mu\text{m}$ thickness.....	50
Figure 2.17 PEFC test station (AUTOPEM-CVZ01, Toyo Corporation, Japan).....	52
Figure 3.1 (a) Photograph of sample (a) CFx-C10, (b) CFx-C8 (c) CFx-C6, and (d) CFx-C5 immediately after opening the PTFE reactor.....	62
Figure 3.2 Plot of the temperature inside the PTFE crucible during the reaction. ....	63
Figure 3.3 SEM images of the four fluorinated carbons synthesized in this work: (a) CX-CF10; (b) CX-CF8; (c) CX-CF6; and (d) CX-CF5. ....	64
Figure 3.4 SEM images of different structure in synthesized fluorinated alcohols. ....	65

Figure 3.5 Nitrogen gas adsorption results for the fluorinated carbons synthesized in this work: (a) BET isotherms, (b) BJH analysis, and (c) MP plots.....	67
Figure 3.6 Fluorine content as measured by XPS and EDX. ....	68
Figure 3.7 XPS of CFX-C10: (a) survey spectrum; (b) C 1s region, (c) F 1s region; (d) O1s region; and the (e) Na 1s region. ....	70
Figure 3.8 XPS of CFX-C8: (a) survey spectrum; (b) C 1s region, (c) F 1s region; (d) O1s region; and the (e) Na 1s region. ....	71
Figure 3.9 XPS of CFX-C6: (a) survey spectrum; (b) C 1s region, (c) F 1s region; (d) O1s region; and the (e) Na 1s region. ....	72
Figure 3.10 XPS of CFX-C5: (a) survey spectrum; (b) C 1s region, (c) F 1s region; (d) O1s region; and the (e) Na 1s region. ....	73
Figure 3.11 EDX mapping of sample CFX-C6. ....	76
Figure 3.12 XRD for the four fluorinated carbon samples: (a) CX-CF10; (b) CX-CF8; (c) CX-CF6; and (d) CX-CF5. ....	78
Figure 3.13 Raman spectroscopy of the fluorinated carbon samples: (a) CX-CF10; (b) CX-CF8; (c) CX-CF6; and (d) CX-CF5.....	80
Figure 3.14 TEM images of the fluorinated carbon samples: (a) CX-CF10; (b) CX-CF8; (c) CX-CF6; and (d) CX-CF5. ....	81
Figure 3.15 TEM and SAED analysis results of the samples (a) CX-CF10, (b) CX-CF8, (c) CX-CF6, (d) CX-CF5. ....	82
Figure 3.16 Thermogravimetric analysis (TGA) and differential thermal analysis (DTA) of the synthesized fluorinated carbons: (a) CX-CF10; (b) CX-CF8; (c) CX-CF6; (d) CX-CF5. ....	85

Figure 3.17 Thermogravimetric analysis and difference thermogravimetric analysis of samples (a) CFX-C10, (b) CFX-C8, (c) CFX-C6, (d) CFX-C5.....	86
Figure 3.18 Water contact angle (WCA) measurements for: (a) CX-CF10; (b) CX-CF8; (c) CX-CF6; (d) CX-CF5.....	87
Figure 3.19 XPS of CFX-C8-HT: (a) survey spectrum; (b) C 1s region; (c) F 1s region; (d) O1s region; and (e) Na 1s region.....	89
Figure 3.20 (a-b) XRD and (c-d) Raman spectra of CFX-C8 and CFX-C8-HT.....	91
Figure 4.1 TGA of Methyl Cellulose and Triton-X.....	105
Figure 4.2 Photo of a MPL coated GDL. ....	106
Figure 4.3 Photo of a free-standing MPL. ....	107
Figure 4.4 Electron microscopy showing the microstructure of the fluorinated carbons used in this study: (a-b) SEM images, (c-d) TEM images.....	114
Figure 4.5 SEM image of fluorinated carbon with large particles .....	115
Figure 4.6 (a-b) SEM images of carbon black. ....	115
Figure 4.7 (a) Brunauer-Emmett-Teller (BET) nitrogen adsorption isotherms, and (b) Barrett-Joyner-Halenda (BJH) pore size distribution graphs.....	117
Figure 4.8 TGA of fluorinated carbon and graphitized carbon black in air. ....	119
Figure 4.9 SEM images of MPL surface at different magnifications: (a-b) FC-MPL; (c-d) CB-MPL. ....	120
Figure 4.10 Surface water contact angle (WCA) measurements for: (a) pressed fluorinated carbon (FC); (b) FC-MPL; (c) CB-MPL; and (d) Toray-GDL (TGP-H-060).....	121

Figure 4.11 (a) Maximum pore diameter; (b) internal water contact angle; (c) air permeability; and (d) oxygen transport resistance for Toray-GDL, CB-MPL and FC-MPL.

..... 124

Figure 4.12 Single cell PEFC measurements under different relative humidity conditions. Polarization curves (IR-free) at cell temperatures of (a) 45 °C and (b) 80 °C. Concentration overvoltage at (c) 45 °C (d) 80 °C. IR overpotential at (e) 45 °C and (f) 80 °C. .... 127

## List of Tables

Table 1.1 Share of Russian gas in total natural gas demand and share of gas in sectoral demand by European Union member states and the United Kingdom, 2021 [1]. .... 3

Table 1.2 Comparison of various types of fuel cell. .... 7

Table 2.1 XPS analysis measurement conditions. .... 36

Table 3.1 Summary of the fluorotelomer alcohol precursors. .... 60

Table 3.2 Elemental composition of synthesized fluorinated carbons measured by XPS. .. 68

Table 3.3 Elemental composition of synthesized fluorinated carbons as measured by EDX.

..... 74

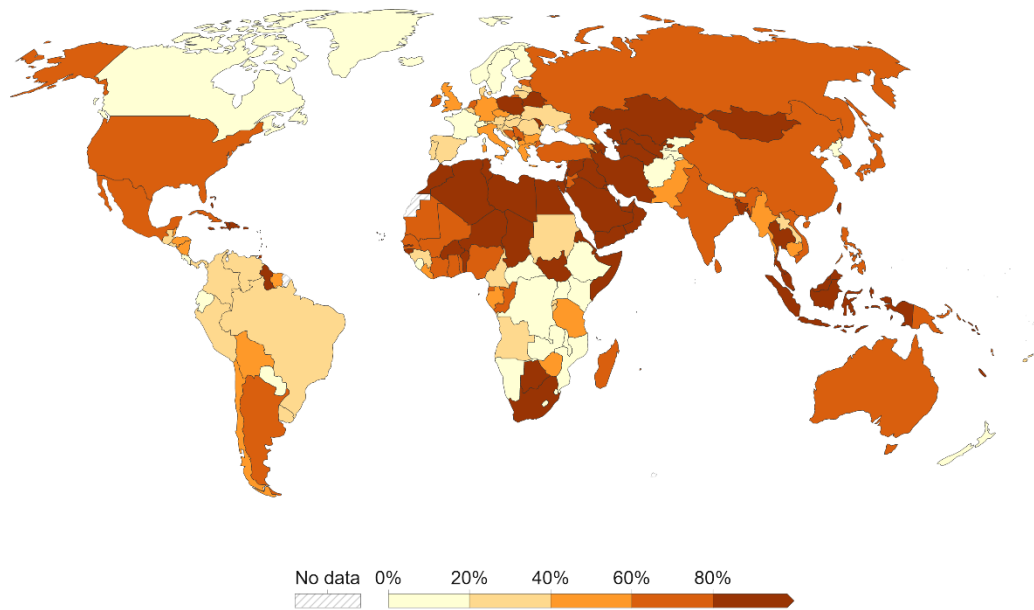
# **Chapter 1. Introduction**

## **1.1 Energy, Energy Security & Pollution**

One of the simplest physical definitions of ‘energy’ is ‘the ability to do work’. However, access to energy in today’s society is a necessary parameter in society to access high technology, quality of life, wealth. Energy is also one of the most important issues in politics, and important in the independency of nations.

According to data provided by International Energy Agency (IEA), over 80% of the world’s energy supply comes from fossil fuels and 63% of global electricity production comes from fossil fuels [1,2]. Figure 1.1 shows the share of electricity production from fossil fuels. Furthermore, over half of fossil fuel production originates from Russia, China, USA, and the Middle East. Most countries, especially those with high energy demand such as those in Europe, Japan, and rapidly developing such as Türkiye, are dependent on external countries with rich fossil fuel reserves. Especially after the breakout of the 2022 Russia-Ukraine war, Western society has come to quickly understand that energy dependency is no longer feasible (Table 1). Energy is also particularly important in winter, where countries such as the United Kingdom are currently dealing with a cost-of-living crisis due to sudden high energy costs for heating homes. Independent self-sufficient energy production can therefore be considered crucial.

## Share of electricity production from fossil fuels, 2021



Source: Our World in Data based on BP Statistical Review of World Energy (2022); Our World in Data based on Ember's Yearly Electricity Data (2022); Our World in Data based on Ember's European Electricity Review (2022)  
OurWorldInData.org/energy • CC BY

**Figure 1.1 Share of electricity production from fossil fuels, 2021 [2].**

**Table 1.1 Share of Russian gas in total natural gas demand and share of gas in sectoral demand by European Union member states and the United Kingdom, 2021 [1].**

Market size	Country	Russian share	Share of gas in sectoral demand		
			Power	Industry	Buildings
>20 bcm	Germany*	46%	20%	31%	38%
	United Kingdom	3%	43%	32%	55%
	Italy*	41%	51%	31%	50%
	France*	20%	9%	31%	29%
	Netherlands**	36%	58%	30%	59%
	Spain	11%	31%	38%	22%
10-20 bcm	Poland**	46%	9%	28%	19%
	Belgium	7%	30%	28%	41%
	Romania	6%	28%	37%	34%
5-10 bcm	Hungary	78%	37%	30%	50%
	Austria*	74%	21%	34%	20%
	Czech Republic*	67%	13%	24%	30%
	Portugal	10%	40%	23%	12%
<5 bcm	Slovak Republic*	76%	20%	28%	40%
	Ireland	0%	52%	42%	22%
	Denmark**	60%	11%	30%	13%
	Greece	39%	29%	23%	9%
	Bulgaria**	100%	15%	34%	5%
	Croatia	0%	32%	51%	22%
	Finland**	68%	8%	6%	1%
	Lithuania**	50%	17%	59%	11%
	Latvia*	100%	48%	11%	13%
	Sweden	14%	1%	5%	1%
	Slovenia	12%	7%	34%	9%
	Luxembourg	25%	27%	44%	36%
	Estonia**	46%	9%	21%	9%

\* Denotes a partial cut. \*\* Denotes a full cut.

Fossil fuel usage impacts global warming severely, and ultimately contributes to climate change through the emission of carbon dioxide and other greenhouse gases. Not only climate change is a pressing issue, but also harmful gas emissions such as carbon monoxide

(CO), nitrogen oxides (NO<sub>x</sub>), and particulate matter (PM) due to fossil fuel combustion, all of which pose severe risk to human health. According to the World Health Organization, air pollution is responsible for 6.7 million premature deaths per year [1]. Air pollution also leads to noncommunicable diseases including strokes, ischaemic heart disease, and lung cancer.

It is therefore crucial to find a new alternative energy source which is clean, abundant, and can be independently produced. In this regard, hydrogen is a promising candidate. Hydrogen is the most abundant element in the world and molecular hydrogen can be produced through various means such as electrolysis of water using renewable energy, or the fermentation of biomass. Furthermore, hydrogen-based energy technologies, such as fuel cells, have high potential to be a game changer in electricity production. For example, polymer electrolyte fuel cells (PEFC), which operate at relatively low temperatures (i.e., 60 to 80 °C), have the potential to replace internal combustion engines in vehicles, as well being used for stationary power. Compared to internal combustion engines, PEFCs have a higher efficiency (~50%). Due to their great potential in combating the abovementioned issues, a worldwide spread of PEFCs as prominent energy technology is crucial.

## **1.2 Fuel Cells**

Fuel cell are electrochemical devices that generate electricity from two electrochemical half reactions between fuel at the anode and oxidant at the cathode electrode side. An electrolyte separates these two electrodes. Fuel cells are classified depending on the electrolyte type which it employs. There are five major fuel cell types: (1) phosphoric acid fuel cells (PAFCs), (2) polymer electrolyte fuel cells (PEFCs), (3) alkaline fuel cells (AFCs), (4) molten

carbonate fuel cells (MCFCs), and (5) solid-oxide fuel cells (SOFCs). Even though these different types of fuel cells have different electrolytes, different materials and operation temperatures, the underlying electrochemical principle is similar. Their basic characteristics are compared in Table 2.

The phosphoric acid fuel cell (PAFC) was the first commercial type of fuel cell. Due to the relatively high operating temperature compared to PEFCs (200°C), the platinum catalyst is less sensitive to carbon monoxide in the fuel. Noble catalysts are required at the cathode side, and therefore the potential for cost reduction is considered to be low. PAFCs are mostly used for stationary electricity and heat production.

Alkaline fuel cells (AFC) generally use a potassium hydroxide aqueous solution as an electrolyte medium. The kinetics of the oxygen reduction reaction proceed more rapidly in alkaline medium than in acidic medium and therefore platinum group metals are not required as cathode catalysts. Therefore, alkaline fuel cells can achieve operating voltages as high as 0.875 V, translating to high efficiency. However, alkaline fuel cells must use pure hydrogen and oxygen as fuel, due to the high sensitivity of the electrolyte to even small amounts of carbon dioxide in the air. Due to this limitation, AFCs are not generally viable for terrestrial power applications. However, the high efficiency and power density leads to applications in the aerospace industry.

Meanwhile, solid oxide fuel cells (SOFCs), and molten carbonate fuel cells (MCFCs) are classified as high temperature fuel cells. SOFCs utilize a ceramic oxygen ion conductive electrolyte and operate in the region of 700 to 1000°C. The high operating temperature means

that there is no need for noble metal catalysts, there is significant fuel flexibility, and high-quality waste heat is produced for co-generation applications. Nevertheless, the high temperature also provides challenges: particularly in terms of material durability and cost. SOFCs are best suited for stationary and distributed power generation. Molten carbonate fuel cells (MCFCs) are being developed for natural gas and coal-based power plants for industrial, electrical utility and military applications. MCFCs are similar to SOFCs but use a molten electrolyte, with similar advantages and disadvantages.

Finally, the polymer electrolyte fuel cell (PEFC) is based around a proton-conducting polymer electrolyte membrane, usually Nafion. Its low operation temperature (i.e. 60 to 80 °C), fast start up and shutdown, and high-power density, make it a good candidate for portable applications, and especially for vehicles. In this thesis, polymer electrolyte fuel cell will be the focus.

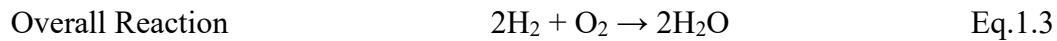
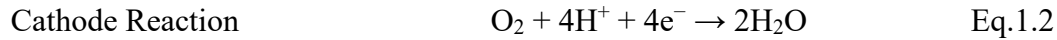
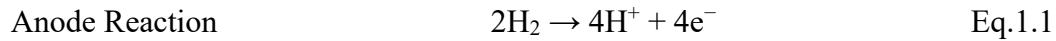
**Table 1.2 Comparison of various types of fuel cell.**

	PEFC	PAFC	AFC	MCFC	SOFC
Electrolyte	Polymer	Liquid $\text{H}_3\text{PO}_4$	Liquid KOH	Molten carbonate	Ceramic
Charge carrier ion	$\text{H}^+$	$\text{H}^+$	$\text{OH}^-$	$\text{CO}_3^{-2}$	$\text{O}^{-2}$
Operating Temperature ( $^{\circ}\text{C}$ )	60 to 80	200	60 to 220	650	600-1000
Reaction Catalyst	Platinum	Platinum	Platinum	Nickel	Perovskites
Fuel	$\text{H}_2$ , Methanol	$\text{H}_2$	$\text{H}_2$	$\text{H}_2$ , $\text{CH}_4$	$\text{H}_2$ , $\text{CH}_4$ , CO

### **1.3 Polymer Electrolyte Fuel Cells (PEFCs)**

In PEFC systems, a polymer electrolyte membrane is employed. This membrane blocks the movement of electrons and allows protons pass through. PEFCs are preferred mainly for transportation applications due to their low operational temperature and high-power density. In PEFCs, two electrochemical half-cell reactions occur, namely the anode and cathode reactions. At the anode side, the hydrogen oxidation reaction (HOR) occurs, and at the cathode side the oxygen reduction reaction (ORR) occurs. The difference in Gibbs free energy between the two reactions generates a potential difference, which manifests as a voltage. As a result of the HOR, hydrogen is separated into its constituent electrons and protons (Eq.1). The potential difference pushes electrons around an external circuit while

protons are diffuse through the polymer electrolyte to the cathode side. At the cathode side, electrons and protons react with supplied oxygen and produce H<sub>2</sub>O (Eq.2). The overall reaction is shown in Eq. 3. As long as there is enough fuel and oxidant present, PEFC systems can continue to generate a voltage indefinitely. A schematic diagram of the working principle of a PEFC is shown in Figure 1.1 and the electrochemical half-cell reaction in a hydrogen fueled PEMFC are as follows. The catalyst coated membrane (CCM) is at the heart of the PEFC system. This comprises the membrane coated with catalyst layers on either side. The catalyst layer in turn generally comprises platinum catalyst nanoparticles supported on carbon black.



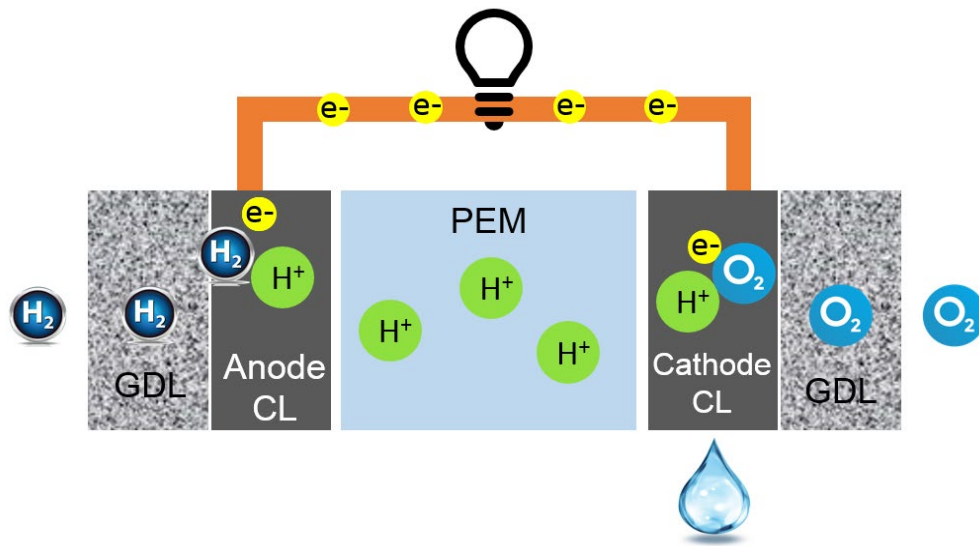


**Figure 1.2 Schematic diagram of a PEFC.**

Meanwhile, an important engineering aspect of PEFCs is the supply of reactants to the electrodes, and the removal of the generated water. Therefore, a polymer electrolyte cell contains a gas diffusion layer (GDL) at each electrode, sandwiching the catalyst coated membrane. The GDL is used in the system to transfer to reactant to the catalyst layer and to act as mechanical support for the CCM. The combined GDL and CCM are collectively called the membrane electrode assembly (MEA). The other components of a single PEFC, including the MEA are shown schematically in Figure 1.3.

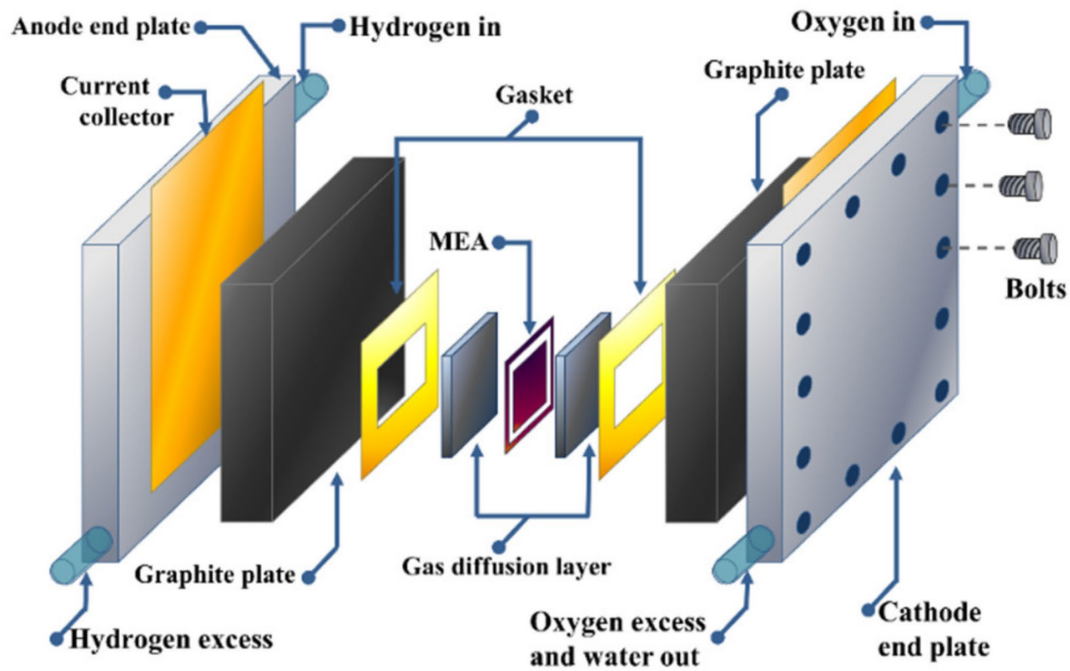


**Figure 1.3 Components of a single PEMFC [3].**

The current produced by a fuel cell scales with the size of the reaction area. The reaction area is the active area where electrolyte and electrodes meet. To increase the generated current, it is therefore necessary to maximize the reaction area, and achieving this is one of the most active areas of research in the field of PEMFCs. The thin, planar structural design of individual PEMFCs is a consequence of this (Figure 1.4).

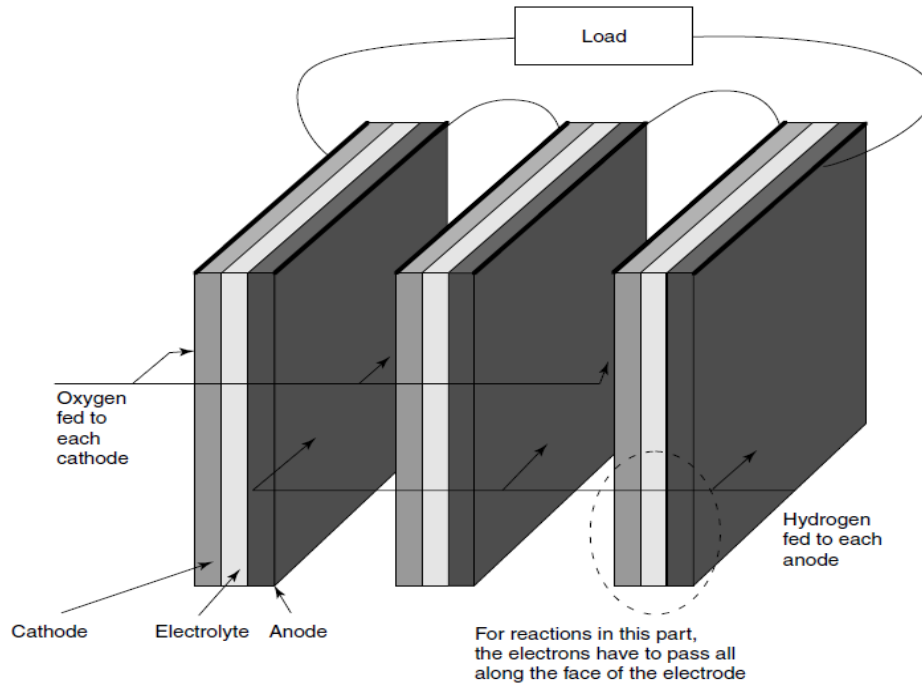


**Figure 1.4 Series arrangement of typical hydrogen PEMFC [4].**

## 1.4 Application and Challenges of PEFCs

The first working fuel cell was demonstrated by Sir William Grove in 1839 [5,6]. Later, in 1959, Francis Thomas Bacon built a 6 kW AFC seen as the first practically feasible fuel cell, and went on to design AFCs used to provide electrical power on crewed Apollo missions [7]. Bacon's work inspired many researchers as he is considered a pioneer in the development of other types of fuel cell systems. The first practical PEFC was invented by General Electric in the 1960s, a company known to provide various products and services in the energy sector [8]. This early version of the PEFC was used in the NASA Gemini spacecraft. However, due

to a severe water management problems in these early PEFC systems, NASA continued mainly using AFCs for several decades [8].

In 1995, a PEFC system for buses in was developed by Ballard Systems, operating in Vancouver and Chicago [9]. Since the beginning of this century, a significant number of automobile companies have introduced fuel cell electric vehicles (FCEVs) to the public. A prime leader in introducing these vehicles is Japan. In 2014, Toyota released the first commercially available FCEV named Toyota Mirai in Japan (Figure 1.4) [10]. South Korea followed up with the introduction of Nexo in 2018, a PEFC powered crossover SUV manufactured by Hyundai [11].

There have also been multiple attempts to introduce PEFCs for stationary applications such as residential or industrial use, such as combined heat and power systems which have been available on the market in Japan under the trade name ENE-FARM since 2008 [12]. In 2009, the world's first purely hydrogen-powered crewed aircraft was developed by the German Aerospace Center [13]. Moreover, H3 Dynamics, a USA based company, commercially produces unmanned aerial vehicles powered by PEFC systems (Figure 1.5) [14].



**Figure 1.5 Photo of fuel cell vehicle Toyota Mirai.**



**Figure 1.6 Photo of PEFC-powered unmanned aerial vehicle [15].**

Despite the remarkable development of PEFCs over the past decade, their market penetration has been relatively slow compared to internal combustion engines and lithium-ion batteries. This is largely due to high cost of the system, which should be significantly reduced to accelerate global scale up. Cost reduction in PEFC systems can generally be achieved in three ways: (1) reducing the cost of the components; (2) improving system durability; or (3) increasing system efficiency. One of the major component costs of PEFC is the platinum catalyst. In early PEFC systems, a platinum loading of 28 mg/cm<sup>2</sup> was required for the catalyst layer. Due to continuous efforts to improve the system, this has decreased significantly to 0.2 mg/cm<sup>2</sup> or even less in current applications [4].

Another important factor to consider is the lifetime of PEFCs, which is limited due to several factors [16]. One factor is the dissolution and agglomeration of platinum particles, which decrease the active reaction area dramatically. Another factor is that carbon-support corrosion decreases conductivity and affects electrode pore structure [17]. One more main factor is thinning and possible pinhole formation in the polymer electrolyte membrane because of hydrogen peroxide formation during operation, also increasing hydrogen crossover [18]. For example, the early PEFC system used in the Gemini spacecraft had only a 500-hour lifetime [19]. This number increased to around 4100 hours in 2016 [20] and today's systems have rated lifetimes in the tens of thousands of hours.

In addition, to increase the system efficiency of PEFCs, it is important to generate higher currents for a given electrode area. To generate higher currents, the fuels should be supplied at a higher rate. However, increasing the reaction rate results in the generation of a larger amount of water. The presence of large amounts of water in the cathode drastically

decreases the fuel cell efficiency by blocking the flow of reactants and covering the electrode area. Water management is therefore crucial to increase PEFC performance.

## **1.5 Water Management in PEFCs**

Under high current density operation water accumulates inside the gas diffusion layer (GDL) blocking the flow of reactants and covering the catalytic active sites. A major factor for NASA using AFCs over PEFCs in the Apollo space missions was the issue of water management [19]. Even today, water management in PEFCs is a crucial factor limiting the widespread introduction of PEFC technologies.

The incorporation of a GDL into PEFCs aids greatly with water management. The GDL is a thin layer of carbon fibres and generally has a thickness of 100 to 400  $\mu\text{m}$ . To improve the mass transport properties, GDLs are created with a high porosity of around 85%, and with pores around 20-30  $\mu\text{m}$  in diameter. It is placed between the catalyst layer and the flow channels, and aids the transfer of gasses to the catalyst layer whilst mechanically supporting the catalyst layer. At the anode side, hydrogen diffuses from the flow channel to the catalyst layer through the GDL. There is no product to be transferred back to the flow channel from the catalyst layer as a result of hydrogen oxidation reaction (HOR).

On the other hand, at the cathode side, the GDL is used to transfer oxygen to the catalyst layer for the oxygen reduction reaction (ORR). It is also simultaneously used to transfer water, a product of the ORR, from the cathode catalyst layer to the flow channel (Figure 1.6 (a)). However, when high current is demanded from the system, the reaction rate of the ORR increases and water is produced excessively at the cathode (Figure 1.6 (b-c)). This produced

water blocks the pores of the GDL and thus hinders oxygen transfer from the flow channel to the catalyst layer. This phenomenon is called '*flooding*' and decreases PEFC efficiency drastically [21]. It is therefore important to remove the generated water from the PEFC system more efficiently without blocking oxygen transfer that is needed to supply the ORR.

One way to assist with the removal of water from the GDL is to use a hydrophobic material. Therefore, to improve the water repellent properties, GDLs are generally coated with polytetrafluoroethylene (PTFE) to render them hydrophobic [22]. Furthermore, to decrease the contact resistance as well as to regulate transfer of the gases and produced water, a microporous layer (MPL) is generally coated onto one side of the GDL [23]. The MPL generally consists of carbon black and a hydrophobic binder such as PTFE and it faces the catalyst layer in the system. Like the GDL, the MPL is also highly porous with around 80% porosity. The pore size of the MPL, however, is smaller, measuring around 1 to 2  $\mu\text{m}$  in diameter compared to the GDL's pore size around 20- to 30  $\mu\text{m}$  in diameter.

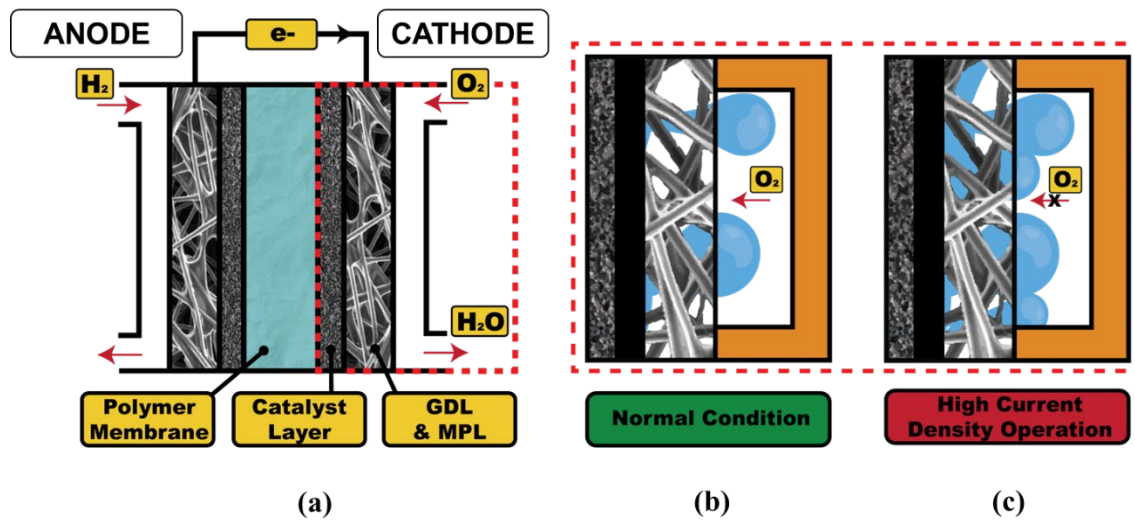


**Figure 1.7 (a) Schematic diagram of PEFC, (b) Illustration of cathode GDL under the normal PEFC operation, (c) Illustration of cathode GDL under the high current density PEFC operation.**

## 1.6 The role of the MPL in PEFC Water Management

As one of the important components of PEFCs, the MPL improves the fuel cell performance drastically [23]. Due to the smaller pore size in the MPL compared to the GDL, the MPL acts as a buffer layer between the catalyst layer and the GDL. This improves the electrical contact between the catalyst layer and thus decreases the efficiency losses [24]. Furthermore, the MPL enhances the removal of excess water, but also aids hydration of the membrane under dry operating conditions.

The most common material used as the MPL is carbon black. The material properties of carbon-based MPLs, including the pore size, thermal conductivity, electrical conductivity, and water contact angle significantly affect the system performance and durability. Tanuma et al. investigated four different carbon materials in the MPL, namely carbon fiber, vapor

grown carbon fiber, Vulcan XC-72R carbon black, and multiwall carbon nanotubes, to investigate the effect of MPL pore size on the performance of PEFCs. It was found that the pore volume of the MPL has significant effect on the cell performance where large pores of the MPL reduce the water saturation in the catalyst layer [25].

Meanwhile, Wang et al. investigated MPLs using two different types of carbon black, which are acetylene black, Black Pearl 2000. They found that, depending on the hydrophobicity of the carbon material, some pores in the MPL remain hydrophilic even if a hydrophobic binder is used. Ultimately, the more hydrophilic in nature the carbon used in an MPL, the more pores will remain hydrophilic, even if hydrophobic binder is applied. This illustrates clearly the disadvantage of using hydrophilic carbons in MPLs [26]. Similar to the above mentioned research, there have been extensive studies to elucidate the effect of different carbon materials in the MPL on PEFC performance [27–34]

Furthermore, the effect of the type of hydrophobic binders used in the MPL on PEFC performance has been investigated [35–37]. For example, Ozturk et. al used three different hydrophobic binders, namely PTFE, fluorinated ethylene propylene (FEP), and polydimethylsiloxane (PDMS), to create MPLs and compared their performance [37]. They found that PDMS performed better compared to the other binders due to its low molecular weight and viscosity. Furthermore, there has been several studies on the effect of hydrophobic binders on MPL morphology and its effect on PEFC performance [29,38,39]. Yan et al. indicated that it is possible to achieve higher hydrophobicity by increasing the amount of hydrophobic binder. They noted, however, that excessive binder amounts lead to (i) a decrease in MPL pore size with an associated increase in gas diffusion resistance and

(ii) an increase in electrical resistance [32,40], both of which have a negative impact on PEFC performance. Additionally, Owejan et. al. showed that MPLs are prone to carbon corrosion under high humidity conditions due to oxidation, making MPLs more hydrophilic over time and leads to a degradation in system performance [31].

It is therefore crucial to create MPLs from different kinds of carbon material that establish superior hydrophobicity even at lower binding loadings. This kind of material could increase the water transport rate through the GDL under high current density operation without needing a higher amount of hydrophobic binder. With this process the detrimental decrease in pore diameter can be avoided, as well as the increase in gas transport and electrical resistance of the MPL.

## **1.7 Fluorinated Carbons in PEFCs**

The incorporation of fluorine atoms can significantly alter the physical, chemical, and electronic properties of carbon-based materials. In particular, fluorination generally leads to enhanced hydrophobicity due to low surface free energy and reduced van der Waals interactions [41–43]. In PEFC systems, fluorinated carbons have mostly been employed as a platinum support within the catalyst layer [44–48]. Otherwise, fluorinated carbons have only been explored to a limited extent in PEFC systems.

For example, Glass et al. showed that the use of fluorinated carbon black as the catalyst support improves the catalyst-ionomer dispersion and intercalation, compared to non-fluorinated carbon black. This results in an increased fuel cell performance [46]. Similarly, Peera et al. investigated nitrogen and fluorine co-doped graphite nanofibers as durable and

platinum-free ORR catalyst for PEFCs. They found that due to fluorine doping, the number of defects in the structure increases, leading to higher ORR activity. Furthermore, they concluded that fluorine doping increased the durability of the catalyst dramatically [48]. Kim et al. addressed the problem of carbon corrosion by investigating doped tin oxide materials as corrosion resistant carbon-free catalyst supports, concluding that fluorine doping provided the most effective corrosion resistance [48].

In all of the abovementioned research, fluorinated carbons were used in the catalyst layer, and the focus was mainly on improving ORR activity and mitigating carbon corrosion. Up to now, there has been no effort to elucidate the effect of using fluorinated carbon in the MPL for PEFC applications, to the best of our knowledge.

## **1.8 Objectives of this Study**

As explained above, water management under high current density operation is crucial for the widespread commercialization of PEFCs. Conventionally used carbon materials in the MPL therefore require PTFE as a hydrophobic additive. Another issue is that even with the hydrophobic PTFE binder, depending on the wettability of the carbon material, some pores of MPL remain hydrophilic [26]. This results in performance deterioration over the lifetime of the cell. Furthermore, the degree of hydrophobicity of the MPL depends strongly on the amount of PTFE binder used. For example, relatively small amounts of PTFE (e.g., 5 wt.%) do not provide sufficient hydrophobicity, whereas larger amounts of PTFE (e.g., 20 wt.%) leads smaller pore diameter (increasing the gas diffusion resistance) and higher electrical resistance due to the insulating nature of PTFE [49].

Fluorinated carbon powder is a promising material to enhance the hydrophobicity of MPLs at lower PTFE loading, and could potentially improve PEFC efficiency under high current density operation. In this thesis we therefore focus first on the synthesis, characterization, and optimization of superhydrophobic fluorinated carbons (Chapter 3). These synthesized superhydrophobic fluorinated carbons are then employed as a hydrophobic MPL material with an aim to improve water management in PEFCs even at low PTFE loading (Chapter 4).

## 1.9 References

- [1] A.J. Appleby, From Sir William Grove to today: fuel cells and the future, *J. Power Sources*. 29 (1990) 3–11. [https://doi.org/10.1016/0378-7753\(90\)80002-U](https://doi.org/10.1016/0378-7753(90)80002-U).
- [2] B.P. Statistical Review, bp Statistical Review of World Energy globally consistent data on world energy markets . The review is one of the most widely respected The Statistical of publications World Energy analyses and Review energy used from by the prior The Review academia , ha, Rep. Stat. Rev. World Energy Glob. Consistent Data World Energy Mark. (2022) 60.
- [3] M.M. Tellez-Cruz, J. Escorihuela, O. Solorza-Feria, V. Compañ, Proton exchange membrane fuel cells (Pemfcs): Advances and challenges, *Polymers (Basel)*. 13 (2021) 1–54. <https://doi.org/10.3390/polym13183064>.
- [4] R. O’Hayre, S.-W. Cha, W. Colella, F.B. Prinz, *Fuel Cell Fundamentals*, John Wiley & Sons, Inc, Hoboken, NJ, USA, 2016. <https://doi.org/10.1002/9781119191766>.
- [5] W.R. Grove, LXXII. On a gaseous voltaic battery , London, Edinburgh, Dublin *Philos. Mag. J. Sci.* 21 (1842) 417–420. <https://doi.org/10.1080/14786444208621600>.
- [6] PII\_ 0378-7753(90)80002-U \_ Elsevier Enhanced Reader.pdf, (n.d.).
- [7] E.M. COHN, NASA’s Fuel Cell Program, (1969) 1–8. <https://doi.org/10.1021/ba-1965-0047.ch001>.
- [8] Collecting the History of Proton Exchange Membrane Fuel Cells, (n.d.).

<https://americanhistory.si.edu/fuelcells/pem/pemmain.htm> (accessed December 24, 2022).

- [9] Our History - Power to Change the World | Ballard Power, (n.d.). <https://www.ballard.com/about-ballard/our-history> (accessed December 24, 2022).
- [10] Toyota rolls out latest Mirai hydrogen fuel cell vehicle - Nikkei Asia, (n.d.). <https://asia.nikkei.com/Business/Automobiles/Toyota-rolls-out-latest-Mirai-hydrogen-fuel-cell-vehicle> (accessed December 24, 2022).
- [11] 2022 Nexo Fuel Cell | Vehicle Overview | Hyundai USA, (n.d.). <https://www.hyundaiusa.com/us/en/vehicles/nexo> (accessed December 24, 2022).
- [12] Residential Fuel Cell ENE-FARM | Challenge Zero, (n.d.). <https://www.challenge-zero.jp/en/casestudy/469> (accessed December 24, 2022).
- [13] New DLR-HY4 - The First Hydrogen-Powered Aircraft Debuts At Stuttgart Airport - FuelCellsWorks, (n.d.). <https://fuelcellsworks.com/news/new-dlr-hy4-the-first-hydrogen-powered-aircraft-debuts-at-stuttgart-airport/> (accessed December 24, 2022).
- [14] H3 DYNAMICS | Global Decarbonization of Air Mobility: From Autonomous Aerial Services to Hydrogen Aviation., (n.d.). <https://www.h3dynamics.com/> (accessed December 24, 2022).
- [15] N. Gavrilovic, D. Vincekovic, J.-M. Moschetta, A Long Range Fuel Cell / Soaring UAV System for Crossing the Atlantic Ocean, Inst. Teknol. Sepuluh Nop. Surabaya. (2019) 121–131.

- [16] H.L. Nguyen, J. Han, X.L. Nguyen, S. Yu, Y.-M. Goo, D.D. Le, Review of the Durability of Polymer Electrolyte Membrane, (2021).
- [17] N. Macauley, D.D. Papadimas, J. Fairweather, D. Spornjak, D. Langlois, R. Ahluwalia, K.L. More, R. Mukundan, R.L. Borup, Carbon Corrosion in PEM Fuel Cells and the Development of Accelerated Stress Tests, *J. Electrochem. Soc.* 165 (2018) F3148–F3160. <https://doi.org/10.1149/2.0061806jes>.
- [18] Z.A.R. Gautama, Y.A. Hutapea, B. Hwang, J. Matsuda, A. Mufundirwa, T. Sugiyama, M. Ariyoshi, S. Fujikawa, S.M. Lyth, A. Hayashi, K. Sasaki, M. Nishihara, Suppression of radical attack in polymer electrolyte membranes using a vinyl polymer blend interlayer with low oxygen permeability, *J. Memb. Sci.* 658 (2022). <https://doi.org/10.1016/j.memsci.2022.120734>.
- [19] P.T. Moseley, *Fuel Cell Systems Explained*, 2001. [https://doi.org/10.1016/s0378-7753\(00\)00571-1](https://doi.org/10.1016/s0378-7753(00)00571-1).
- [20] T. Abdel-Baset, T. Benjamin, R. Borup, K.E. Martin, N. Garland, S. Hirano, J. Kopasz, B. Lakshmanmn, D. Masten, M. Mehall, D. Myers, D. Papageorgopoulos, W. Podolski, T. Trabold, B. Vermeersch, J. Waldecker, The US Department of Energy (DOE). Energy Efficiency and Renewable Energy <https://energy.gov/eere/fuelcells/doe-technical-targets-polymer-electrolyte-membrane-fuel-cell-components>, (2017) 30. <https://doi.org/10.2172/1220127>.
- [21] U. Pasaogullari, C.Y. Wang, Liquid Water Transport in Gas Diffusion Layer of Polymer Electrolyte Fuel Cells, *J. Electrochem. Soc.* 151 (2004) A399.

<https://doi.org/10.1149/1.1646148>.

- [22] A.H. Kakaee, G.R. Molaeimanesh, M.H. Elyasi Garmaroudi, Impact of PTFE distribution across the GDL on the water droplet removal from a PEM fuel cell electrode containing binder, *Int. J. Hydrogen Energy*. 43 (2018) 15481–15491. <https://doi.org/10.1016/j.ijhydene.2018.06.111>.
- [23] Y. Tabe, Y. Aoyama, K. Kadowaki, K. Suzuki, T. Chikahisa, Impact of micro-porous layer on liquid water distribution at the catalyst layer interface and cell performance in a polymer electrolyte membrane fuel cell, *J. Power Sources*. 287 (2015) 422–430. <https://doi.org/10.1016/j.jpowsour.2015.04.095>.
- [24] S.Y. Lin, M.H. Chang, Effect of microporous layer composed of carbon nanotube and acetylene black on polymer electrolyte membrane fuel cell performance, *Int. J. Hydrogen Energy*. 40 (2015) 7879–7885. <https://doi.org/10.1016/j.ijhydene.2014.10.146>.
- [25] T. Tanuma, M. Kawamoto, S. Kinoshita, Effect of Properties of Hydrophilic Microporous Layer (MPL) on PEFC Performance, *J. Electrochem. Soc.* 164 (2017) F499–F503. <https://doi.org/10.1149/2.0371706jes>.
- [26] X.L. Wang, H.M. Zhang, J.L. Zhang, H.F. Xu, Z.Q. Tian, J. Chen, H.X. Zhong, Y.M. Liang, B.L. Yi, Micro-porous layer with composite carbon black for PEM fuel cells, *Electrochim. Acta*. 51 (2006) 4909–4915. <https://doi.org/10.1016/j.electacta.2006.01.048>.
- [27] A. Ozden, S. Shahgaldi, J. Zhao, X. Li, F. Hamdullahpur, Assessment of graphene as

- an alternative microporous layer material for proton exchange membrane fuel cells, *Fuel*. 215 (2018) 726–734. <https://doi.org/10.1016/j.fuel.2017.11.109>.
- [28] M.A. Abdelkareem, E.T. Kasem, N. Nakagawa, E.A.M. Abdelghani, A.A. Elzatahry, K.A. Khalil, N.A.M. Barakat, Enhancement of the passive direct methanol fuel cells performance by modification of the cathode microporous layer using carbon nanofibers, *Fuel Cells*. 14 (2014) 607–613. <https://doi.org/10.1002/fuce.201300279>.
- [29] D. Ye, E. Gauthier, J.B. Benziger, M. Pan, Bulk and contact resistances of gas diffusion layers in proton exchange membrane fuel cells, *J. Power Sources*. 256 (2014) 449–456. <https://doi.org/10.1016/j.jpowsour.2014.01.082>.
- [30] C. Simon, D. Kartouzian, D. Müller, F. Wilhelm, H.A. Gasteiger, Impact of Microporous Layer Pore Properties on Liquid Water Transport in PEM Fuel Cells: Carbon Black Type and Perforation, *J. Electrochem. Soc.* 164 (2017) F1697–F1711. <https://doi.org/10.1149/2.1321714jes>.
- [31] J.E. Owejan, P.T. Yu, Mitigation of Carbon Corrosion in Non-Active Layers Using Graphitized Carbon Black in PEM Fuel Cells, *ECS Meet. Abstr.* MA2007-02 (2007) 593–593. <https://doi.org/10.1149/ma2007-02/9/593>.
- [32] W.M. Yan, D.K. Wu, X.D. Wang, A.L. Ong, D.J. Lee, A. Su, Optimal microporous layer for proton exchange membrane fuel cell, *J. Power Sources*. 195 (2010) 5731–5734. <https://doi.org/10.1016/j.jpowsour.2010.03.041>.
- [33] H. Gharibi, M. Javaheri, R.A. Mirzaie, The synergy between multi-wall carbon nanotubes and Vulcan XC72R in microporous layers, *Int. J. Hydrogen Energy*. 35

- (2010) 9241–9251. <https://doi.org/10.1016/j.ijhydene.2009.08.092>.
- [34] G. Bin Jung, W.J. Tzeng, T.C. Jao, Y.H. Liu, C.C. Yeh, Investigation of porous carbon and carbon nanotube layer for proton exchange membrane fuel cells, *Appl. Energy*. 101 (2013) 457–464. <https://doi.org/10.1016/j.apenergy.2012.08.045>.
- [35] A. Bottino, G. Capannelli, A. Comite, C. Costa, A.L. Ong, Microporous layers based on poly(vinylidene fluoride) and sulfonated poly(vinylidene fluoride), *Int. J. Hydrogen Energy*. 40 (2015) 14690–14698. <https://doi.org/10.1016/j.ijhydene.2015.08.099>.
- [36] M. Sarker, M.A. Rahman, F. Mojica, S. Mehrazi, W.J.M. Kort-Kamp, P.Y.A. Chuang, Experimental and computational study of the microporous layer and hydrophobic treatment in the gas diffusion layer of a proton exchange membrane fuel cell, *J. Power Sources*. 509 (2021). <https://doi.org/10.1016/j.jpowsour.2021.230350>.
- [37] A. Öztürk, B. Fıçıcılar, İ. Eroğlu, A. Bayrakçeken Yurtcan, Facilitation of water management in low Pt loaded PEM fuel cell by creating hydrophobic microporous layer with PTFE, FEP and PDMS polymers: Effect of polymer and carbon amounts, *Int. J. Hydrogen Energy*. 42 (2017) 21226–21249. <https://doi.org/10.1016/j.ijhydene.2017.06.202>.
- [38] H. Sadeghifar, In-plane and through-plane electrical conductivities and contact resistances of a Mercedes-Benz catalyst-coated membrane, gas diffusion and microporous layers and a Ballard graphite bipolar plate: Impact of humidity, compressive load and polytetrafluoroe, *Energy Convers. Manag.* 154 (2017) 191–202.

<https://doi.org/10.1016/j.enconman.2017.10.060>.

- [39] H. Sadeghifar, N. Djilali, M. Bahrami, Thermal conductivity of a graphite bipolar plate (BPP) and its thermal contact resistance with fuel cell gas diffusion layers: Effect of compression, PTFE, micro porous layer (MPL), BPP out-of-flatness and cyclic load, *J. Power Sources*. 273 (2015) 96–104. <https://doi.org/10.1016/j.jpowsour.2014.09.062>.
- [40] Q. Zhang, T. Gu, R. Shi, J. Yan, W. Wang, W. Qian, B. Zhai, M. Zhou, M. Chai, R. Yang, Silane-functionalized carbon with super-hydrophobicity advancing microporous layer for proton exchange membrane fuel cells, *J. Power Sources*. 555 (2023) 232342. <https://doi.org/10.1016/j.jpowsour.2022.232342>.
- [41] O.R. Brown, Graphite Fluorides, 1989. [https://doi.org/10.1016/0013-4686\(89\)87102-6](https://doi.org/10.1016/0013-4686(89)87102-6).
- [42] X. Dong, X. Zhao, L. Wang, M. Zhang, One-step synthesis of hydrophobic fluorinated ordered mesoporous carbon materials, *RSC Adv.* 6 (2016) 48870–48874. <https://doi.org/10.1039/c6ra06583j>.
- [43] S.M. Lyth, W. Ma, J. Liu, T. Daio, K. Sasaki, A. Takahara, B. Ameduri, Solvothermal synthesis of superhydrophobic hollow carbon nanoparticles from a fluorinated alcohol, *Nanoscale*. 7 (2015) 16087–16093. <https://doi.org/10.1039/c5nr03484a>.
- [44] S.G. Peera, A. Arunchander, A.K. Sahu, Platinum nanoparticles supported on nitrogen and fluorine co-doped graphite nanofibers as an excellent and durable oxygen reduction catalyst for polymer electrolyte fuel cells, *Carbon N. Y.* 107 (2016) 667–

679. <https://doi.org/10.1016/j.carbon.2016.06.021>.

- [45] S. Akula, B. Balasubramaniam, P. Varathan, A.K. Sahu, Nitrogen-Fluorine Dual Doped Porous Carbon Derived from Silk Cotton as Efficient Oxygen Reduction Catalyst for Polymer Electrolyte Fuel Cells, *ACS Appl. Energy Mater.* 2 (2019) 3253–3263. <https://doi.org/10.1021/acsaem.9b00100>.
- [46] D.E. Glass, V. Galvan, M. Iulliucci, G.K.S. Prakash, Optimization of platinum loading on partially fluorinated carbon catalysts for enhanced proton exchange membrane fuel cell performance, *J. Power Sources.* 542 (2022). <https://doi.org/10.1016/j.jpowsour.2022.231725>.
- [47] J.M. Kim, Y.J. Lee, S. hoon Kim, K.H. Chae, K.R. Yoon, K.A. Lee, A. Byeon, Y.S. Kang, H.Y. Park, M.K. Cho, H.C. Ham, J.Y. Kim, High-performance corrosion-resistant fluorine-doped tin oxide as an alternative to carbon support in electrodes for PEM fuel cells, *Nano Energy.* 65 (2019). <https://doi.org/10.1016/j.nanoen.2019.104008>.
- [48] S.G. Peera, A.K. Sahu, A. Arunchander, S.D. Bhat, J. Karthikeyan, P. Murugan, Nitrogen and fluorine co-doped graphite nanofibers as high durable oxygen reduction catalyst in acidic media for polymer electrolyte fuel cells, *Carbon N. Y.* 93 (2015) 130–142. <https://doi.org/10.1016/j.carbon.2015.05.002>.
- [49] O.M. Orogbemi, D.B. Ingham, M.S. Ismail, K.J. Hughes, L. Ma, M. Pourkashanian, The effects of the composition of microporous layers on the permeability of gas diffusion layers used in polymer electrolyte fuel cells, *Int. J. Hydrogen Energy.* 41

(2016) 21345–21351. <https://doi.org/10.1016/j.ijhydene.2016.09.160>.

## **Chapter 2. Experimental Methods**

### **2.1 Synthesis of Fluorinated Carbon Powders**

In this research, fluorinated carbon powders were synthesized by solvothermal decomposition reaction between fluorotelomer alcohols and sodium metal. This synthesis method is a unique, one-step method which was developed by our group [1]. Fluorotelomer alcohol and sodium metal were put in a PTFE crucible (Figure 2.1a) under flowing nitrogen to decrease contamination from air. After placing the lid on the PTFE crucible, it was enclosed in a stainless-steel jacket in a pre-heated oven at 150 °C for 24 hours. After heating, the stainless-steel container was left to cool down to room temperature, after which the lid was carefully opened in a well-ventilated fume hood. The resulting product inside the PTFE crucible was already carbonized after the reaction without the requirement for an additional pyrolysis step. The product was directly tipped into a 2 litre beaker filled with a mixture of deionised water and ethanol. After magnetic stirring for 24 hours, the product was vacuum-filtered and dried in an oven at 60 °C for an additional 24 hours. A more detailed explanation of the synthesis is discussed in Chapter 3.

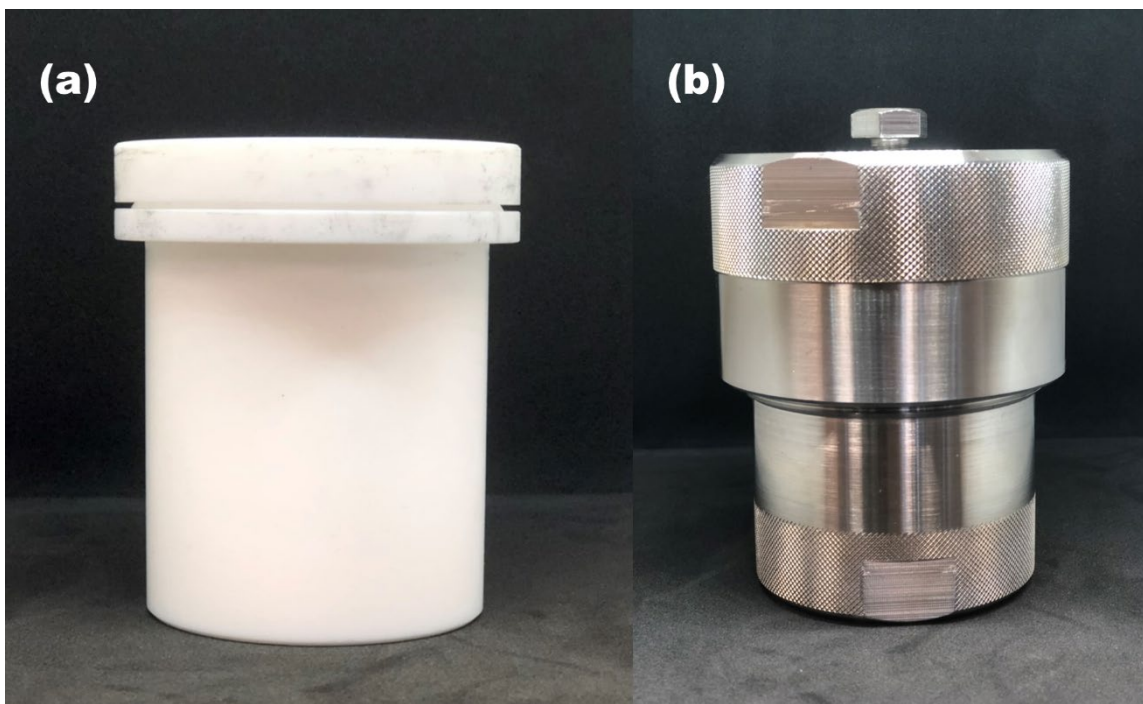


**Figure 2.1** Photos of (a) PTFE crucible, (b) stainless-steel jacket.

## **2.2 Material Characterization Techniques**

### **2.2.1 Scanning Electron Microscopy (SEM)**

The morphology and microstructure of the samples were characterized by field emission scanning electron microscopy (FE-SEM, JEOL JSM-7001F, WDS, EDS, 25 kV). Fluorinated carbon powders were scattered onto one side of a double-sided carbon tape and then stuck onto a sample holder. To avoid contamination of the SEM's vacuum chamber, excess powder was removed via an air blower.

### **2.2.2 X-ray Photoelectron Spectroscopy (XPS)**

X-ray photoelectron spectroscopy (XPS) is a non-destructive surface characterization technique to investigate the elemental composition and chemical structure of materials [2]. Due to the measurement depth of 10 nm, XPS mostly provides information near the surface of a material. Photoelectrons are produced from a material when the energy of the impinging photons exceed the binding energy of electrons in that material. Irradiation of the sample is generally done by single energy X-ray photons (monochromatic X-rays, commonly Mg K $\alpha$ , 1253.6 eV or Al K $\alpha$ , 1486 eV) in ultra-vacuum conditions. The energy of the produced photoelectrons is characteristic of the irradiated elements within the material. The emitted photoelectrons are collected by an electron energy analyser that measures the kinetic energy of the emitted electrons. Since the kinetic energy of the emitted electron is related to the binding energy of each electron, and as atoms have various orbitals with different binding energy as well as kinetic energy, the analyser produces XPS spectra.

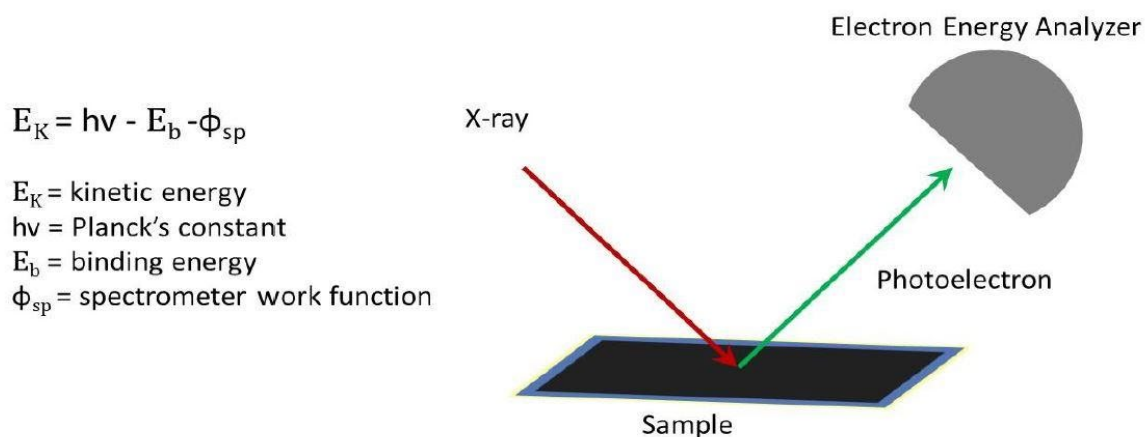


**Figure 2.2 Principle of X-ray photoelectron spectroscopy (XPS) [3].**

A high-resolution XPS analyser (PHI 5000 Vera Probe II, ULVAC-PHI, INC) was used to perform XPS analysis under ultra-high vacuum conditions (Figure 2.3). To prepare samples for XPS measurement, a small amount of fluorinated carbon was placed on a piece of indium foil. Carbon powders were pressed into the foil using a spatula to create a smooth continuous surface. The indium foil with the sample was then attached to the sample holder using double sided carbon tape. Survey spectra and narrow scan spectra of the carbon, fluorine, oxygen, and sodium regions were performed on all samples. The measurement conditions are given in Table 2.1.

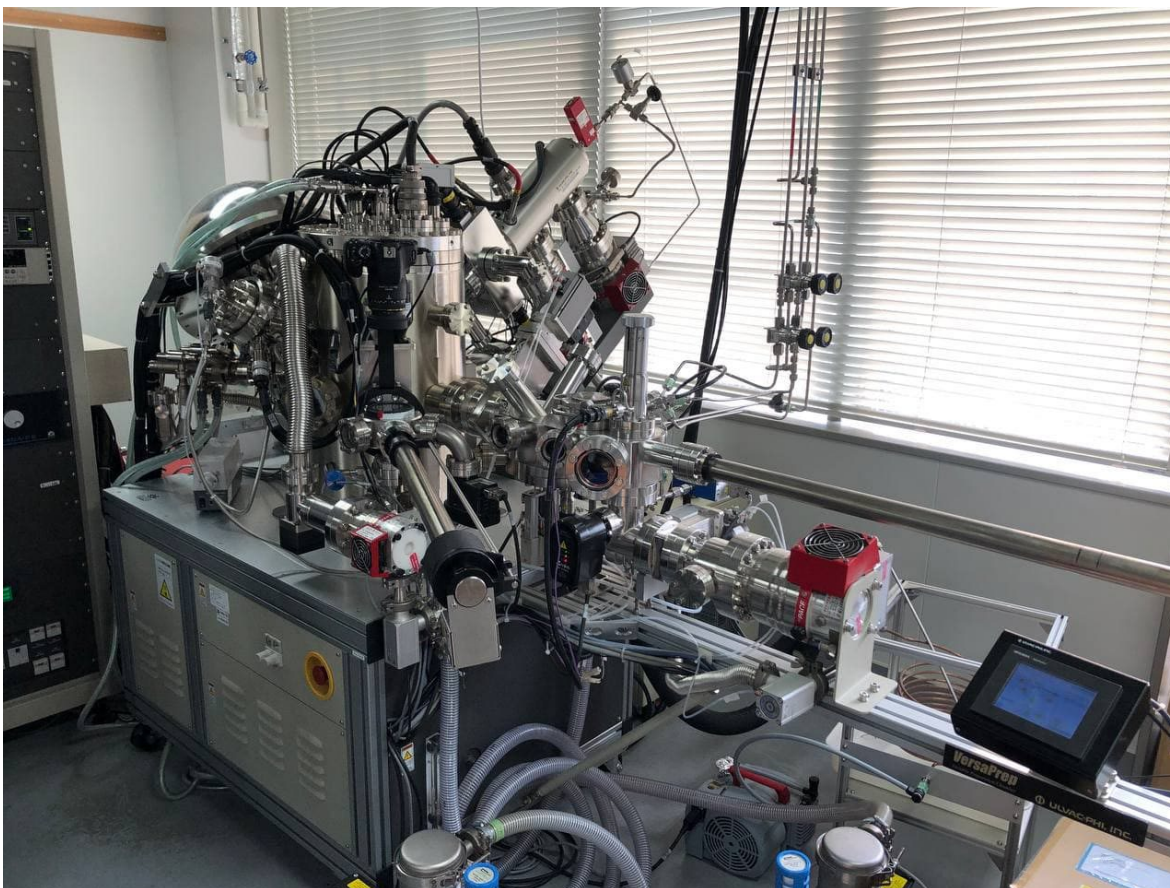


**Figure 2.3 Photo of XPS analysis equipment.**

**Table 2.1 XPS analysis measurement conditions.**

Element	Number of Sweeps	Pass energy (eV)	eV Step
Wide scan	20	187.85	0.2
C 1s	50	46.95	0.1
F 1s	100	46.95	0.1
O 1s	50	46.95	0.1
Na 1s	50	46.95	0.1

CasaXPS software was used to analyse and deconvolute the spectra. The binding energies were calibrated based to the  $sp^3$  peak of the C 1s peak at 284.5 eV. For XPS deconvolution, a Shirley type background subtraction was used with the Gaussian-Lorentzian sum (50/50) line shape. The FWHM values were fixed between 1.2 eV to 1.3 eV for most of the peaks.

### **2.2.3 Energy Dispersive X-ray Analysis (EDX)**

To characterize the bulk elemental composition of the samples, energy dispersive X-ray analysis was used (EDX). EDX makes use of the X-ray spectrum emitted by a solid sample bombarded with a focused beam of electrons to obtain a localized chemical structure. EDX analysis was performed with the same equipment used for SEM imaging. Compared to XPS, EDX has a measurement depth of  $\sim 2\text{ }\mu\text{m}$ , meaning that it is not as sensitive to the surface, and can be regarded as a bulk measurement technique [4].

### 2.2.4 X-ray Diffraction (XRD)

The X-ray diffraction (XRD) was used to characterize the atomic or molecular structure of the material. It is a non-destructive X-ray technique and provides information on crystallinity, crystal size, interatomic spacing, and interlayer spacing of the material [5,6]. XRD is based on the constructive interference of monochromatic X-rays and a crystalline sample. By measuring the angle and intensity of the diffracted beam, the crystal lattice spacing can be calculated using Bragg's Equation (Eq. 2.1).

$$n\lambda = 2d\sin\theta \quad \text{Eq. 2.1}$$

Here,  $n$  is a positive integer,  $\lambda$  is the X-ray wavelength,  $d$  is the interlayer spacing, and  $\theta$  is the angle between the incident X-ray and scattering planes. Figure 2.4 shows the principle of X-ray diffraction (XRD) according to Bragg's law [7].

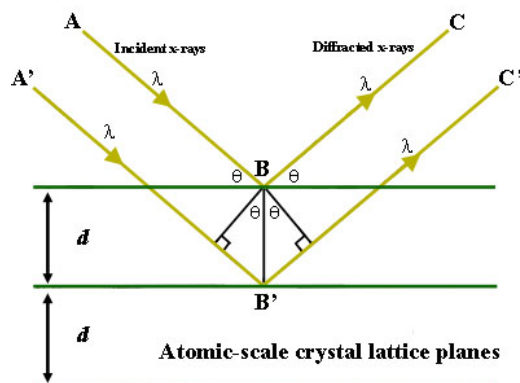


Figure 2.4 Principle of XRD according to Bragg's law [7].

In this thesis, XRD was used to analyse the crystallinity and structure of fluorinated carbons as well as the effect of fluorination on crystallinity and structure of the carbon. A Rigaku

Smartlab X-ray Diffractometer was used for this measurement (Figure 2.5). The radiation source was a Cu K $\alpha$  with a wavelength of 1.5418 Å.



**Figure 2.5 Rigaku Smartlab X-Ray Diffractometer.**

### **2.2.5 Transmission Electron Microscopy (TEM) & Selected Area Electron Diffraction (SAED)**

Transmission electron microscopes (TEM) use a particle beam of electrons to visualise the sample with high resolution. An electron gun is employed at the top of the TEM which emits

electrons that travel through the TEM vacuum tube. An electromagnetic lens is used to focus electrons into a very fine beam. To allow the beam to pass through the specimen to produce clear images, the samples should be very thin (around 100 nm). A simplified diagram of a TEM is given in Figure 2.6 [8]. A selected area electron diffraction (SAED), a crystallographic technique, is performed by using a TEM. A SAED pattern is obtained in the k-space of lattice planes. SAED images give information about crystallinity of the material. In this work, a conventional TEM (TEM, Titan<sup>TM</sup> ETEM G2, FEI Company) at an acceleration voltage of 100 kV was used to observe the nanostructures of fluorinated carbons and to determine the lattice spacing of graphitic shells. Samples were prepared by dispersing 100 µg of catalyst powder in 1 ml ethanol, followed by sonication to make a homogenous dispersion. A few drops were added to a holey carbon-coated Cu TEM grid, and the solvent was allowed to evaporate.

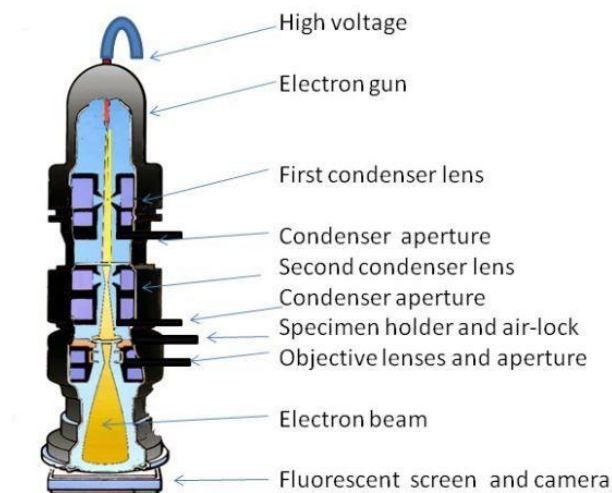


**Figure 2.6 A simplified diagram of a TEM [8].**

### 2.2.6 Raman Spectroscopy

Raman spectroscopy is a light scattering non-destructive chemical analysis technique, which provides information on the crystallinity, molecular interaction, and chemical structure of materials [9]. This vibrational spectroscopy works based on the inelastic light scattering that emits when the specimen is irradiated by a light from a monochromatic light source. Raman spectroscopy is therefore an important technique for carbonaceous materials. In this study, the graphitic structure of the samples was analysed, as well as the effect of fluorination on the defect of the graphitic sample. A Renishaw inVia Raman Microscope DM2500M (Figure 2.7), using an argon-ion laser with a wavelength of 532 nm, was used in this research.

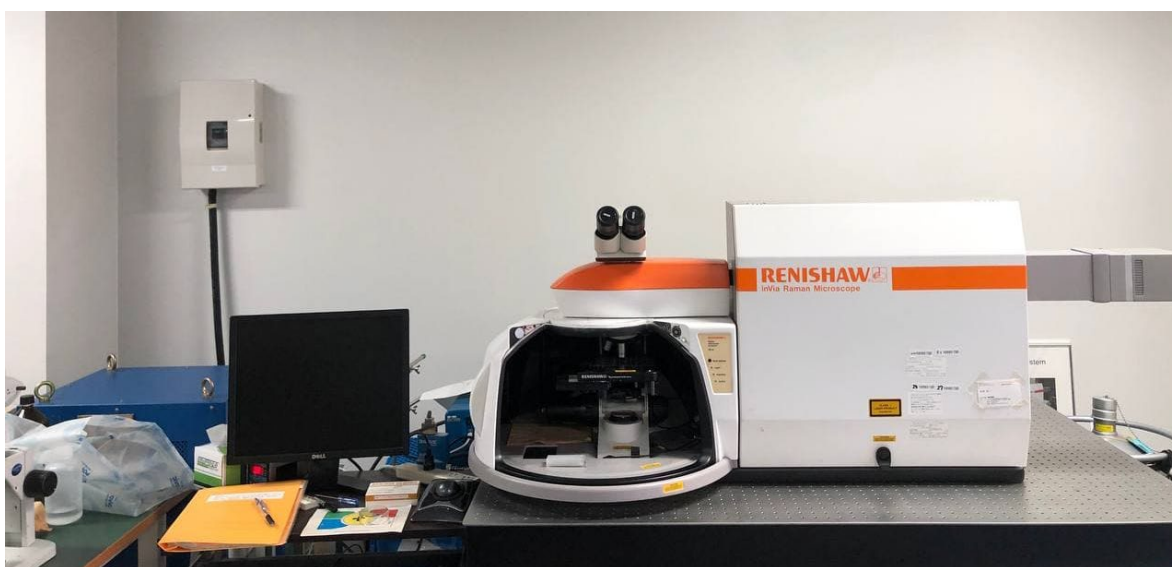


**Figure 2.7 Renishaw inVia Raman Microscope.**

### **2.2.7 Surface Area and Pore Size Distribution Analysis**

Nitrogen gas adsorption takes advantage of the fact that nitrogen gas molecules can physically adsorb on solid surfaces at cryogenic temperatures (77 K), due to van der Waals forces [10]. Here, samples were carefully weighed, and placed inside glass tubes. After attaching the sample tube to the machine, they were degassed using a pre-treatment unit at 200 °C under vacuum for 2 hours (Figure 2.8 (a)). Then the sample tubes were transferred and mounted onto the N<sub>2</sub> adsorption/desorption equipment (Belsorp-mini, BEL Japan, Inc, Figure 2.8 (b)), equipped with a liquid nitrogen container. The glass cells were then submerged into liquid nitrogen, and the amount of adsorbed gas was measured as the pressure increases. The recorded isotherms can be used to determine the surface area using Brunauer Emmet and Teller (BET) analysis, and porosity parameters using MP-plots, T-plots, and Barrett Joyner and Halenda (BJH) analysis.

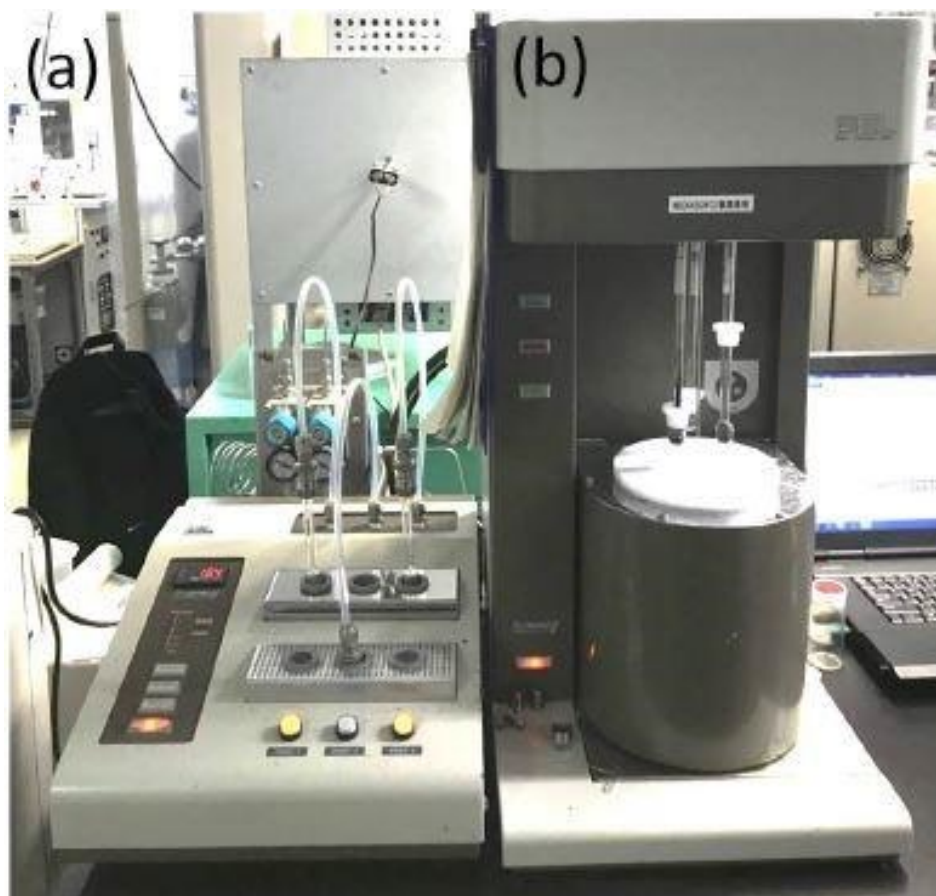


**Figure 2.8 Photo of the nitrogen gas adsorption/desorption equipment (Belsorp-mini, BEL Japan)**

### **2.2.8 Thermogravimetric Analysis (TGA)**

Thermogravimetric analysis (with a Rigaku Corp., Thermo plus EVO2) (Figure 2.9) was conducted under constant air flow of 25 sccm to investigate the thermal stability of the fluorinated carbon. Samples were placed in a 100  $\mu$ l platinum container and heated to 1000  $^{\circ}$ C with an increment of 10  $^{\circ}$ C per minute, starting from room temperature whilst the mass loss was recorded.

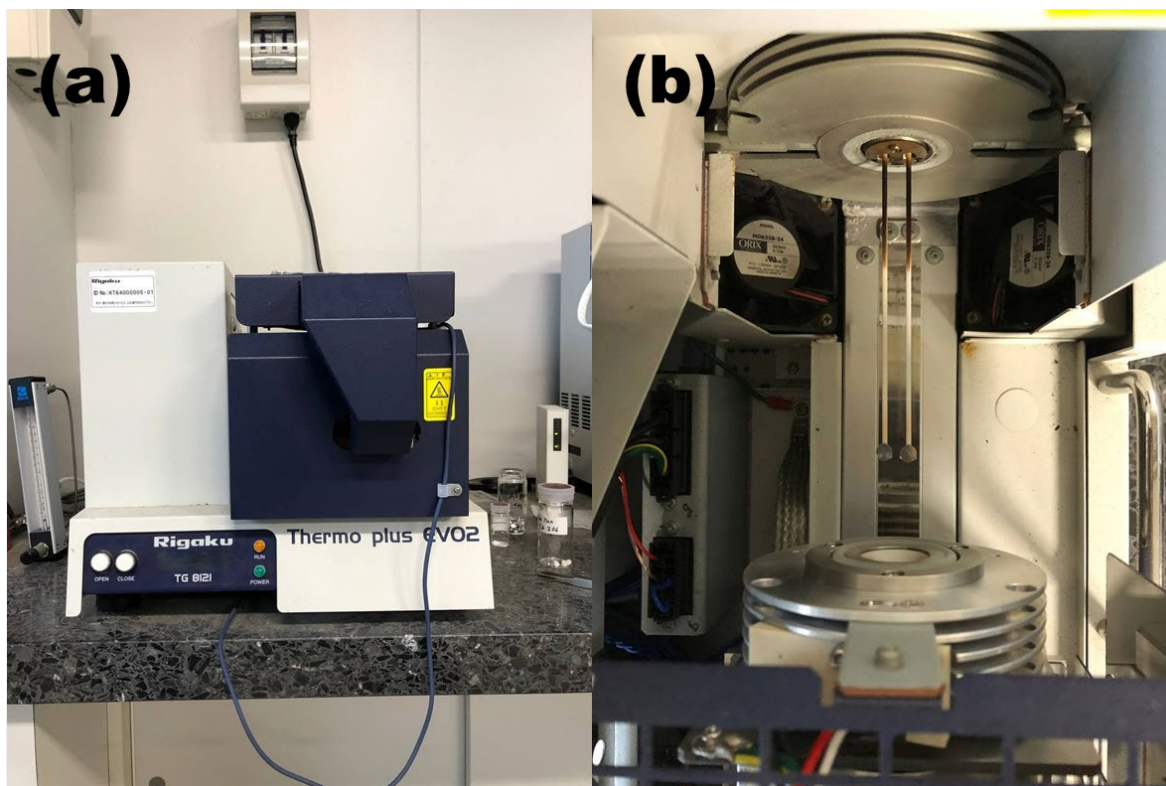


**Figure 2.9 Thermogravimetric analysis Equipment.**

## **2.3 Electrochemical Characterization Techniques**

### **2.3.1 Microporous Layer (MPL) Manufacturing and Coating**

In this thesis two different types of MPL were used, based on (i) carbon black (CB-MPL) and (ii) based on the synthesized fluorinated carbons (FC-MPL). Slurries were prepared by mixing carbon powder, deionized water, and 60 wt.% PTFE solution via sonication. Then the slurry was coated onto GDLs using the doctor blade technique (Figure 2.10). The thickness of the MPL coating was adjusted by varying the thickness of the stainless-steel frame. After coating the MPL, the GDLs were dried in an oven at 65 °C for an

hour and heat treated in a furnace at 380 °C temperature. Figure 2.11 shows a photo of a MPL coated GDL. The details of the manufacturing and coating of MPLs are further explained in Chapter 4.

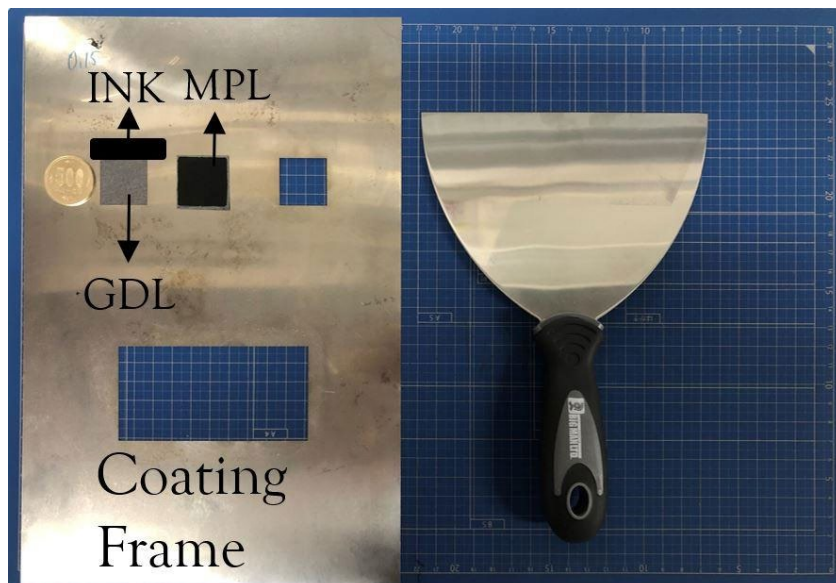


**Figure 2.10** Photo of the stainless-steel frame used for MPL coating using the doctor blade technique.

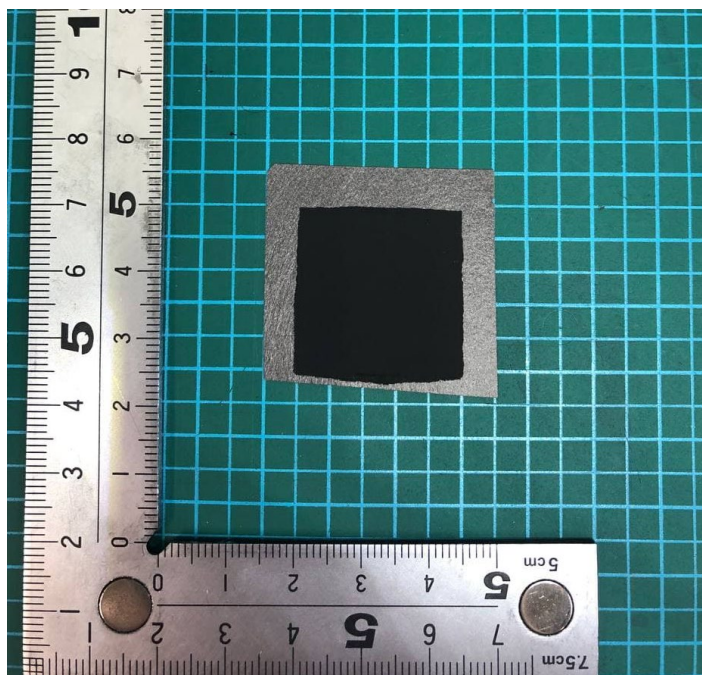


**Figure 2.11 Photo of a MPL coated GDL.**

### **2.3.2 Water Contact Angle Measurement of MPLs**

To determine the hydrophobicity of the synthesised fluorinated carbons and the fabricated MPLs, water contact angle (WCA) measurements were conducted using the Pendant Drop Method. An automated WCA measurement device (DMs-401, Kyowa Interface Science Co., Ltd, Japan) was used for measurement (Figure 2.12).

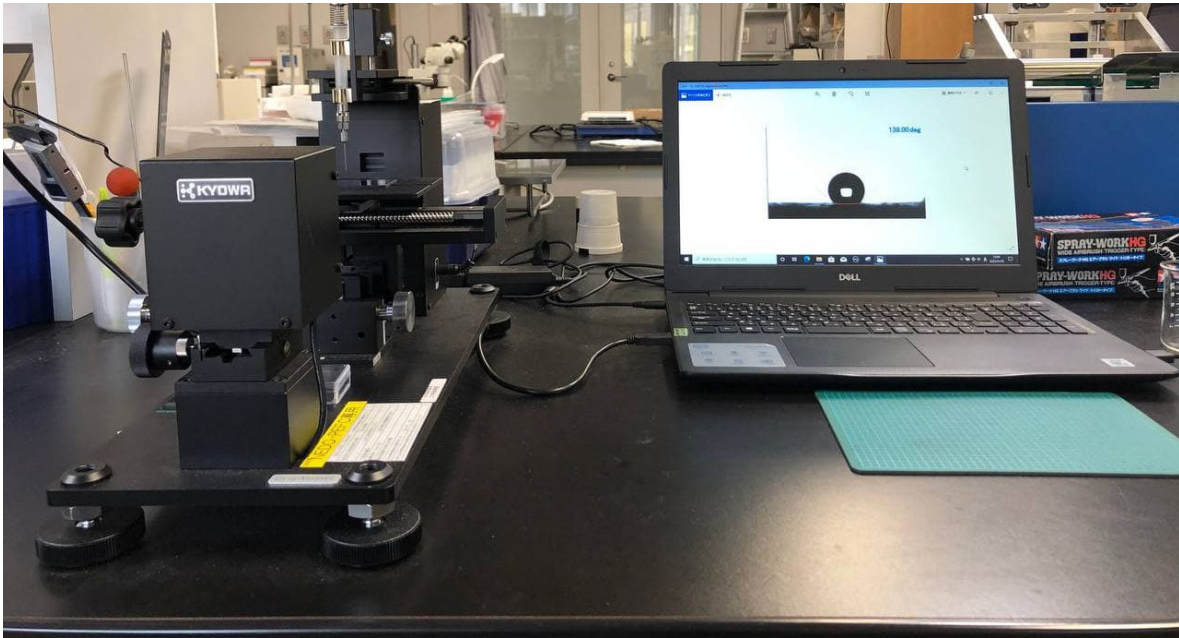


**Figure 2.12 Photo of WCA measurement equipment.**

### **2.3.3 Air Permeability Test of MPLs**

Through-plane air permeability tests were conducted on the MPL-coated GDLs under ambient conditions with dry air flow, using a home-made system (Figure 2.13) [11]. The GDLs were compressed at 1 MPa during the measurements, which is similar to the compression within a single PEFC cell. This test protocol is similar to that of the Gurley method [5].

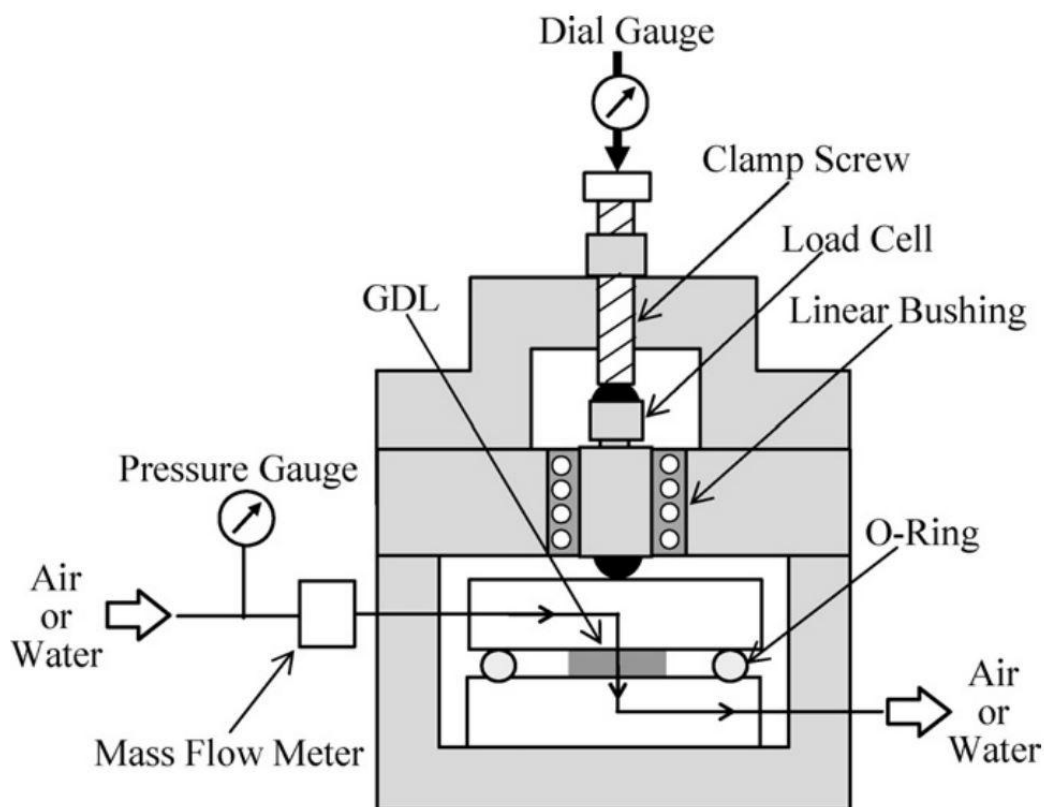


**Figure 2.13 Schematic diagram of air permeability test equipment [11].**

### **2.3.4 Membrane Electrode Assembly Preparation (MEA)**

The catalyst ink was prepared by mixing Pt/C (TEC10E50E, lot 1019-8581, 46.8 wt.Pt%, Tanaka, Japan) with 5 wt% Nafion solution (Wako, Japan), deionized water, and super-dehydrated ethanol (99.5 vol%, Wako, Japan). The catalyst ink was stirred overnight, then sonicated for 30 min just before use (SMT Corporation, Ultra Sonic Homogenizer UH- 600). Nafion 212 membranes were placed onto movable-hot plate and masked, leaving an exposed area of 1 cm<sup>2</sup>. The catalyst ink was then sprayed directly onto the Nafion membrane using pulsed spray mode from an automated spraying device (Nordson K.K., C3J) (Figure 2.14

(a)), with a catalyst loading of  $0.3 \text{ mgPt/cm}^2$  and a Nafion content of 28 wt% [12], at both the anode and cathode. The resulting MEAs were finally hot pressed at  $132^\circ\text{C}$  and  $0.3 \text{ kN}$  for 180 s (Sinto Digital Press CYPT-10) (Figure 2.14 (b)). Figure 2.15 shows a photo of a catalyst coated membrane after hot pressing.



**Figure 2.14 (a) Nordson K.K. Spraying Device, (b) Sinto Digital Press CYPT-10.**



**Figure 2.15 Photo of catalyst coated membrane.**

### **2.3.5 Polymer Electrolyte Fuel Cell (PEFC) Testing**

Fuel cell tests were performed using a single cell with an active area of  $1 \text{ cm}^2$  obtained from the Japanese Automotive Research Institute (JARI) with serpentine type flow fields. Photo of PEFC single cell with its parts is given in Figure 2.16.

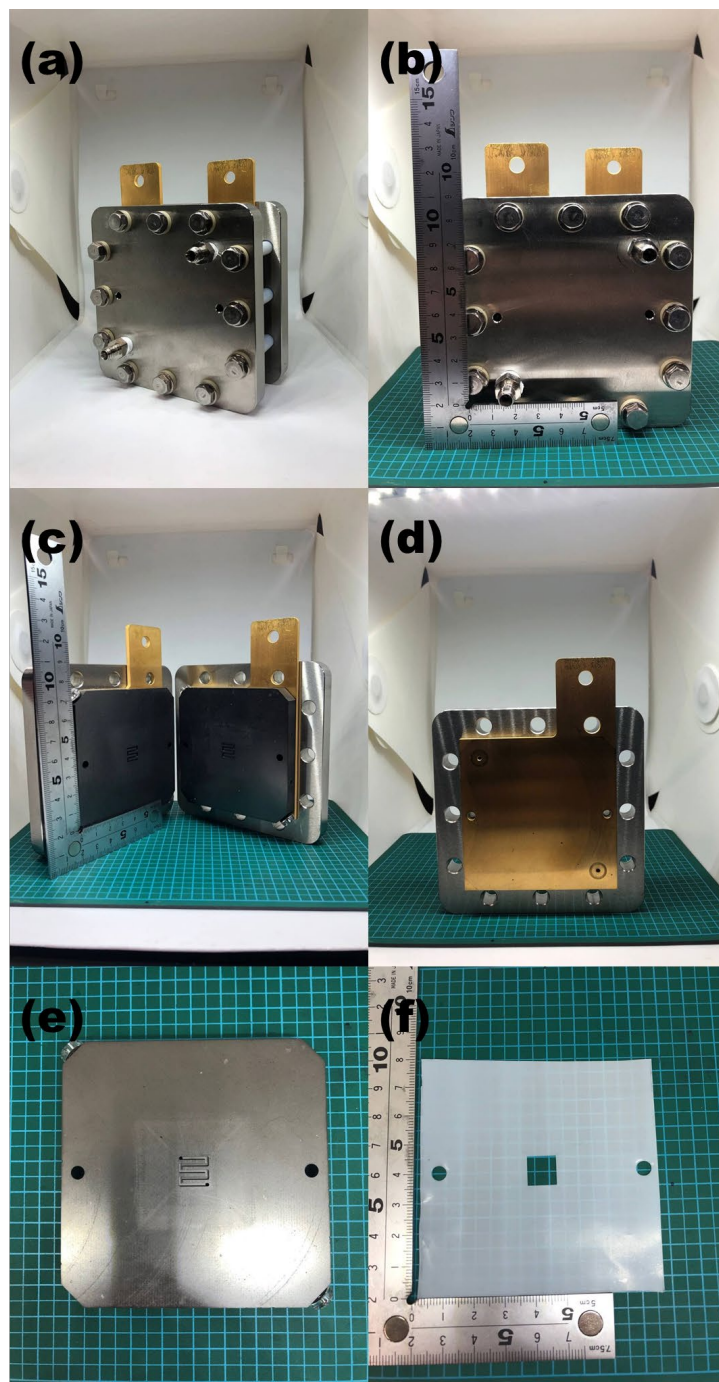


**Figure 2.16** Photos of components of a single cell for PEFC performance test, (a-b) assembled single cell, (c) graphite flow channel, gold coated current collector, and end plate, (d) gold coated current collector and end plate, (e) gasket with 150  $\mu\text{m}$  thickness.

The performance of the different MPL-coated GDLs was investigated by measuring polarization curves at two different cell temperatures (45 °C and 80 °C). The temperature of 80 °C was selected to reproduce conventional PEFCs operating conditions. The lower temperature of 45 °C was selected as an extreme condition in which water condensation readily causes flooding even at lower current density, to highlight the effect of using superhydrophobic MPLs. Three different conditions of relative humidity (RH) were also tested (80%, 100%, 120%) at both the anode and cathode. To reach 120% relative humidity with a cell temperature of 80 °C, the humidifier temperature was maintained at 85 °C. For a cell temperature of 45 °C, the humidifier was maintained at 49 °C. Fuel cell performance tests at 120% RH and 80 °C are not shown because of water condensation in uninsulated sections of the pipes between the cell and the humidifier (85 °C), disrupting the gas flow and preventing stable cell I–V performance from being measured. The constant volumetric flow rates were 0.139 L/min hydrogen and 0.332 L/min oxygen at anode and cathode, respectively (counter flow conditions). A fuel cell test station (AUTOPEM-CVZ01, Toyo Corporation, Japan, Figure 2.17) was used to control the humidification, cell temperature, and gas flow. Polarization curves were measured using an electrochemical interface impedance analyser (Solartron SI-1287). Prior to the polarization curve measurement, each cell was conditioned at 0.6 V for 5 h.



**Figure 2.17 PEFC test station (AUTOPEM-CVZ01, Toyo Corporation, Japan).**

### **2.3.6 Oxygen Transport Resistance Test**

The total oxygen transport resistance was calculated from the limiting current density under the differential relative humidity conditions of the supplied gases, using the following equation [13]:

$$R_T = \frac{4 \cdot F \cdot P_{O_2}}{i_{lim} \cdot R \cdot T} \quad \text{Eq. 2.2}$$

Where  $R_T$  is the total oxygen transport resistance of the cell ( $\text{sm}^{-1}$ ),  $F$  is the Faraday constant ( $96485 \text{ C mol}^{-1}$ ),  $P_{O_2}$  is the oxygen partial pressure (Pa),  $R$  is the gas constant ( $8314 \text{ J mol}^{-1}\text{K}^{-1}$ ),  $T$  is the cell temperature (K) and  $i_{lim}$  is the limiting current density at 0.2 V.

The oxygen transport resistance was calculated at both 80 °C and 45 °C cell temperature conditions for each different MPL. At high cell temperature, the oxygen transport resistance was measured at relative humidity of 80, 100, and 120 %. At low cell temperature, the oxygen transport resistance was measured at 80, 100, 120, 160, and 200 % relative humidity. The flow rate of the supplied gases at both the anode and cathode was 1 L/min. The oxygen concentration was 2 vol% at the cathode side, and nitrogen was used as the balance gas.

## 2.4 References

- [1] S.M. Lyth, W. Ma, J. Liu, T. Daio, K. Sasaki, A. Takahara, B. Ameduri, Solvothermal synthesis of superhydrophobic hollow carbon nanoparticles from a fluorinated alcohol, *Nanoscale*. 7 (2015) 16087–16093. <https://doi.org/10.1039/c5nr03484a>.
- [2] N. Fairely, CasaXPS Manual 2.3. 15, Casa Softw. Ltd. (2009) 1–177. <http://scholar.google.com/scholar?hl=en&btnG=Search&q=intitle:CasaXPS+Manual+2.3.15#2>.
- [3] A. Mufundirwa, An Investigation of the Formation of Active Sites in Fe-N-C Electrocatalysts for the Oxygen Reduction Reaction Albert Mufundirwa 2020 年 7 月 An Investigation of the Formation of Active Sites in Fe-N-C Electrocatalysts for the Oxygen Reduction Reaction By, 2020.
- [4] P.D. Ngo, Energy Dispersive Spectroscopy, *Fail. Anal. Integr. Circuits*. (1999) 205–215. [https://doi.org/10.1007/978-1-4615-4919-2\\_12](https://doi.org/10.1007/978-1-4615-4919-2_12).
- [5] I. V. Minin, O. V. Minin, *Elements of diffraction quasi-optics*, 1994.
- [6] W.F. Tivol, Selected Area Electron Diffraction and its Use in Structure Determination, *Micros. Today*. 18 (2010) 22–28. <https://doi.org/10.1017/s1551929510000441>.
- [7] Crystallography. Scattering and diffraction. The Bragg's Law, (n.d.). [https://www.xtal.iqfr.csic.es/Cristalografia/parte\\_05\\_5-en.html](https://www.xtal.iqfr.csic.es/Cristalografia/parte_05_5-en.html) (accessed December 26, 2022).
- [8] File:Electron Microscope.png - Wikimedia Commons, (n.d.). [https://commons.wikimedia.org/wiki/File:Electron\\_Microscope.png](https://commons.wikimedia.org/wiki/File:Electron_Microscope.png) (accessed December 26, 2022).
- [9] R.R. Jones, D.C. Hooper, L. Zhang, D. Wolverson, V.K. Valev, Raman Techniques: Fundamentals and Frontiers, *Nanoscale Res. Lett.* 14 (2019). <https://doi.org/10.1186/s11671-019-3039-2>.

- [10] P.M. V Raja, A.R. Barron, Physical methods in chemistry, *Nature*. 134 (1934) 366–367. <https://doi.org/10.1002/jctb.5000533702>.
- [11] T. Kitahara, H. Nakajima, K. Mori, Hydrophilic and hydrophobic double microporous layer coated gas diffusion layer for enhancing performance of polymer electrolyte fuel cells under no-humidification at the cathode, *J. Power Sources*. 199 (2012) 29–36. <https://doi.org/10.1016/j.jpowsour.2011.10.002>.
- [12] S. Takei, K. Uda, M. Nagayama, K. Sasaki, A. Hayashi, Investigation of Reducing Concentration Overvoltage toward Development of Low Pt-Loading PEFC, *J. Electrochem. Soc.* 167 (2020) 124510. <https://doi.org/10.1149/1945-7111/abac28>.
- [13] N. Nonoyama, S. Okazaki, A.Z. Weber, Y. Ikogi, T. Yoshida, Analysis of Oxygen-Transport Diffusion Resistance in Proton-Exchange-Membrane Fuel Cells, *J. Electrochem. Soc.* 158 (2011) B416. <https://doi.org/10.1149/1.3546038>.

## **Chapter 3. Synthesis and Characterization of Fluorinated Carbon Powder**

### **3.1 Introduction**

The incorporation of fluorine atoms can significantly alter the physical, chemical, and electronic properties of carbon-based materials. In particular, fluorination generally leads to enhanced hydrophobicity due to low surface free energy and reduced van der Waals interactions [1]. Fluorinated carbons are attracting considerable attention in applications including tribological coatings [2], electrodes for lithium-ion batteries [3–5], gas sensors [6], polymer electrolyte fuel cells, and water electrolysis [7,8]. A wide range of carbon-based materials have been fluorinated in the literature, with examples including carbon black [9,10], activated carbon [11], carbon fiber [12,13], carbon nanotubes [14,15], and graphene [16,17]. Meanwhile, methods for the fluorination of carbon can be mainly classified into three types: (i) direct fluorination, (ii) indirect fluorination, and (iii) plasma fluorination. The direct fluorination method involves the direct reaction of fluorine gas ( $F_2$ ) with the surface of the target carbon material at elevated temperature [18]. Meanwhile, indirect fluorination involves thermal decomposition of a fluorine source such as xenon fluoride ( $XeF_2$ ) or terbium fluoride ( $TbF_3$ ) in close proximity to the target carbon material [19–21]. Alternatively, surface functionalization of carbon materials can be achieved via plasma treatment at room temperature in carbon tetrafluoride gas ( $CF_4$ ) [14].

The properties of the resulting fluorinated carbons depend not only on the type of carbon precursor, but also on the fluorination conditions, such as the duration of the reaction, the reaction temperature, the reaction pressure, and the type of fluorine-containing precursor [22]. Depending on these parameters, the C-F bonds which are generated during the reaction can be classed as ionic, semi-ionic, or covalent [23]. Previous studies have reported that when the proportion of fluorine atoms in fluorinated graphite is small (e.g.  $x < 0.5$  in  $\text{CF}_x$ ), ionic C-F bonds are generated, resulting in relatively high electronic conductivity [23]. However, when the concentration of fluorine atoms increases, covalent bonds are reported to form, resulting in decreased electronic conductivity due to the formation of  $\text{sp}^3$  bonds [23], so different applications for fluorinated carbons may require different degrees of fluorination [1,5]. Moreover, for lithium batteries high fluorine content is preferred because C-F bonds act as electroactive species during discharge [24].

As such, it is of interest to investigate fluorinated carbons in which the amount of fluorine can be tailored to suit different applications. Several studies have focused on the effect of the fluorination parameters on the properties of the resulting fluorinated carbon materials [17,22,25,26]. Thermal annealing has been applied to different type of fluorinated carbons to gain insight into the stability of these materials. A high proportion of fluorine atoms in fluorinated graphene can be removed at mild temperatures under the inert atmosphere, but for complete removal a temperature higher than 500 °C is reported to be required [27,28]. The defluorination of carbon nanotubes has also been investigated, and it was found that single-wall carbon nanotubes fluorinated in  $\text{F}_2$  (g) at 250 °C, were completely defluorinated at 400 °C under inert atmosphere [29].

In this chapter, fluorinated carbon materials are synthesized using a unique solvothermal method from fluorotelomer alcohols (FTOHs) and sodium metal. Fluorotelomers are generally used in the production of polyfluorinated alkyl substances (PFAS), which are used in fire-fighting foams, grease-resistant papers, anti-fogging sprays and wipes [30]. The typical structure of FTOHs is  $\text{F}(\text{CF}_2\text{CF}_2)_n\text{CH}_2\text{CH}_2\text{OH}$ , where  $n$  is a number from 2 to 5 [31]. The fluorine content in the final product is tailored by changing the FTOH precursor with different chain lengths. The effect of fluorine content on the final fluorinated carbon black microstructure and chemical structure is investigated. Furthermore, the effect of thermal annealing on fluorinated carbon blacks is explored and compared with the focus on changes in microstructure of the resulting carbons. Finally, the effect of fluorine content on hydrophobicity is examined with the water contact angle (WCA) measurement.

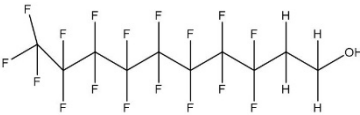
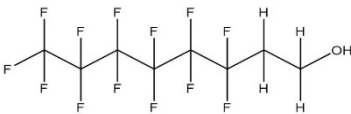
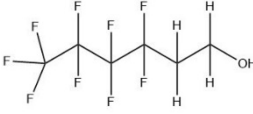
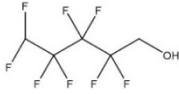
### 3.2 Experimental Methods

All chemicals were used as received from suppliers without further purification. Four fluorotelomer alcohols with different chain length were utilised as precursors for fluorinated carbon synthesis, namely: (i) perfluoro-1-decanol ( $\text{C}_{10}\text{H}_5\text{F}_{17}\text{O}$ , Fluorochem, Ltd. Japan); (ii) tridecafluorooctan-1-ol ( $\text{C}_8\text{H}_5\text{F}_{13}\text{O}$ , Funakoshi Co., Ltd., Japan); (iii) perfluorohexan-1-ol ( $\text{C}_6\text{H}_5\text{F}_9\text{O}$ , Sigma Aldrich, Japan); and (iv) octafluoro-1-pentanol ( $\text{C}_5\text{H}_4\text{F}_8\text{O}$ , Sigma Aldrich, Japan). 0.022 mol of each respective fluorotelomer alcohol was pipetted into 100 ml polytetrafluoroethylene (PTFE) crucibles (Flon Industry, Japan), followed by the addition of 0.088 mol of metallic sodium lumps under flowing nitrogen. The PTFE crucible was quickly

sealed, and then screwed into a protective stainless steel jacket. This was placed into a preheated oven at 150 °C for 24 hours, then cooled naturally to room temperature.

After cooling, the stainless steel jacket was carefully unscrewed in a well-ventilated fume hood, taking precautions for the possible presence of hydrogen fluoride fumes. The black powdery product was emptied into a two-liter glass beaker filled with a 50:50 vol.% mixture of deionized water and ethanol, sonicated for one hour, and then stirred at 1000 rpm for 24 hours. The dispersion was then washed by vacuum filtration using Omnipore™ 0.2 µm filters until the filtrate reached neutral pH. Finally, the resulting black powder was dried in a convection oven at 65 °C for 24 hours. Detailed information about the reactions are presented in Table 3.1. The samples are named as CF<sub>X</sub>-C<sub>N</sub>. CF<sub>X</sub> indicates that the sample is fluorinated carbon where C<sub>N</sub> is the number of carbon atoms in the precursor that was used to synthesis of fluorinated carbon. For example, CF<sub>X</sub>-C<sub>10</sub> corresponds to fluorinated carbon synthesised using perfluoro-1-decanol (C<sub>10</sub>H<sub>5</sub>F<sub>17</sub>O), which contains 10 carbon atoms in its structure.

**Table 3.1 Summary of the fluorotelomer alcohol precursors.**

<b>Sample Name</b>	<b>Precursor Molecule</b>	<b>Precursor Structure</b>	<b>Boiling Point (Melting Point) (°C)</b>	<b>Fluorine Content in Precursor (at.%)</b>
CF <sub>x</sub> -C <sub>10</sub>	Perfluoro-1-decanol (C <sub>10</sub> H <sub>5</sub> F <sub>17</sub> O)		113 (50)	69.6
CF <sub>x</sub> -C <sub>8</sub>	Tridecafluorooctan-1-ol (C <sub>8</sub> H <sub>5</sub> F <sub>13</sub> O)		88 to 95	67.8
CF <sub>x</sub> -C <sub>6</sub>	Perfluorohexan-1-ol (C <sub>6</sub> H <sub>5</sub> F <sub>9</sub> O)		140 to 143	64.8
CF <sub>x</sub> -C <sub>5</sub>	Octafluoro-1-pentanol (C <sub>5</sub> H <sub>4</sub> F <sub>8</sub> O)		141 to 142	65.5

The fluorinated carbon products were characterized by field emission scanning electron microscopy and energy dispersive X-ray analysis (FE-SEM EDX, SU9000, Hitachi); transmission electron microscopy (TEM, Titan<sup>TM</sup> ETEM G2, FEI Company); X-ray photoelectron spectroscopy (XPS, PHI 5000 Versa probe (II) ULVAC); nitrogen adsorption analysis (Belsorp Mini X, Microtrac MRB); X-ray diffraction analysis ( $\lambda = 1.54 \text{ \AA}$ , SmartLab

9kw AMK, Rigaku); thermogravimetric analysis (TGA, Rigaku Thermo plus EV02); and Raman spectroscopy ( $\lambda = 532$  nm, inVia Raman Microscope, Renishaw). The water contact angle (WCA) was measured using the sessile drop method with an automated surface measuring instrument (DMs-401, Kyowa Interface Science Co., Ltd, Japan). Fluorinated carbon powders were pressed between two glass slides to form a smooth surface. The droplet size was set to 1  $\mu$ L.

### 3.3 Results and Discussion

On removal from the PTFE reactor, the superficial appearance of the product was similar regardless of which fluorotelomer alcohol was used as a precursor during synthesis. All four of the generated samples were observed to be a fine dry black powder, mixed with a small amount of white residue (Figure 3.1). This white residue has been identified in our previous works as sodium fluoride (NaF) [7,9], and this was largely removed during the washing stage. After the reaction the PTFE crucible was discolored and slightly deformed. This suggests that the reaction temperature exceeded the softening point of PTFE (250 °C) despite the oven temperature being just 150 °C, i.e. that the process was exothermic.

To confirm this, the progression of the reaction temperature inside the PTFE crucible was recorded using a thermocouple for sample CF<sub>x</sub>-C<sub>8</sub>. This data (Figure 3.2) shows that the temperature steadily increased for 52 minutes after the reactor was placed in the oven, towards the target temperature of 150 °C. However, when the internal temperature reached 102 °C, a rapid increase in temperature was observed, reaching 345 °C in less than a minute. After that, the temperature quickly decreased again. This data confirms that the reaction

between sodium and tridecafluorooctan-1-ol is highly exothermic, and that the reaction occurs relatively quickly. As such, the use of stainless steel or graphite reaction vessels may be more appropriate for future studies.

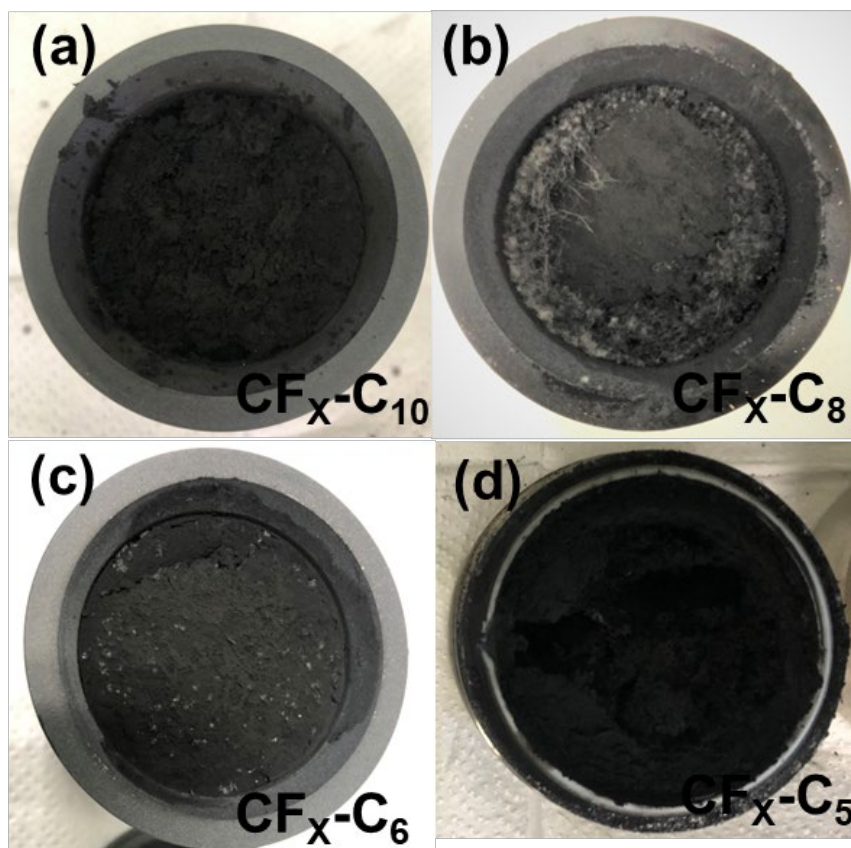


**Figure 3.1 (a) Photograph of sample (a) CF<sub>x</sub>-C<sub>10</sub>, (b) CF<sub>x</sub>-C<sub>8</sub> (c) CF<sub>x</sub>-C<sub>6</sub>, and (d) CF<sub>x</sub>-C<sub>5</sub> immediately after opening the PTFE reactor.**

The mass yields were calculated for the four different samples, which were 34, 29, 18 and 32 % for CF<sub>x</sub>-CF<sub>5</sub>, CF<sub>x</sub>-C<sub>6</sub>, CF<sub>x</sub>-C<sub>8</sub>, and CF<sub>x</sub>-C<sub>10</sub>, respectively, relative to the initial mass of the fluorotelomer precursors.

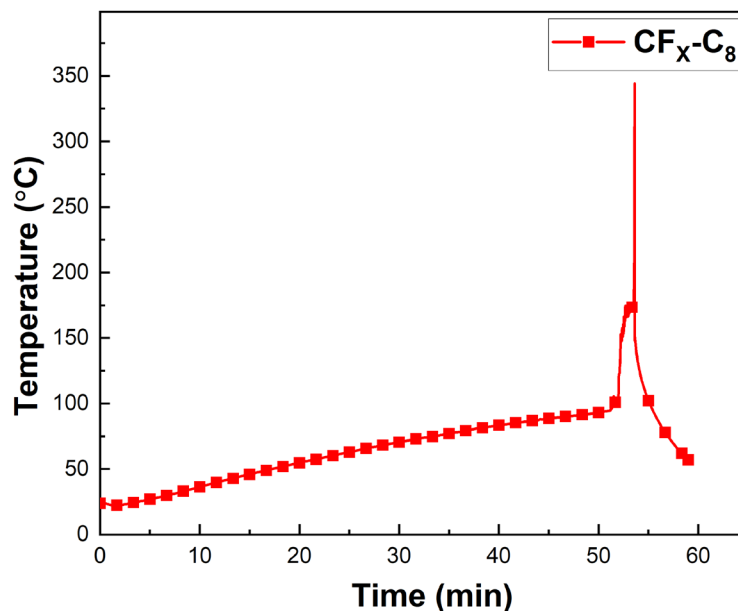


**Figure 3.2** Plot of the temperature inside the PTFE crucible during the reaction.

### 3.3.1 Scanning Electron Microscopy (SEM)

The microstructure of the four different fluorinated carbon products was first investigated by SEM (Figure 3.3). All four samples have similar microstructure and particle size distribution, regardless of the fluorotelomer precursor used. This confirms for the first time that this novel synthetic process is repeatable and can be generalized to different precursors. Each sample is comprised almost entirely of spheroidal nanoparticles with similar structure to that of carbon black. These are clustered together in a loosely aggregated structure, leaving micron-scale voids. Some larger wall-like structures are also observed in some regions of the sample, but with extremely low occurrence (Figure 3.4). The diameter of the nanoparticles mainly varies between 50 to 100 nm for all four samples, although occasionally much larger micron-scale particles are also observed.

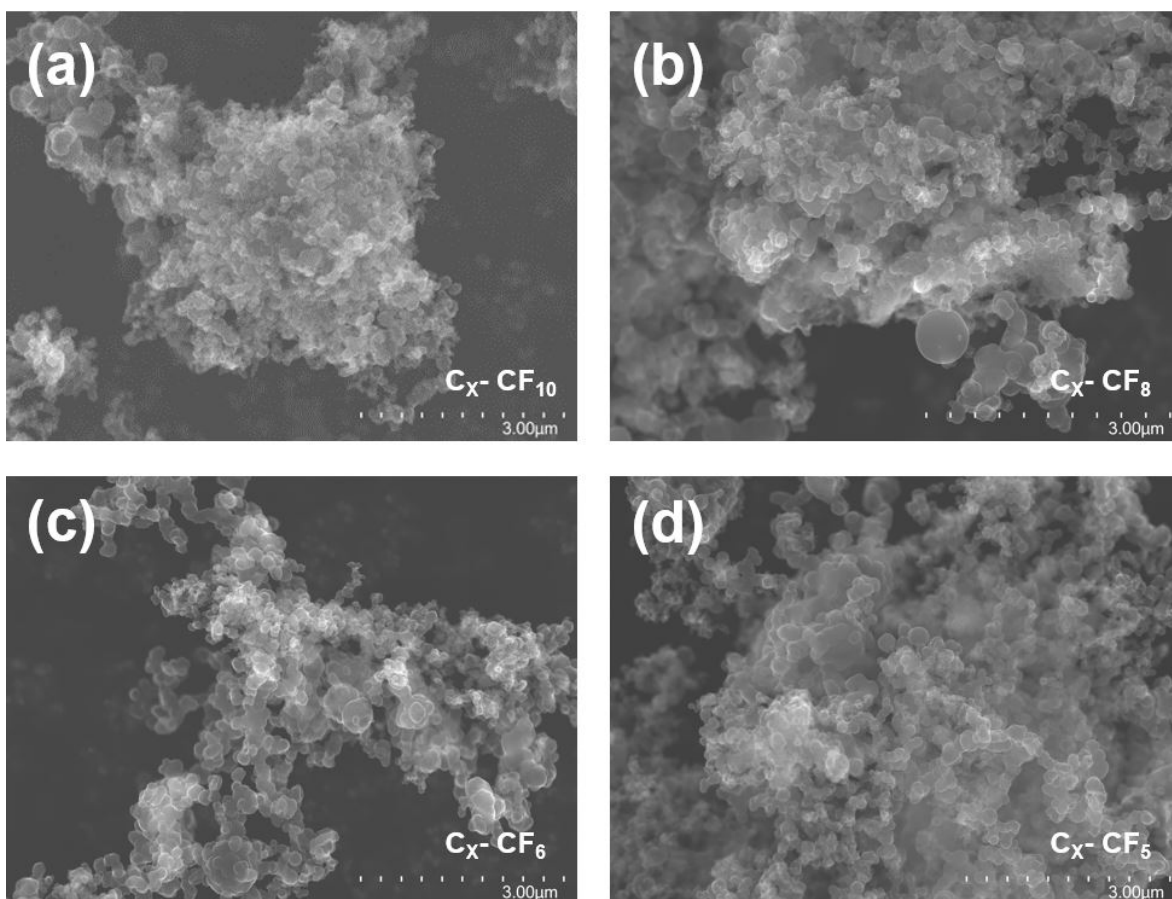


**Figure 3.3 SEM images of the four fluorinated carbons synthesized in this work: (a) CX-CF10; (b) CX-CF8; (c) CX-CF6; and (d) CX-CF5.**

The spherical structure of the nanoparticles strongly suggests that they are formed from liquid droplets, the shape being driven by surface tension. This would be analogous to the synthesis of carbon black, in which a liquid hydrocarbon precursor is injected into a high temperature reaction vessel as an atomized aerosol, after which it forms spheroidal carbon particles via incomplete combustion. In the case of these fluorinated carbons, we propose that the precursors enter a supersaturated mixed state within the PTFE vessel, forming suspended

droplets which then decompose to form the observed spheroidal nanoparticles. This is supported by the fact that the boiling point of tridecafluorooctan-1-ol is around 95 °C, which is very close to the temperature at which the reaction is observed to proceed.

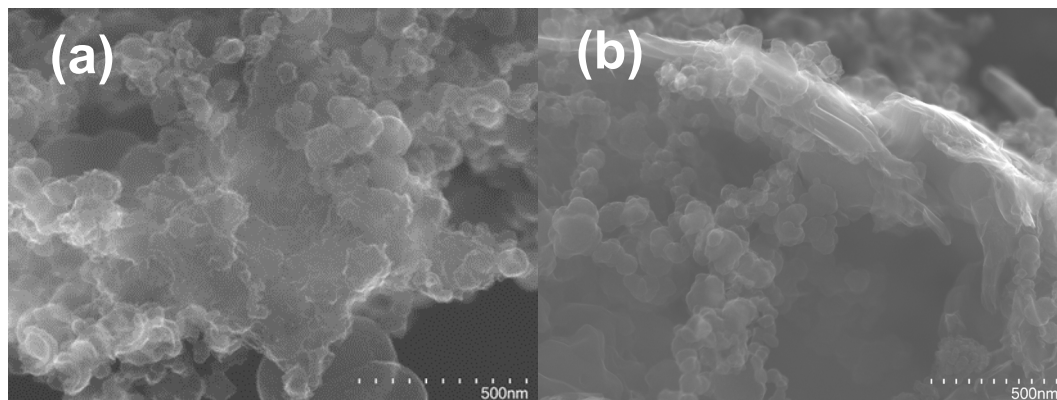


**Figure 3.4 SEM images of different structure in synthesized fluorinated alcohols.**

### **3.3.2 Surface Area and Porosity**

Nitrogen adsorption/desorption isotherms of all the fluorinated carbon samples were recorded to provide insight into the microstructure (Figure 3.5). Brunauer-Emmett-Teller (BET) and Barrett-Joyner-Halenda (BJH) methods were used to estimate the specific surface area and pore size distributions from the isotherms. The specific surface areas of  $\text{CF}_X\text{-C}_{10}$ ,  $\text{CF}_X\text{-C}_8$ ,  $\text{CF}_X\text{-C}_6$ , and  $\text{CF}_X\text{-C}_5$  were measured to be 25.6, 39.5, 25.7 and 26.6  $\text{m}^2/\text{g}$ , respectively, which are surprisingly low values for carbon nanomaterials. BJH and micropore plot (MP) analysis shows that these fluorinated carbons have relatively low mesopore volume and micropore volume, whilst the detected pore volume can probably be attributed to the

spaces between the particles observed by SEM, rather than being inherent to the nanoparticles themselves. All four samples display Type III isotherms, which are characteristic of non-porous materials [32].

Overall, the surface area and pore volumes are much lower compared to the non-fluorinated porous carbons prepared in a similar manner and previously reported by our group [33–36]. In those cases, the high surface area and porosity is attributed to the formation of sodium hydroxide (NaOH) during synthesis, which acts as an activation agent to generate micro- and mesopores. However, in the case of fluorinated carbon synthesis, this activation evidently does not occur. This could be attributed (i) to the high proportion of sodium fluoride (NaF) which is preferentially formed, decreasing the amount of NaOH activation agent present in the sample, or (ii) to the lower synthesis temperature in this case (activation is generally held to occur at  $> 500\text{ }^{\circ}\text{C}$ ). Meanwhile, (iii) differences in pressure within the PTFE crucible and the viscosity of the melting precursors as they decompose may also be a factor. Furthermore, (iv) fluorination has been previously reported to decrease surface area and pore volume by blocking micropores [23].

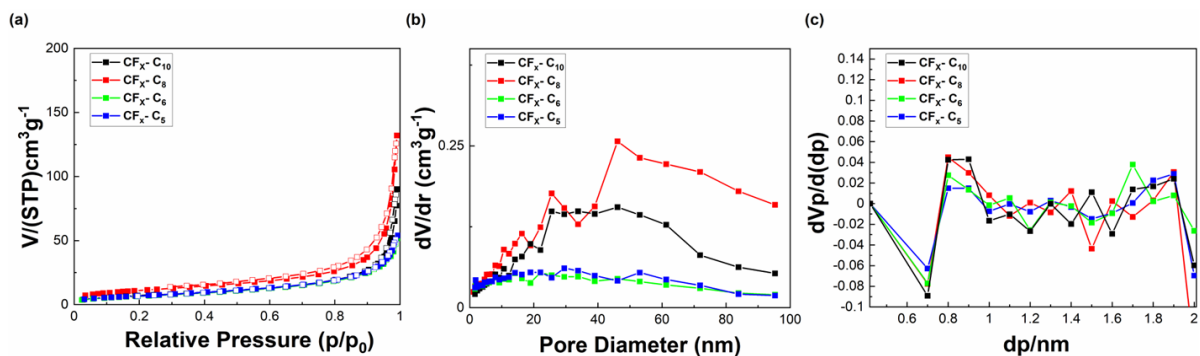


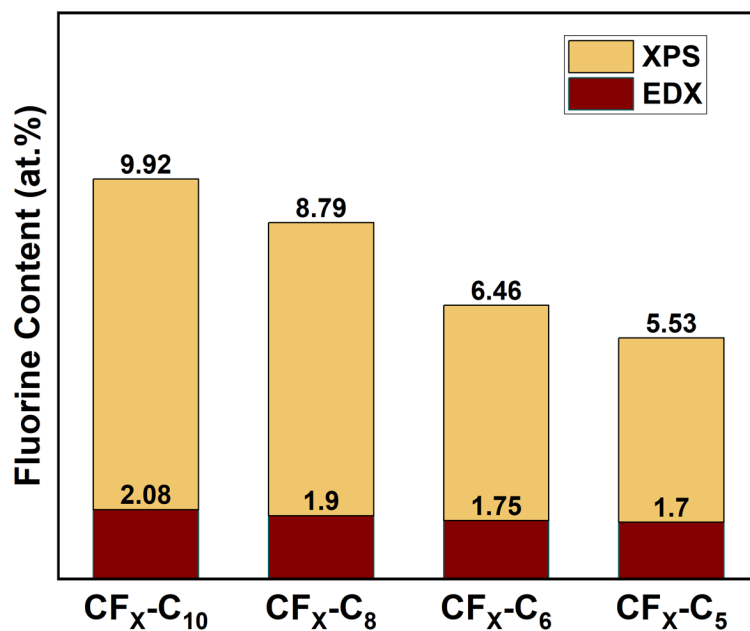
**Figure 3.5** Nitrogen gas adsorption results for the fluorinated carbons synthesized in this work: (a) BET isotherms, (b) BJH analysis, and (c) MP plots.

### 3.3.3 X-ray Photoelectron Spectroscopy (XPS)

The elemental compositions of the synthesized carbons as determined by XPS are shown in Table 3.2, and the corresponding fluorine contents are plotted in Figure 3.6. The results confirm that all the carbon samples contain a significant amount of fluorine. In addition, *the amount of fluorine detected in the samples correlates strongly with the proportion of fluorine in the fluorotelomer alcohol precursor*, ranging from 5.5 at.% for  $\text{CF}_x\text{-C}_5$  to 9.9 at.% for  $\text{CF}_x\text{-C}_{10}$ . Meanwhile, the oxygen content varies between 1.4 at.% and 2.1 at.% for all samples, and trace quantities of sodium are found, attributed to small amounts of remaining sodium fluoride. This NaF may be encapsulated within the samples, rendering it inaccessible during the washing step.

**Table 3.2 Elemental composition of synthesized fluorinated carbons measured by XPS.**

SAMPLE NAME	CARBON ( at%)	Fluorine (at%)	Oxygen (at%)	Sodium (at%)
CF <sub>x</sub> -C <sub>10</sub>	88.31	9.92	1.65	0.11
CF <sub>x</sub> -C <sub>8</sub>	89.46	8.79	1.60	0.15
CF <sub>x</sub> -C <sub>6</sub>	91.28	6.46	2.05	0.21
CF <sub>x</sub> -C <sub>5</sub>	93.03	5.53	1.40	0.04



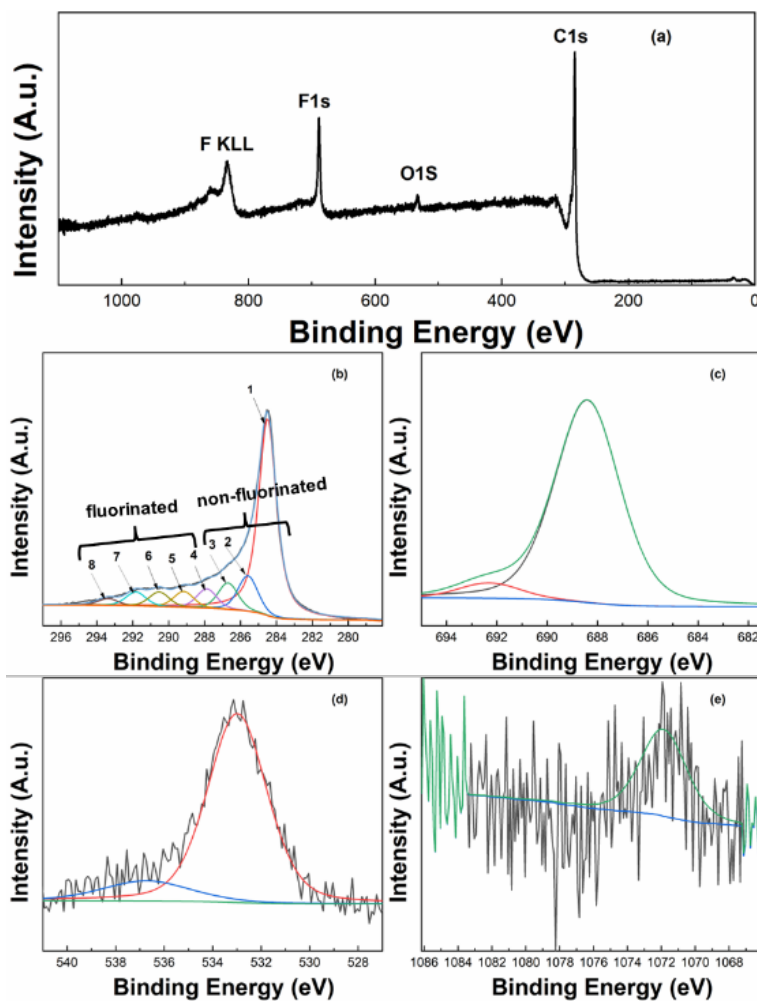
**Figure 3.6 Fluorine content as measured by XPS and EDX.**

Figure 3.7 shows the XPS survey and narrow scans for CF<sub>x</sub>-C<sub>10</sub>, whilst CF<sub>x</sub>-C<sub>8</sub>, CF<sub>x</sub>-C<sub>6</sub>, and CF<sub>x</sub>-C<sub>5</sub> are shown in Fig. 3.8, 3.9 and 3.10 respectively. Whilst the amount of fluorine varies depending on the type of fluorotelomer alcohol precursor, the narrow scan and deconvoluted

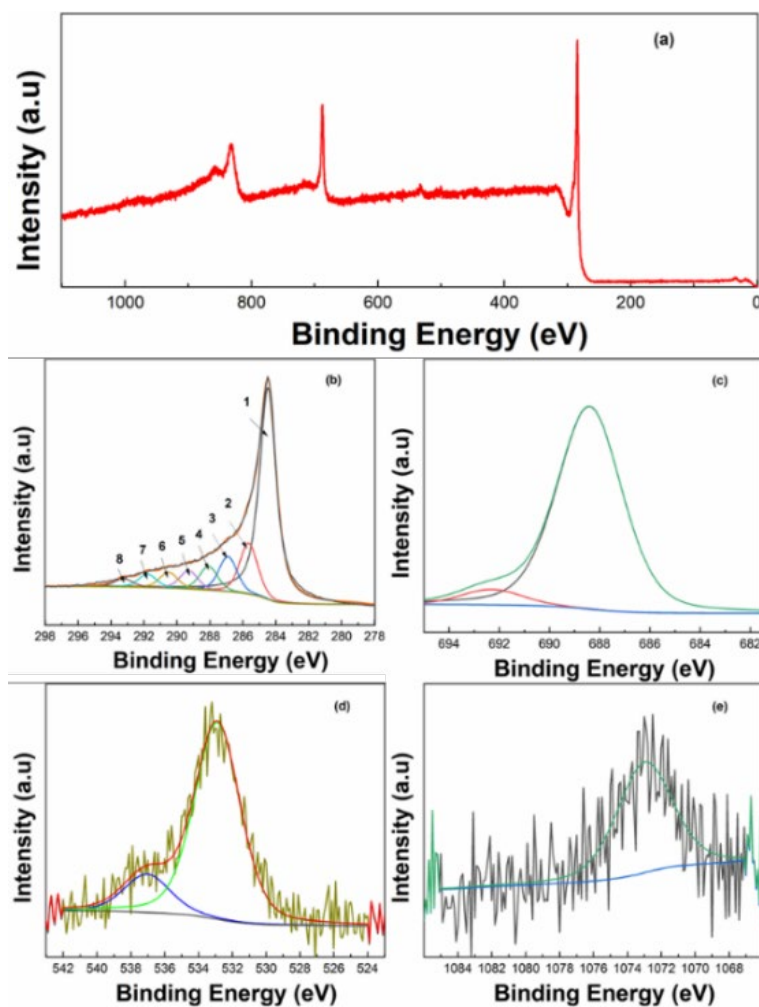
spectra have remarkably similar profiles. This confirms the reproducibility of this synthesis method even when different precursors are used. Previously, it has been reported that either ionic or covalent C-F bonds can be formed depending on the fluorination conditions, namely ionic bonds for low fluorine content, semi-ionic for mild fluorination, and covalent bonds for harsher fluorination conditions [1]. The binding energy of semi-ionic C-F bonds is generally assigned to around 287 eV in the C 1s region, and around 685.5 eV in the F 1s region [23]. For covalent C-F bonds, the binding energy is reported to depend on the amount of fluorine, varying between e.g. 289 eV for CF and 290.2 eV for CF<sub>2</sub> in the C 1s region, and around 688 eV in the F 1s region [37]. Furthermore, due to the high electronegativity of fluorine atoms, charging is expected to shift the spectra to slightly higher binding energy [9].

Figure 5(b) shows the C1s region deconvoluted into different contributions. Peaks at (1) 284.5 eV, (2) 285.6 eV, and (3) 286.7 eV are assigned to sp<sup>2</sup> bonding, sp<sup>3</sup> bonding and C-O bonds, respectively [10]. Meanwhile, the component at (4) 288 eV is attributed to C-F bonds at structural defects, and/or at the periphery of graphitic domains [37]. The component at (5) 289.1 eV is assigned to covalent C-F bonds at the alpha position in border CF<sub>2</sub> groups [37], and the component at (6) 290.2 eV is assigned to border CF<sub>2</sub> and CF groups surrounded by other CF groups [10]. Finally, the components at (7) 291.8 eV and (8) 293.5 eV are assigned to perfluorinated groups [9]. The F1s region (Fig. 5c) is deconvoluted into two peaks at 688.4 eV and 692.4 eV which are assigned to covalent C-F bonds. Finally, the O1s region in Fig. 5d has a broad signal centred at 533 eV, corresponding to C-O bonds. A small shoulder is observed at 536 eV corresponding to the sodium auger peak (Na KLL). No significant signals

are observed at lower binding energy in the F1s region (e.g. <686 eV), suggesting that fluorine atoms are covalently bonded to carbon rather than ionically bonded.



**Figure 3.7 XPS of CFX-C10: (a) survey spectrum; (b) C 1s region, (c) F 1s region; (d) O1s region; and the (e) Na 1s region.**



**Figure 3.8 XPS of CFX-C8: (a) survey spectrum; (b) C 1s region, (c) F 1s region; (d) O 1s region; and the (e) Na 1s region.**

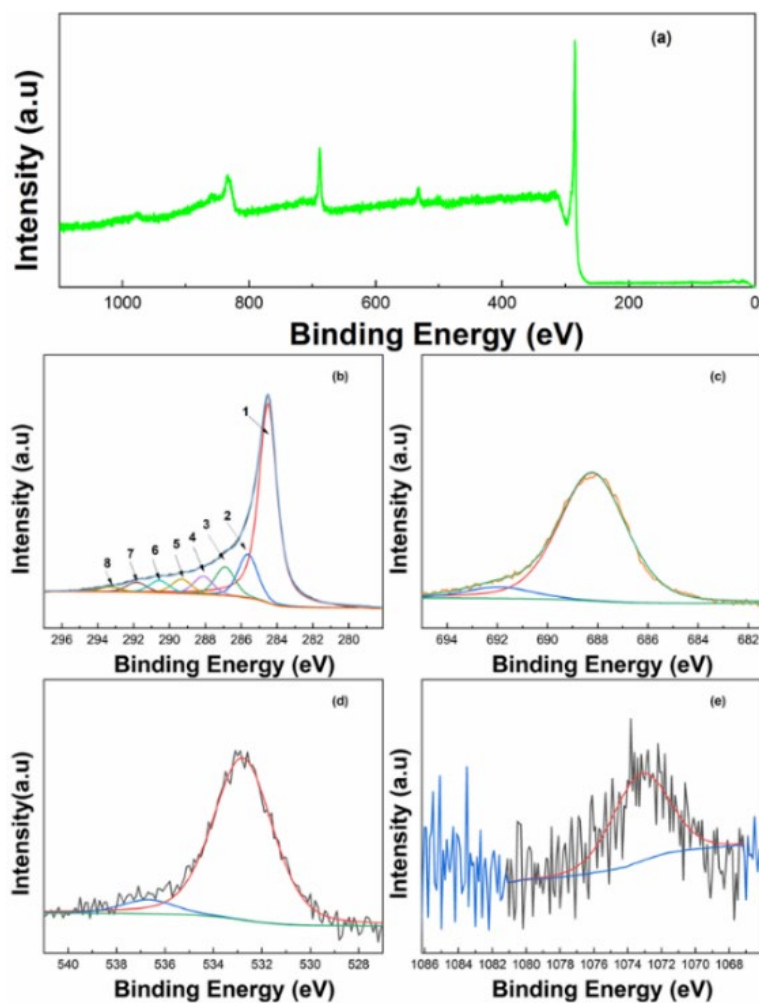


**Figure 3.9 XPS of CFX-C6: (a) survey spectrum; (b) C 1s region, (c) F 1s region; (d) O 1s region; and the (e) Na 1s region.**

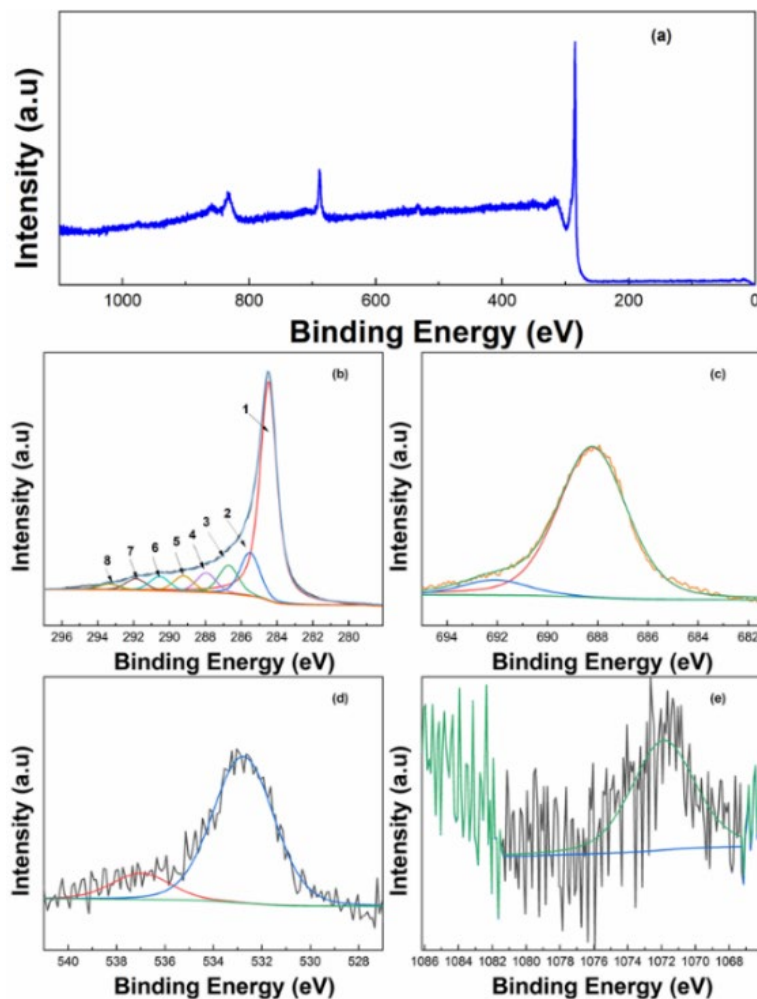


**Figure 3.10 XPS of CFX-C5: (a) survey spectrum; (b) C 1s region, (c) F 1s region; (d) O 1s region; and the (e) Na 1s region.**

### 3.3.4 Energy Dispersive X-Ray Analysis (EDX)

Table 3.3 shows the elemental composition of the samples as measured by EDX. In this case, the elemental composition of all the samples is similar. The carbon contents vary between 89 and 93 at.%, whilst the fluorine content remains between 1 and 2 at.% in all cases. The oxygen content varies from 5 to 9 at.%, and trace amounts of sodium are detected. Similar to

the case of XPS, EDX show that the fluorine content of the product is proportional to the amount of fluorine in the fluorotelomer alcohol precursor. However, the atomic concentration of fluorine (1 to 2 at.%) is much lower than that measured by XPS (i.e. 5 to 9 at.%). This discrepancy is attributed to the fact that XPS is a quasi-surface sensitive analysis technique with a penetration depth of just ~5 to 10 nm, whilst EDX is a bulk measurement technique with a much greater penetration depth of 1 to 2  $\mu\text{m}$ . Therefore, the difference in measured values suggests that fluorination mostly occurs near the surface of the carbon. As such, XPS detects a high fluorine content concentrated near the exposed surface of the carbon, whereas EDX records the average fluorine content throughout the whole sample, which includes the unfluorinated core of the particles.

**Table 3.3 Elemental composition of synthesized fluorinated carbons as measured by EDX.**

SAMPLE NAME	CARBON ( at%)	Fluorine (at%)	Oxygen (at%)	Sodium (at%)
CF <sub>x</sub> -C <sub>10</sub>	90.91	2.08	6.81	0.19
CF <sub>x</sub> -C <sub>8</sub>	93.0	1.90	5.02	0.18
CF <sub>x</sub> -C <sub>6</sub>	89.47	1.75	8.73	0.04
CF <sub>x</sub> -C <sub>5</sub>	89.06	1.70	9.06	0.19

Furthermore, the oxygen content of the samples is significantly higher according to EDX (i.e., 6 to 7 at%) compared to that measured using XPS (i.e. 1 to 2 at.%). Using the same reasoning, this might suggest that oxygen is not as highly concentrated at the surface. Conventional carbon nanomaterials can be relatively hydrophilic, and thus XPS tends to detect a high concentration of oxygen atoms due to adsorbed water molecules on the surface.

However, fluorinated carbon materials are generally hydrophobic, and thus water adsorption is not expected to be significant. The oxygen atoms detected here using EDX could be associated with e.g. residual sodium hydroxide encapsulated within the material and therefore protected from the washing step. Figure 11. shows representative EDX mapping of sample CF<sub>x</sub>-C<sub>6</sub>. The presence of fluorine is confirmed throughout the whole structure, indicating that the sample is uniform. Meanwhile, in some areas, fluorine and sodium signals have high intensity and overlapping EDX signals, strongly indicating the presence of sodium fluoride. It is likely that this sodium fluoride is encapsulated within the fluorinated carbon particles, preventing it from being removed during the washing step, as also observed in our previous studies [7,9].

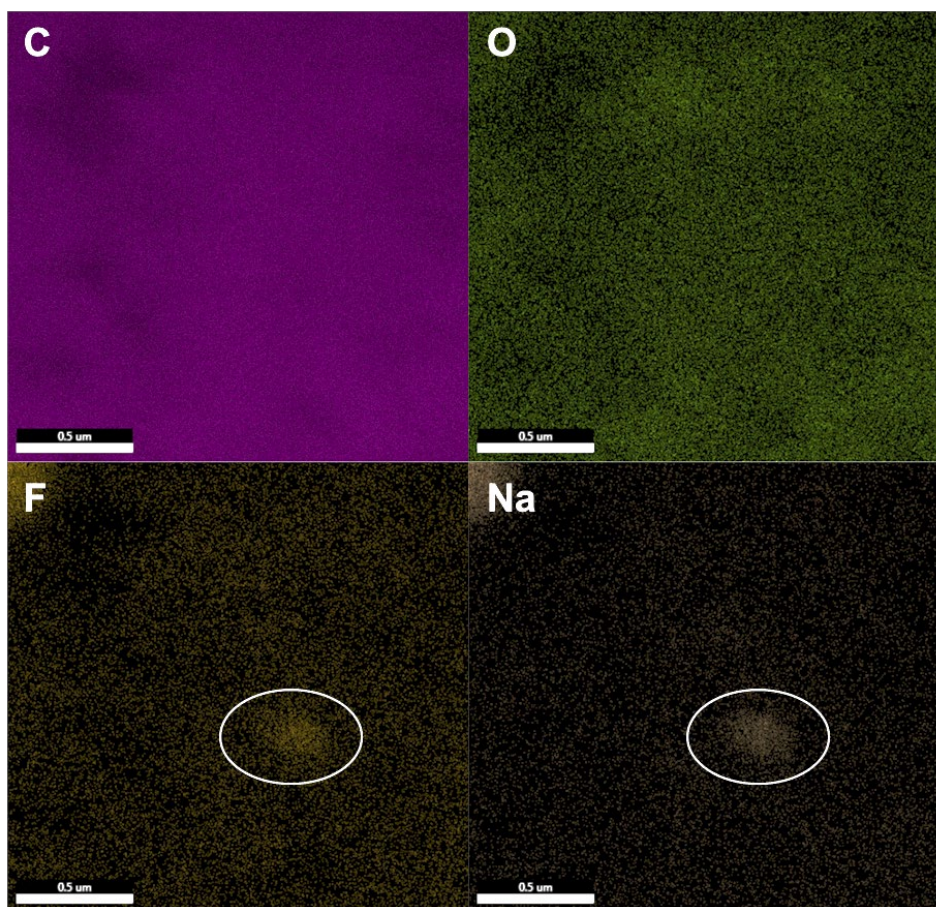


**Figure 3.11 EDX mapping of sample CFX-C6.**

### **3.3.5 X-ray Diffraction (XRD)**

The crystallographic structure of the synthesized fluorinated carbons was investigated using XRD (Figure 3.12). In all samples, similar peaks positions are observed, although there are some clear differences in the relative peak intensities. In some samples, a diffraction peak is observed at  $18^\circ$  (equivalent to a lattice spacing of 0.49 nm). This peak corresponds closely to crystalline PTFE [38]. As such, this may indicate contamination of the sample from the

PTFE reaction vessel, which may be expected due to the high reaction temperature (as observed in Figure 3.2). This peak has the highest intensity for sample CF<sub>x</sub>- C<sub>5</sub>.

Two narrow peaks are observed at 25.9 ° and 26.4 °, corresponding to lattice spacings of 0.342 and 0.337 nm, respectively. The later of these corresponds very closely with the lattice spacing of graphite (0.336 nm). As such, these features are attributed to the 002 planes of fluorinated carbon and graphitic carbon, respectively. Similarly, two separate peaks are observed at 42.8 ° and 44.5 °, corresponding to lattice spacings of 0.211 and 0.203 nm and attributed to the 100 planes of fluorinated carbon and graphitic carbon [6,24,25]. Previous studies have shown that the interlayer spacing of graphite increases due to fluorination, because of an increase in sp<sup>3</sup> type bonding [23,39–41]. In addition, two more carbon related diffraction peaks with much smaller intensity were observed at 54.5 ° and 77.5°, corresponding to lattice spacings of 0.168 and 0.123 nm, respectively. These are assigned to the 004 and 112 crystal planes of graphite. Finally, three small diffraction peaks are observed at 38.8, 56.0, and 70.3 °, which are attributed to the 200, 220, and 222 crystal planes of sodium fluoride [42].

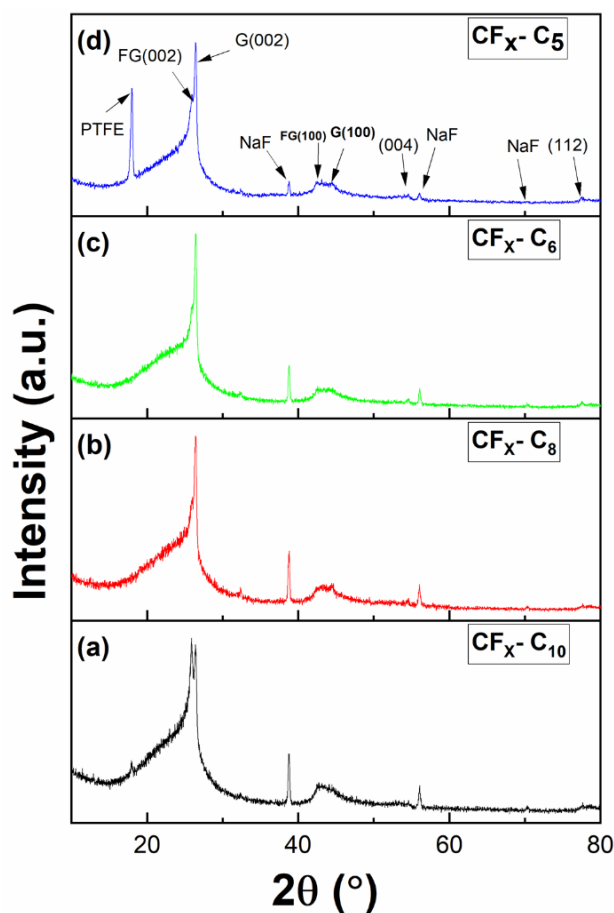


**Figure 3.12** XRD for the four fluorinated carbon samples: (a) CX-CF10; (b) CX-CF8; (c) CX-CF6; and (d) CX-CF5.

### 3.3.6 Raman Spectroscopy

Raman spectroscopy was used to further probe the chemical structure of the synthesized carbons (Figure 3.13), and the spectra are similar to those of graphitic materials commonly reported in the literature [43,44]. The most prominent features in the Raman spectra of graphitic materials are the G band at  $\sim 1582\text{ cm}^{-1}$  and the D band at  $\sim 1350\text{ cm}^{-1}$ , as well as the D' band at  $\sim 1620\text{ cm}^{-1}$  and the 2D or G' band at  $\sim 2700\text{ cm}^{-1}$ . The G band is associated

with the structural intensity of the  $sp^2$ -hybridized carbon atom. The D band is generally associated with defects graphitic ( $sp^2$ ) carbon, and it has been reported that the intensity of this peak can increase due to the  $sp^3$  bonding of fluorine in graphene [45].

In all the fluorinated carbon samples, the D band is centred at  $\sim 1342\text{ cm}^{-1}$  has a relatively high intensity, which is attributed directly to the fluorine content. The G peak is centred at 1580, 1578, 1579, and  $1571\text{ cm}^{-1}$  for  $CF_X-C_{10}$ ,  $CF_X-C_8$ ,  $CF_X-C_6$ , and  $CF_X-C_5$ , respectively. The shifting of the G peak is attributed to the different layer thicknesses of the graphitic structure and/or the fluorine doping [43]. Meanwhile, the ratio of the intensity of the D and G bands is commonly used to estimate the density of defects in the structure. In this case, the  $I_D/I_G$  values are 0.99, 0.99, 1.00, and 0.56 for  $CF_X-C_{10}$ ,  $CF_X-C_8$ ,  $CF_X-C_6$ , and  $CF_X-C_5$ , respectively. Furthermore, the 2D peak observed at  $\sim 2680\text{ cm}^{-1}$  has a profile similar to that of bulk graphite [44]. Between the D and G bands a relatively high signal intensity is observed for all samples, which is referred to as the D3 band in the literature. Previous studies suggest that this D3 band originates from the amorphous carbon fraction in the structure [46]. The D3 band signal intensity varies between samples. The lowest intensity recorded for sample  $CF_X-C_5$  which indicates the relatively smaller amount of amorphous region compared to other 3 samples.

The highest intensity of the diffraction peak at  $25.9^\circ$  (corresponding to fluorinated graphite) was obtained for sample  $CF_X-C_{10}$ . This is in agreement with the elemental analysis, which showed that this sample has the highest fluorine amount, of 9.9 at. %. Meanwhile, the diffraction peak at  $18^\circ$  (corresponding to PTFE) has the highest intensity for sample  $CF_X-C_5$ . This may indicate that this sample contains a higher degree of PTFE contamination. In

addition, this same sample had the lowest intensity D peak in the Raman spectra, indicating that this is the most graphitic of the samples, and it also had the lowest fluorine content (5.5 at.%). These factors combined strongly suggest that this sample reached a higher reaction temperature than the other three samples.

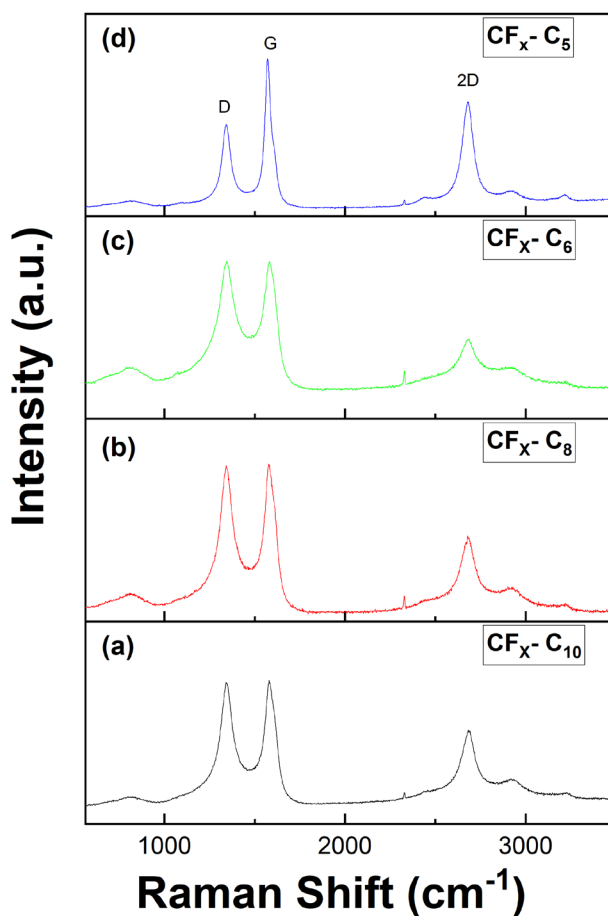


**Figure 3.13 Raman spectroscopy of the fluorinated carbon samples: (a) CX-CF10; (b) CX-CF8; (c) CX-CF6; and (d) CX-CF5.**

### 3.3.7 Transmission Electron Microscopy (TEM) and Selected Area Electron Diffraction (SAED)

The local crystal structure was examined in more detail using TEM and SAED. The TEM images (Figure 3.14) clearly reveal the presence of highly graphitized carbon with well-defined crystal structure, for all four of the samples. The graphitic structure appears to be more prominent near the outer surface of the particles, whilst the interior contains more amorphous regions. This mixture of different crystallographic phases may explain the combination of the highly developed 2D peak in the Raman spectra in combination with the large D peak. Meanwhile, the SAED results confirm the crystalline nature of the fluorinated carbon samples, with prominent diffraction rings corresponding to the 002, 101, 004, and 112 planes of graphitic carbon (Figure 3.15).

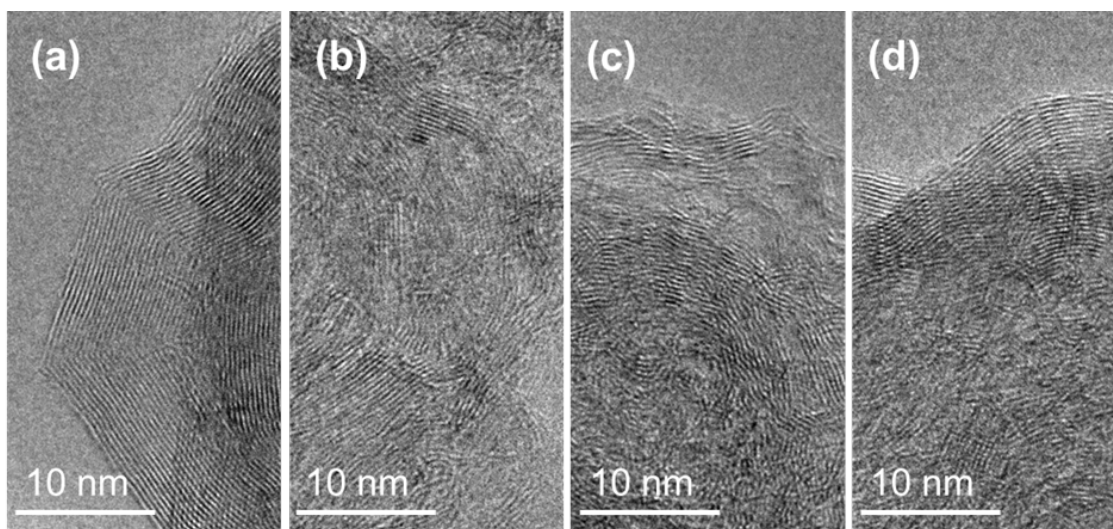


**Figure 3.14 TEM images of the fluorinated carbon samples: (a) CX-CF10; (b) CX-CF8; (c) CX-CF6; and (d) CX-CF5.**

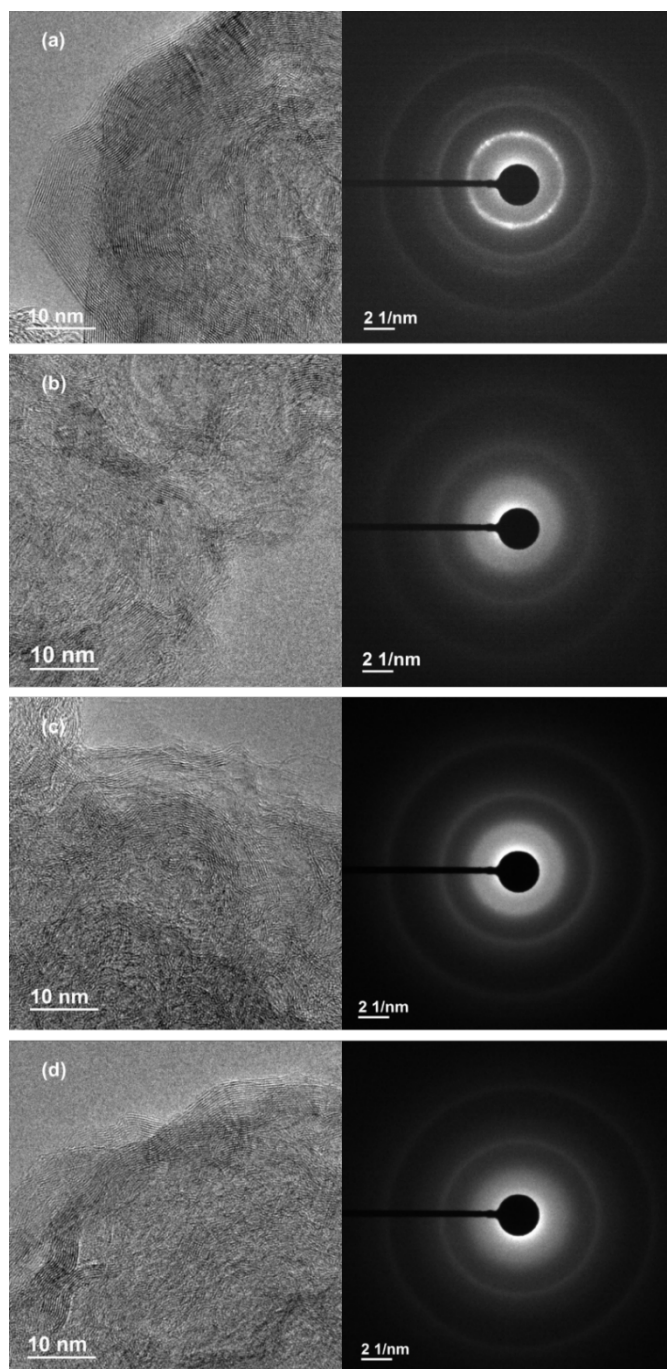


**Figure 3.15** TEM and SAED analysis results of the samples (a) CX-CF10, (b) CX-CF8, (c) CX-CF6, (d) CX-CF5.

### 3.3.8 New Catalytic Mechanism for Graphitic Structure

The XRD, Raman and TEM results all revealed that the fluorinated carbons synthesized in this work have a highly graphitic structure. This is despite the relatively low temperature used during the solvothermal reaction (namely, 150 °C). Even considering the exothermic nature of the reaction, the temperature inside the vessel only increased to ~350 °C. Under normal circumstances, the synthesis of highly graphitized carbon requires the application of very high temperatures. For example, graphitization of carbon is typically performed at temperatures of > 3000 °C [47]. Alternatively, carbon nanotubes are highly graphitic and are synthesized at intermediate temperature (e.g. 650 °C), but the graphitization in this case is assisted by the presence of a transition metal catalyst, usually in the form of iron, cobalt or nickel nanoparticles [48]. However, the solvothermal synthesis of fluorinated carbons from sodium and fluorotelomer alcohol precursors takes place in a PTFE vessel without exposure to conventional catalysts. In addition, the non-fluorinated carbons synthesized in our group using similar methods and identical equipment are not only highly amorphous, but remain so even at pyrolysis temperatures up to 1400 °C [49,50].

As such, the mechanism behind the highly graphitised nature of these fluorinated carbons is unclear. The recorded reaction temperature is much lower than that usually required for graphitisation, and there is no indication of the presence of transition metal catalyst particles such as iron or cobalt. Instead, we propose that HF molecules generated during the decomposition of the fluorotelomer alcohol have a catalytic effect, aiding in the formation of graphitic C-C bonds at high temperature and pressure. Indeed, HF-assisted alkylation is

commonly used in gasoline production, in which low-molecular-weight alkenes are converted into alkylate via carbon-carbon bond formation [51]. This is supported by the observation that the interior of the nanoparticles is more amorphous, whilst the outside is graphitic, which can be attributed to the outer surface of the particle being exposed to HF for longer periods of time, producing a greater degree of graphitization. This mechanism will be further investigated in future work.

### **3.3.9 Thermogravimetric Analysis (TGA), Differential Thermal Analysis (DTA), and Differential Thermogravimetry (DTG)**

The thermal stability of the synthesized fluorinated carbons was investigated using thermogravimetric analysis (TGA) and differential thermal analysis (DTA) in flowing air (Figure 3.16). Differential thermogravimetry (DTG) is shown in Figure 3.17. All four samples display similar profiles and are thermally stable up to ~500 °C. The first mass loss is attributed to the breaking of C-F bonds, manifesting as a slow decrease in the TGA curve and a small local minimum in the DTG at ~580 °C. When the temperature reaches ~600 °C, a rapid exothermic mass loss is observed representing reaction between carbon and oxygen in the air. The samples were completely consumed once the temperature reached ~700 °C in all cases.

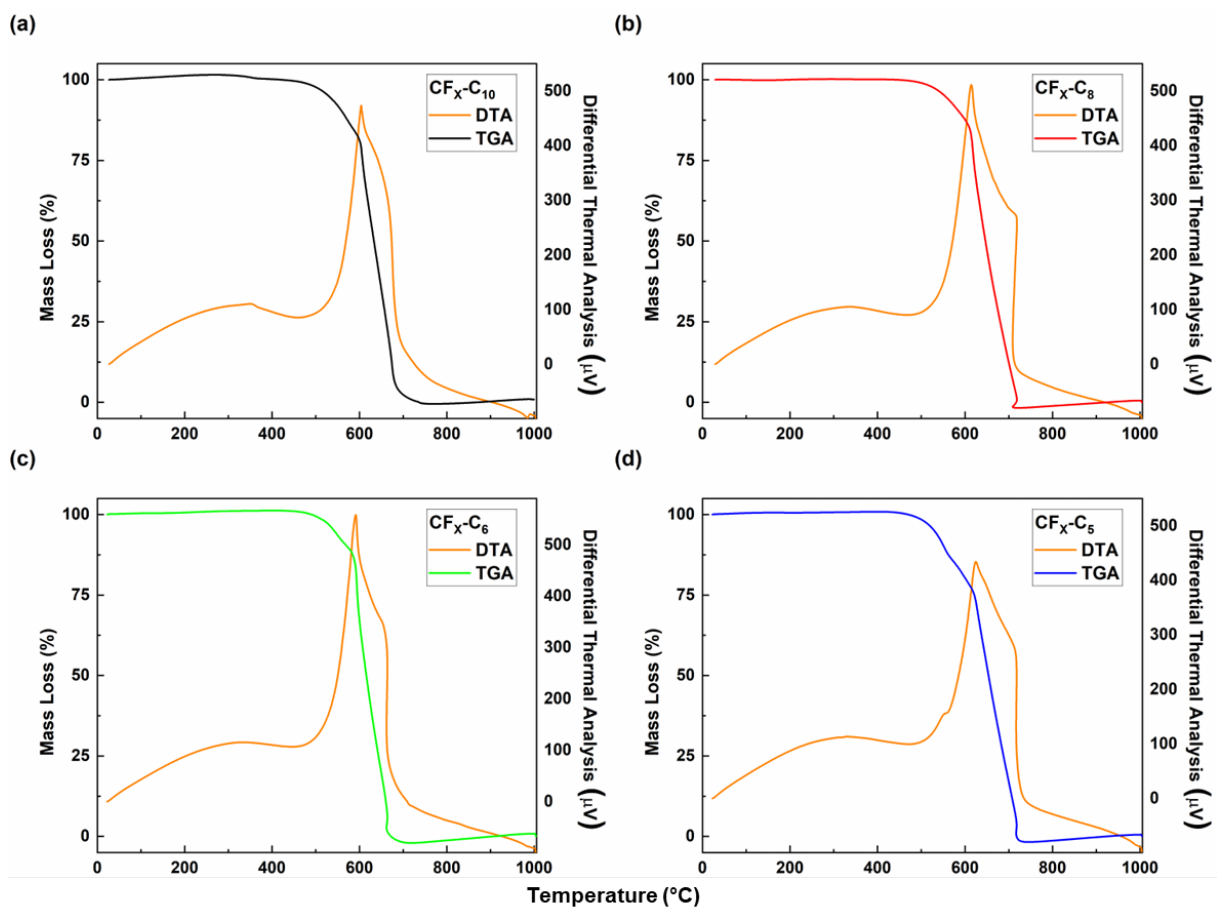


**Figure 3.16 Thermogravimetric analysis (TGA) and differential thermal analysis (DTA) of the synthesized fluorinated carbons: (a) CX-CF10; (b) CX-CF8; (c) CX-CF6; (d) CX-CF5.**

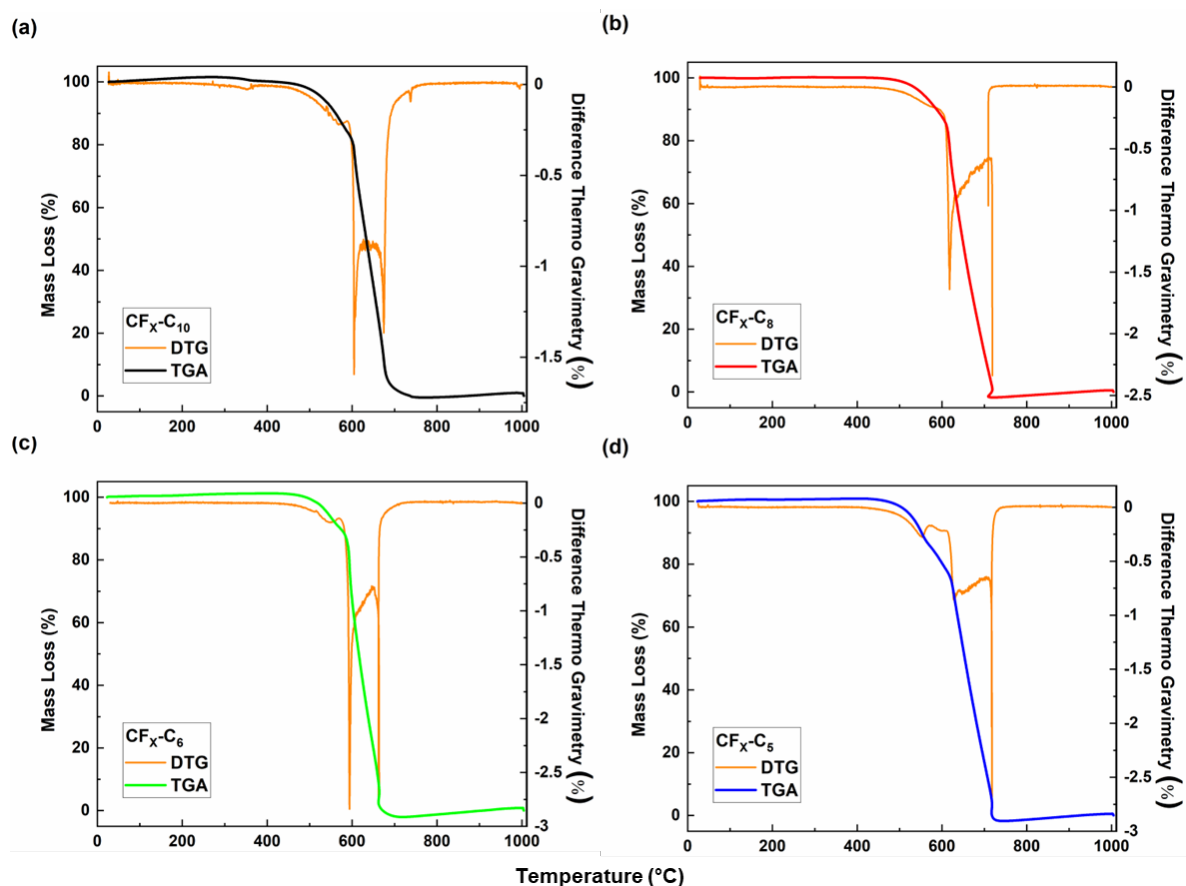


**Figure 3.17 Thermogravimetric analysis and difference thermogravimetric analysis of samples (a) CF<sub>x</sub>-C<sub>10</sub>, (b) CF<sub>x</sub>-C<sub>8</sub>, (c) CF<sub>x</sub>-C<sub>6</sub>, (d) CF<sub>x</sub>-C<sub>5</sub>.**

### 3.3.10 Water Contact Angle (WCA) Measurement

Due to the low free energy of hydration and in combination with the large diameter of fluorine atoms (leading to low surface density and poorer van der Waals interactions with water [52]), fluorinated carbons are generally hydrophobic. This is also the case with the fluorinated carbons synthesised in this work. This is the reason for washing with an ethanol: water mixture, because pure water will not interact with the resulting carbon materials at all. The

relative hydrophobicity of the carbons synthesised in this work was evaluated using the water contact angle (WCA) as a comparison (Figure 3.18). The WCAs of  $C_X-CF_{10}$ ,  $C_X-CF_8$ ,  $C_X-CF_6$ , and  $C_X-CF_5$  are 160.0 °, 158.5 °, 154.6 °, and 151.0 °, respectively. These results confirm that all of the synthesised samples display superhydrophobicity (i.e.  $WCA > 150^\circ$ ). Furthermore, there is a clear trend in which higher fluorine content results in higher water contact angle. Importantly, this result shows that it is possible to tailor the water contact angle of these fluorinated carbons by varying the type of fluorotelomer alcohol precursor, which could be important in e. g. electrochemical applications.

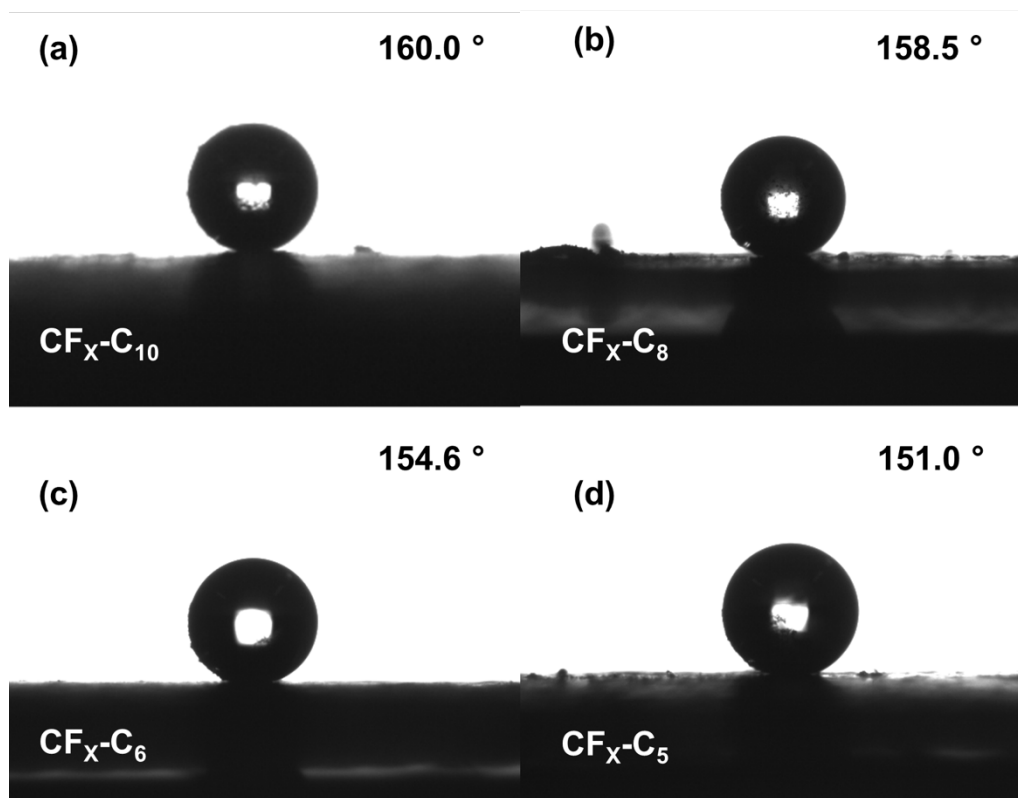


**Figure 3.18** Water contact angle (WCA) measurements for: (a)  $C_X-CF_{10}$ ; (b)  $C_X-CF_8$ ; (c)  $C_X-CF_6$ ; (d)  $C_X-CF_5$ .

### 3.3.11 Secondary Heat Treatment and Removal of Fluorine

It has been previously reported that fluorine atoms can be removed from fluorinated graphene via thermal annealing [27,40]. To explore the effect of thermal treatment on these fluorinated carbons  $\text{CF}_x\text{-C}_8$  was selected for a secondary heat treatment in a tube furnace at 700 °C (5 °C/min heating rate) under flowing nitrogen (100 ml/min), for one hour. The resulting sample is labelled  $\text{CF}_x\text{-C}_8\text{-HT}$ .

XPS analysis reveals that after secondary thermal treatment,  $\text{CF}_x\text{-C}_8\text{-HT}$  comprises 97.01 at.% carbon, 2.67 at.% oxygen, 0.16 at.% sodium and just 0.16 at.% fluorine (Figure 3.19). This confirms that most fluorine atoms can be removed from the synthesized fluorinated carbons via thermal annealing. Since the concentration of sodium and fluorine are similar, the remaining fluorine atoms are likely in the form of encapsulated sodium fluoride, which is thermally stable with a melting point of 993 °C. The oxygen content of  $\text{CF}_x\text{-C}_8\text{-HT}$  is slightly increased compared to  $\text{CF}_x\text{-C}_8$  (Table 3.1), which is attributed to an increased proportion of absorbed water vapor after heat treatment, due to loss of the hydrophobicity. The C1s region of  $\text{CF}_x\text{-C}_8\text{-HT}$  is deconvoluted into 5 main peaks, corresponding to (1)  $\text{sp}^2$  carbon at 284.5 eV; (2) aliphatic  $\text{sp}^3$  carbon at 285.6 eV; (3) C-O bonds at 286.7 eV; (4) O-C=O bonds at 288.5 eV; and (5) C1s shake-up. The small F1s peak at 687.5 eV and the Na1s peak at 1072 eV correspond to NaF.

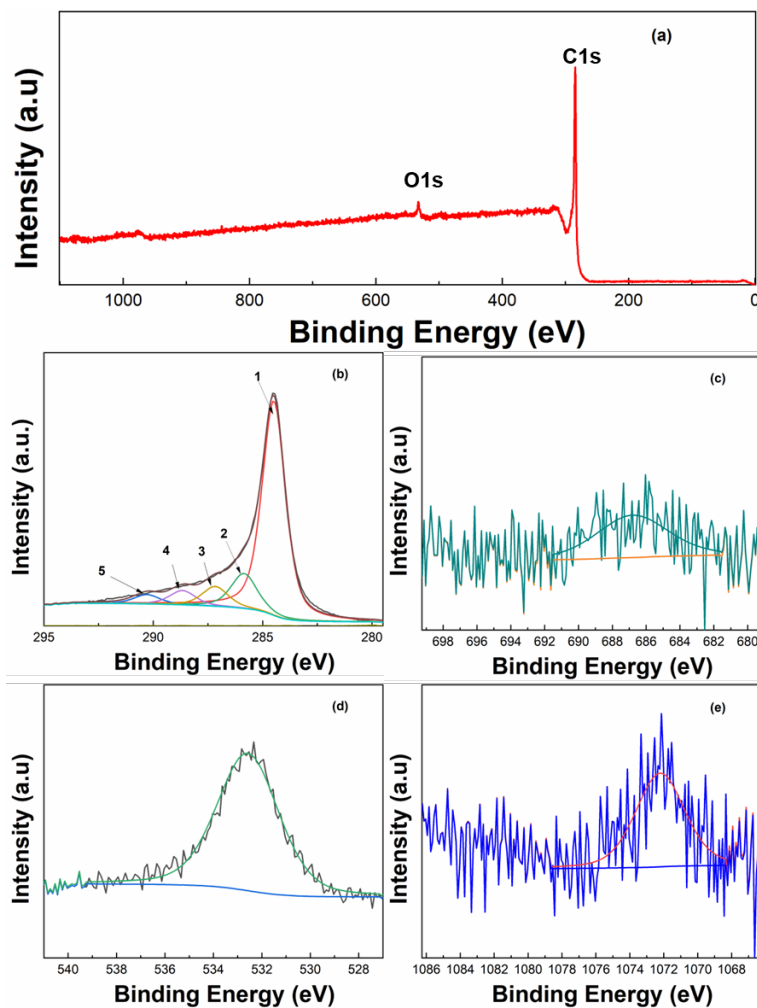


**Figure 3.19 XPS of CFX-C8-HT: (a) survey spectrum; (b) C 1s region; (c) F 1s region; (d) O1s region; and (e) Na 1s region.**

To further clarify the effect of secondary thermal annealing, CFX-C<sub>8</sub>-HT was analysed by XRD (Figure 20b). The diffraction peaks at 25.9, 42.8, 54.5 and 77.5 ° are assigned to the 002, 100, 004 and 112 crystal planes of graphite, respectively. Surprisingly, despite the removal of fluorine atoms during secondary thermal annealing, the wider d-spacing associated with fluorinated graphite is retained (namely at 0.342 nm), whilst the narrower d-spacing associated with graphite is less prominent. This is contrary to reports in previous

studies, in which the d-spacing of graphitic fluorinated carbons contracts upon the removal of fluorine atoms, reverting back to its graphitic form [40,53,54]. This effect may be related to the microstructure and chemical structure of the carbon under investigation. Similar to the case of non-graphitizable carbons [55], crosslinking of basic structural units in the structure, and/or interatomic corrugation, [28] may prevent contraction of the graphitic layers in this case, despite the removal of fluorine. Meanwhile, peaks at 38.8, 56.0, and 70.3 ° are assigned to different orientations of crystalline NaF. The relative intensity of the peaks assigned to NaF increases significantly after the secondary thermal treatment. This increase in intensity is attributed to the fact that NaF has a melting point of 993 °C, and is therefore unaffected by secondary thermal treatment at 700 °C.

Raman spectra before and after secondary heat treatment are shown in Figure 20 (c-d). After thermal annealing, the intensity of the D peak decreases dramatically, as also reflected by a significant decrease in the  $I_D/I_G$  ratio from 0.99 for  $CF_X-C_8$  to 0.51 for  $CF_X-C_8-HT$ . In addition,  $I_{2D}/I_G$  ratio was 0.51 for  $CF_X-C_8$ , increasing to 0.73 for  $CF_X-C_8-HT$ . These changes are directly attributed to the removal of  $sp^3$  bonded fluorine atoms which disrupt the  $sp^2$  structure of graphitic carbon [27,56]. Overall, these results suggest that the secondary thermal treatment of these fluorinated carbons successfully removes C-F bonds, whilst creating a highly graphitic carbon with large d-spacing.

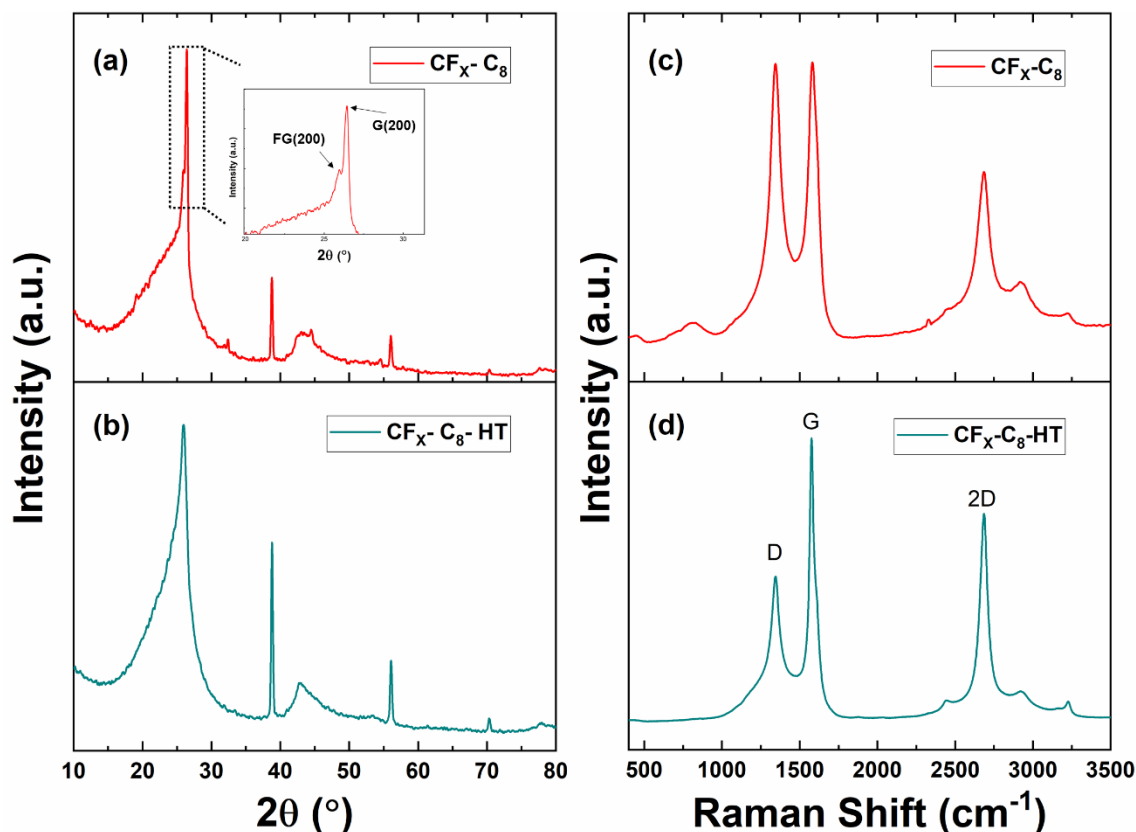


**Figure 3.20 (a-b) XRD and (c-d) Raman spectra of  $\text{CF}_x\text{-C}_8$  and  $\text{CF}_x\text{-C}_8\text{-HT}$ .**

Finally, attempts were made to measure the WCA of the  $\text{C}_x\text{-CF}_8\text{-HT}$  sample after secondary heat treatment. However, for this sample droplet formation was not possible, and the liquid rapidly wetted the surface. As such, the sample is confirmed to be hydrophilic after thermal annealing. Since the microstructure is similar after secondary heat treatment, this confirms that the hydrophobic nature of the synthesised carbons can also be controlled via thermal annealing. This presents a second method of tailoring the hydrophobicity of these fluorinated carbons.

### 3.4 Summary and Conclusion

In this chapter a simple method to synthesize hydrophobic fluorinated carbons with controllable fluorine content was described. Four different fluorotelomer alcohols with different chain length were used as precursors and these were reacted with sodium metal at 150 °C. The reaction was exothermic and the temperature inside the reaction vessel subsequently reached 345 °C. The resulting fluorinated carbon nanoparticle had a non-porous microstructure and low surface area, with a predominantly covalent C-F bonds. The samples were all found to have highly crystalline graphitic components, despite the low reaction temperature, attributed to the catalytic effect of HF generated during the reaction. Meanwhile, the fluorine content of the final products was found to be dependent on the chain length of the fluorotelomer alcohol precursor. The carbons were all found to be superhydrophobic, and the water contact angle was dependant on the fluorine content. Furthermore, secondary thermal treatment was used to effectively remove fluorine atoms from the samples, providing a second method of tailoring the fluorine content and water contact angle.

### 3.5 References

- [1] O.R. Brown, Graphite Fluorides, 1989. [https://doi.org/10.1016/0013-4686\(89\)87102-6](https://doi.org/10.1016/0013-4686(89)87102-6).
- [2] R.L. Fusaro, Mechanisms of graphite fluoride [(CF<sub>x</sub>)<sub>n</sub>] lubrication, *Wear*. 53 (1979) 303–323. [https://doi.org/10.1016/0043-1648\(79\)90084-X](https://doi.org/10.1016/0043-1648(79)90084-X).
- [3] T. Nakajima, V. Gupta, Y. Ohzawa, M. Koh, R.N. Singh, A. Tressaud, E. Durand, Electrochemical behavior of plasma-fluorinated graphite for lithium ion batteries, *J. Power Sources*. 104 (2002) 108–114. [https://doi.org/10.1016/S0378-7753\(01\)00895-3](https://doi.org/10.1016/S0378-7753(01)00895-3).
- [4] J. Li, K. Naga, Y. Ohzawa, T. Nakajima, H. Iwata, Surface fluorination and electrochemical behavior of petroleum cokes graphitized at medium and high temperatures for secondary lithium battery, *J. Fluor. Chem.* 126 (2005) 1028–1035. <https://doi.org/10.1016/j.jfluchem.2005.03.016>.
- [5] K. Guérin, M. Dubois, A. Houdayer, A. Hamwi, Applicative performances of fluorinated carbons through fluorination routes: A review, *J. Fluor. Chem.* 134 (2012) 11–17. <https://doi.org/10.1016/j.jfluchem.2011.06.013>.
- [6] W. Kang, S. Li, Preparation of fluorinated graphene to study its gas sensitivity, *RSC Adv.* 8 (2018) 23459–23467. <https://doi.org/10.1039/C8RA03451F>.
- [7] E.M. Can, A. Mufundirwa, P. Wang, S. Iwasaki, T. Kitahara, H. Nakajima, M. Nishihara, K. Sasaki, S.M. Lyth, Superhydrophobic fluorinated carbon powders for

- improved water management in hydrogen fuel cells, *J. Power Sources*. 548 (2022) 232098. <https://doi.org/10.1016/j.jpowsour.2022.232098>.
- [8] J. Guo, J. Zhang, H. Zhao, Y. Fang, K. Ming, H. Huang, J. Chen, X. Wang, Fluorine-doped graphene with an outstanding electrocatalytic performance for efficient oxygen reduction reaction in alkaline solution, *R. Soc. Open Sci.* 5 (2018). <https://doi.org/10.1098/rsos.180925>.
- [9] S.M. Lyth, W. Ma, J. Liu, T. Daio, K. Sasaki, A. Takahara, B. Ameduri, Solvothermal synthesis of superhydrophobic hollow carbon nanoparticles from a fluorinated alcohol, *Nanoscale*. 7 (2015) 16087–16093. <https://doi.org/10.1039/c5nr03484a>.
- [10] G. Nansé, E. Papirer, P. Fioux, F. Moguet, A. Tressaud, Fluorination of carbon blacks: An X-ray photoelectron spectroscopy study: I. A literature review of XPS studies of fluorinated carbons. XPS investigation of some reference compounds, *Carbon N. Y.* 35 (1997) 175–194. [https://doi.org/10.1016/S0008-6223\(96\)00095-4](https://doi.org/10.1016/S0008-6223(96)00095-4).
- [11] J. Parmentier, S. Schlienger, M. Dubois, E. Disa, F. Masin, T.A. Centeno, Structural/textural properties and water reactivity of fluorinated activated carbons, *Carbon N. Y.* 50 (2012) 5135–5147. <https://doi.org/10.1016/j.carbon.2012.06.054>.
- [12] S.J. Park, M.K. Seo, Y.S. Lee, Surface characteristics of fluorine-modified PAN-based carbon fibers, *Carbon N. Y.* 41 (2003) 723–730. [https://doi.org/10.1016/S0008-6223\(02\)00384-6](https://doi.org/10.1016/S0008-6223(02)00384-6).
- [13] C. Te Hsieh, W.Y. Chen, F.L. Wu, Fabrication and superhydrophobicity of fluorinated carbon fabrics with micro/nanoscaled two-tier roughness, *Carbon N. Y.* 46 (2008)

1218–1224. <https://doi.org/10.1016/j.carbon.2008.04.026>.

- [14] N.O.V. Plank, L. Jiang, R. Cheung, Fluorination of carbon nanotubes in CF<sub>4</sub> plasma, *Appl. Phys. Lett.* 83 (2003) 2426–2428. <https://doi.org/10.1063/1.1611621>.
- [15] C.B.H. Mickelson, E. T., Fluorination of single-wall carbon nanotubes, *Chem. Phys. Lett.* 296 (1998) 188–194. [https://doi.org/10.1016/S0008-6223\(97\)00013-4](https://doi.org/10.1016/S0008-6223(97)00013-4).
- [16] B. Shen, J. Chen, X. Yan, Q. Xue, Synthesis of fluorine-doped multi-layered graphene sheets by arc-discharge, *RSC Adv.* 2 (2012) 6761–6764. <https://doi.org/10.1039/c2ra20593a>.
- [17] Y. Ahmad, N. Batisse, X. Chen, M. Dubois, Preparation and Applications of Fluorinated Graphenes, *C.* 7 (2021) 20. <https://doi.org/10.3390/c7010020>.
- [18] X. Wang, Y. Dai, J. Gao, J. Huang, B. Li, C. Fan, J. Yang, X. Liu, High-yield production of highly fluorinated graphene by direct heating fluorination of graphene-oxide, *ACS Appl. Mater. Interfaces.* 5 (2013) 8294–8299. <https://doi.org/10.1021/am402958p>.
- [19] W. Zhang, P. Bonnet, M. Dubois, C.P. Ewels, K. Guérin, E. Petit, J.Y. Mevellec, L. Vidal, D.A. Ivanov, A. Hamwi, Comparative study of SWCNT fluorination by atomic and molecular fluorine, *Chem. Mater.* 24 (2012) 1744–1751. <https://doi.org/10.1021/cm203415e>.
- [20] E. Rangasamy, J. Li, G. Sahu, N. Dudney, C. Liang, Pushing the Theoretical Limit of Li-CF, *J. Am. ....* (2014). <http://pubs.acs.org/doi/abs/10.1021/ja5026358>.

- [21] R. Stine, W.K. Lee, K.E. Whitener, J.T. Robinson, P.E. Sheehan, Chemical stability of graphene fluoride produced by exposure to XeF<sub>2</sub>, *Nano Lett.* 13 (2013) 4311–4316. <https://doi.org/10.1021/nl4021039>.
- [22] Y.S. Lee, Syntheses and properties of fluorinated carbon materials, *J. Fluor. Chem.* 128 (2007) 392–403. <https://doi.org/10.1016/j.jfluchem.2006.11.014>.
- [23] O. V. Boltalina, T. Nakajima, *New Fluorinated Carbons: Fundamentals and Applications Progress in Fluorine Science Series*, 2016. <https://doi.org/10.1016/C2014-0-04885-X>.
- [24] S. Ha, C. Lim, Y.S. Lee, Fluorination methods and the properties of fluorinated carbon materials for use as lithium primary battery cathode materials, *J. Ind. Eng. Chem.* 111 (2022) 1–17. <https://doi.org/10.1016/j.jiec.2022.03.044>.
- [25] Y. Ahmad, E. Disa, K. Guérin, M. Dubois, E. Petit, A. Hamwi, P. Thomas, J.L. Mansot, Structure control at the nanoscale in fluorinated graphitized carbon blacks through the fluorination route, *J. Fluor. Chem.* 168 (2014) 163–172. <https://doi.org/10.1016/j.jfluchem.2014.09.021>.
- [26] H. Touhara, Property Control of Carbon Materials by Fluorination, *Carbon Alloy. Nov. Concepts to Dev. Carbon Sci. Technol.* 38 (2003) 485–498. <https://doi.org/10.1016/B978-008044163-4/50030-9>.
- [27] S.D. Costa, J.E. Weis, O. Frank, Z. Bastl, M. Kalbac, Thermal treatment of fluorinated graphene: An in situ Raman spectroscopy study, *Carbon N. Y.* 84 (2015) 347–354. <https://doi.org/10.1016/j.carbon.2014.12.029>.

- [28] Fluorographene: A Two-Dimensional Counterpart of Teflon - Nair - 2010 - Small - Wiley Online Library, (n.d.).  
<https://onlinelibrary.wiley.com/doi/epdf/10.1002/sml.201001555>.
- [29] W. Zhang, L. Spinelle, M. Dubois, K. Guérin, H. Kharbache, F. Masin, A.P. Kharitonov, A. Hamwi, J. Brunet, C. Varenne, A. Pauly, P. Thomas, D. Himmel, J.L. Mansot, New synthesis methods for fluorinated carbon nanofibres and applications, *J. Fluor. Chem.* 131 (2010) 676–683. <https://doi.org/10.1016/j.jfluchem.2010.02.007>.
- [30] R.C. Buck, J. Franklin, U. Berger, J.M. Conder, I.T. Cousins, P. De Voogt, A.A. Jensen, K. Kannan, S.A. Mabury, S.P.J. van Leeuwen, Perfluoroalkyl and polyfluoroalkyl substances in the environment: Terminology, classification, and origins, *Integr. Environ. Assess. Manag.* 7 (2011) 513–541.  
<https://doi.org/10.1002/ieam.258>.
- [31] H.-J. Lehmler, Synthesis of environmentally relevant fluorinated surfactants—a review, *Chemosphere.* 58 (2005) 1471–1496.  
<https://doi.org/10.1016/j.chemosphere.2004.11.078>.
- [32] M. Thommes, K. Kaneko, A. V. Neimark, J.P. Olivier, F. Rodriguez-Reinoso, J. Rouquerol, K.S.W. Sing, Physisorption of gases, with special reference to the evaluation of surface area and pore size distribution (IUPAC Technical Report), *Pure Appl. Chem.* 87 (2015) 1051–1069. <https://doi.org/10.1515/pac-2014-1117>.
- [33] M.I.M. Kusdhany, Z. Ma, A. Mufundirwa, H.W. Li, K. Sasaki, A. Hayashi, S.M. Lyth, Hydrogen and carbon dioxide uptake on scalable and inexpensive microporous carbon

- foams, *Microporous Mesoporous Mater.* 343 (2022) 112141. <https://doi.org/10.1016/j.micromeso.2022.112141>.
- [34] A. Mufundirwa, G.F. Harrington, M.S. Ismail, B. Šmid, B. V. Cunning, Y. Shundo, M. Pourkashanian, K. Sasaki, A. Hayashi, S.M. Lyth, Gram-scale synthesis of alkoxide-derived nitrogen-doped carbon foam as a support for Fe-N-C electrocatalysts, *Nanotechnology*. 31 (2020). <https://doi.org/10.1088/1361-6528/ab76ed>.
- [35] S.M. Lyth, H. Shao, J. Liu, K. Sasaki, E. Akiba, Hydrogen adsorption on graphene foam synthesized by combustion of sodium ethoxide, *Int. J. Hydrogen Energy*. 39 (2014) 376–380. <https://doi.org/10.1016/j.ijhydene.2013.10.044>.
- [36] S.M. Lyth, Y. Nabae, N.M. Islam, T. Hayakawa, S. Kuroki, M.A. Kakimoto, S. Miyata, Solvothermal synthesis of nitrogen-containing graphene for electrochemical oxygen reduction in acid media, *E-Journal Surf. Sci. Nanotechnol.* 10 (2012) 29–32. <https://doi.org/10.1380/ejssnt.2012.29>.
- [37] A. Tressaud, F. Moguet, S. Flandrois, M. Chambon, C. Guimon, G. Nanse, E. Papirer, V. Gupta, O.P. Bahl, On the nature of C-F bonds in various fluorinated carbon materials: XPS and TEM investigations, *J. Phys. Chem. Solids*. 57 (1996) 745–751. [https://doi.org/10.1016/0022-3697\(96\)00343-5](https://doi.org/10.1016/0022-3697(96)00343-5).
- [38] J. Si, R. Ma, Y. Wu, Y. Dong, K. Yao, Microstructure and magnetic properties of novel powder cores composed of iron-based amorphous alloy and PTFE, *J. Mater. Sci.* 57 (2022) 8154–8166. <https://doi.org/10.1007/s10853-022-07199-4>.

- [39] W. Zhao, C. Song, B. Zheng, J. Liu, T. Viswanathan, Thermal recovery behavior of fluorinated single-walled carbon nanotubes, *J. Phys. Chem. B.* 106 (2002) 293–296. <https://doi.org/10.1021/jp0133135>.
- [40] R.R. Nair, W. Ren, R. Jalil, I. Riaz, V.G. Kravets, L. Britnell, P. Blake, F. Schedin, A.S. Mayorov, S. Yuan, M.I. Katsnelson, H.-M. Cheng, W. Strupinski, L.G. Bulusheva, A. V. Okotrub, I. V. Grigorieva, A.N. Grigorenko, K.S. Novoselov, A.K. Geim, Fluorographene: A Two-Dimensional Counterpart of Teflon, *Small.* 6 (2010) 2877–2884. <https://doi.org/10.1002/sml.201001555>.
- [41] Y. Sato, H. Watano, R. Hagiwara, Y. Ito, Reaction of layered carbon fluorides  $C_xF$  ( $x = 2.5-3.6$ ) and hydrogen, *Carbon* N. Y. 44 (2006) 664–670. <https://doi.org/10.1016/j.carbon.2005.09.029>.
- [42] B.H.F. Mcmurdie, M.C. Morris, E.H. Evans, B. Paretzkin, W. Wong-ng, Y. Zhang, C.R. Hubbard, Standard X-Ray Diffraction Powder Patterns from The JCPDS Research Associateship — International Centre for Diffraction Data Ammonium Hydrogen Phosphate ,  $NH_4H_2PO_4$  Barium Magnesium Germanium Oxide , Powder Diffr. 1 (1986) 334–345.
- [43] A.C. Ferrari, Raman spectroscopy of graphene and graphite: Disorder, electron-phonon coupling, doping and nonadiabatic effects, *Solid State Commun.* 143 (2007) 47–57. <https://doi.org/10.1016/j.ssc.2007.03.052>.
- [44] A.C. Ferrari, J.C. Meyer, V. Scardaci, C. Casiraghi, M. Lazzeri, F. Mauri, S. Piscanec, D. Jiang, K.S. Novoselov, S. Roth, A.K. Geim, Raman spectrum of graphene and

- graphene layers, *Phys. Rev. Lett.* 97 (2006) 1–4.  
<https://doi.org/10.1103/PhysRevLett.97.187401>.
- [45] J. Ek Weis, S.D. Costa, O. Frank, Z. Bastl, M. Kalbac, Fluorination of isotopically labeled turbostratic and bernal stacked bilayer graphene, *Chem. - A Eur. J.* 21 (2015) 1081–1087. <https://doi.org/10.1002/chem.201404813>.
- [46] A. Sadezky, H. Muckenhuber, H. Grothe, R. Niessner, U. Pöschl, Raman microspectroscopy of soot and related carbonaceous materials: Spectral analysis and structural information, *Carbon N. Y.* 43 (2005) 1731–1742.  
<https://doi.org/10.1016/j.carbon.2005.02.018>.
- [47] J.J. Kipling, J.N. Sherwood, P. V. Shooter, N.R. Thompson, Factors influencing the graphitization of polymer carbons, *Carbon N. Y.* 1 (1964).  
[https://doi.org/10.1016/0008-6223\(64\)90285-4](https://doi.org/10.1016/0008-6223(64)90285-4).
- [48] S.M. Lyth, S.R.P. Silva, Electron Field Emission from Water-Based Carbon Nanotube Inks, *ECS J. Solid State Sci. Technol.* 4 (2015) P3034–P3043.  
<https://doi.org/10.1149/2.0051504jss>.
- [49] J. Liu, B. V. Cuning, T. Daio, A. Mufundirwa, K. Sasaki, S.M. Lyth, Nitrogen-Doped Carbon Foam as a Highly Durable Metal-Free Electrocatalyst for the Oxygen Reduction Reaction in Alkaline Solution, *Electrochim. Acta.* 220 (2016) 554–561.  
<https://doi.org/10.1016/j.electacta.2016.10.090>.
- [50] S.M. Lyth, H. Shao, J. Liu, K. Sasaki, E. Akiba, Hydrogen adsorption on graphene foam synthesized by combustion of sodium ethoxide, *Int. J. Hydrogen Energy.* 39

- (2014) 376–380. <https://doi.org/10.1016/j.ijhydene.2013.10.044>.
- [51] M.B. Smith, Chapter 16 - Carbon-Carbon Bond-Forming Reactions: Carbocation and Oxocarbenium Ion Intermediates, 2017. <http://www.sciencedirect.com/science/article/pii/B9780128007204000167>.
- [52] V.H. Dalvi, P.J. Rossky, Molecular origins of fluorocarbon hydrophobicity, *Proc. Natl. Acad. Sci. U. S. A.* 107 (2010) 13603–13607. <https://doi.org/10.1073/pnas.0915169107>.
- [53] E. Disa, M. Dubois, K. Guérin, H. Kharbache, F. Masin, A. Hamwi, The effect of nanostructure on the thermal properties of fluorinated carbon nanofibres, *Carbon N. Y.* 49 (2011) 4801–4811. <https://doi.org/10.1016/j.carbon.2011.06.092>.
- [54] P.E. Pehrsson, W. Zhao, J.W. Baldwin, C. Song, J. Liu, S. Kooi, B. Zheng, Thermal fluorination and annealing of single-wall carbon nanotubes, *J. Phys. Chem. B.* 107 (2003) 5690–5695. <https://doi.org/10.1021/jp027233s>.
- [55] A. Oberlin, Carbonization and graphitization, *Carbon N. Y.* 22 (1984) 521–541. [https://doi.org/10.1016/0008-6223\(84\)90086-1](https://doi.org/10.1016/0008-6223(84)90086-1).
- [56] C. Casiraghi, Doping dependence of the Raman peaks intensity of graphene close to the Dirac point, *Phys. Rev. B - Condens. Matter Mater. Phys.* 80 (2009) 2–4. <https://doi.org/10.1103/PhysRevB.80.233407>.

## **Chapter 4. Application of Fluorinated Carbons in Microporous Layers**

### **4.1 Introduction**

In PEFCs, the gas diffusion layer (GDL) is located between the catalyst layer and the flow channel. This component is primarily made of carbon fiber, and has several roles including: (i) the supply of reactant gases; (ii) the exhaust of products; (iii) electrical connectivity; and (iv) water management [1]. At the cathode side of the membrane electrode assembly (MEA), oxygen is supplied through the GDL to the catalyst layer, where water is formed via the oxygen reduction reaction (ORR). The water generated in the catalyst layer is then ideally transported back through the GDL to the flow channel, eventually leaving the system via the exhaust. However, in circumstances where high power output is required, the rate of water generation in the catalyst layer increases. This can lead to water accumulation, preventing oxygen diffusion to the platinum catalyst surface, and causing a significant voltage drop. This phenomenon is called ‘flooding’, and decreases PEFC efficiency under high current density conditions [2].

To minimize flooding and improve water management, the carbon fibers in GDLs are generally coated with a thin layer of polytetrafluoroethylene (PTFE) to render them hydrophobic. In addition, a microporous layer (MPL) is used at the interface with the catalyst layer to aid water transport [11–15]. The MPL usually consists of carbon black with a hydrophobic binder such as PTFE. In the absence of an MPL, GDLs are prone to severe

flooding under high current density operation [7]. Therefore, the choice of an MPL with suitable properties is critical for water management in PEFCs.

There have been numerous studies on MPLs investigating the type of material used, the pore structure, the thickness, the PTFE content, and different wettability designs [1,10,11,13–26]. The PTFE content in the MPL is reported to significantly affect PEFC performance, with lower PTFE content leading to a greater likelihood of flooding. Higher PTFE content is reported to reduce the pore size, leading to lower gas permeability and thus higher diffusion losses. In addition, PTFE is electronically insulating, so higher PTFE loadings can lead to increased ohmic losses. As such alternative solutions to water management in PEFCs in which the amount of PTFE used is reduced could be highly advantageous.

Fluorinated carbon materials have also been explored in PEFCs in a few reports. For example, Nguyen et al. investigated fluorination of carbon fibers in the GDL via direct fluorination in fluorine gas and reported improved I-V performance in the mass diffusion limited current density region [13]. Carbon monofluoride decorated with platinum has been reported to be an effective electrocatalyst with high mass activity in PEFCs and enhanced mass diffusion in direct methanol fuel cells (DMFCs) [19]. Similarly, fluorinated carbon decorated with platinum as a cathode catalyst has been reported to improve durability by suppressing carbon corrosion. [20,21]. However, to the best of our knowledge there are no reports on the utilization of fluorinated carbons in the MPL of PEFCs.

In Chapter 3 the synthesis and characterization of highly graphitic superhydrophobic fluorinated carbon black powders are investigated. In this chapter, one of the synthesized fluorinated carbon black powders ( $\text{CF}_x\text{-C}_8$ ) is applied to the PEFC as an MPL material to

improve the water removal rate for improved PEFC performance. The performance of superhydrophobic fluorinated carbon based MPL and graphitized carbon black based MPL are also compared.

## **4.2 Experimental**

### **4.2.1 Preparation of the MPL**

Carbon black (Sigma-Aldrich, Japan) MPLs (CB-MPL) and fluorinated carbon MPLs (FC-MPL) were manufactured using identical processes. An MPL slurry was prepared by adding 2 g of carbon (either CB or FC), 0.5 g of methyl cellulose pore forming agent (Fujifilm Wako Chemicals, Japan), 14 ml of deionized water (Milli-Q, 18 M $\Omega$  cm), and 0.1 ml of Triton X-100 (Sigma-Aldrich, Japan) surfactant to a 100 ml polypropylene beaker. This mixture was homogenized for 15 min at 2000 rpm (Thinky Mixer AR-100). Then, 0.059 ml (corresponding to 0.089 g) of PTFE dispersion (60 wt%, Teflon<sup>TM</sup> 30B from Polysciences, Inc) was added to the mixture as a binder, followed by a second homogenization step for 15 min at 2000 rpm. To coat the MPL onto the Toray-GDL (5 wt% wetproofed TGP-H-060 Toray Paper), a 5 cm  $\times$  5 cm square of GDL was placed on a glass plate, and a 75  $\mu$ m thick stainless-steel mask with 3 cm  $\times$  3 cm opening was placed on top of the GDL (Figure 2.9). The MPL slurry was then coated onto the GDL using a doctor blade, then dried at 65  $^{\circ}$ C for one hour. Finally, the MPL-coated GDLs were heat-treated at 400 $^{\circ}$ C for one hour under air, to sinter the PTFE binder and decompose the methyl cellulose pore forming agent as well as any remaining Triton-X surfactant. Decomposition of these materials is confirmed by TGA in Figure 4.1. Manufactured MPL coated GDL is shown in Figure 4.2.

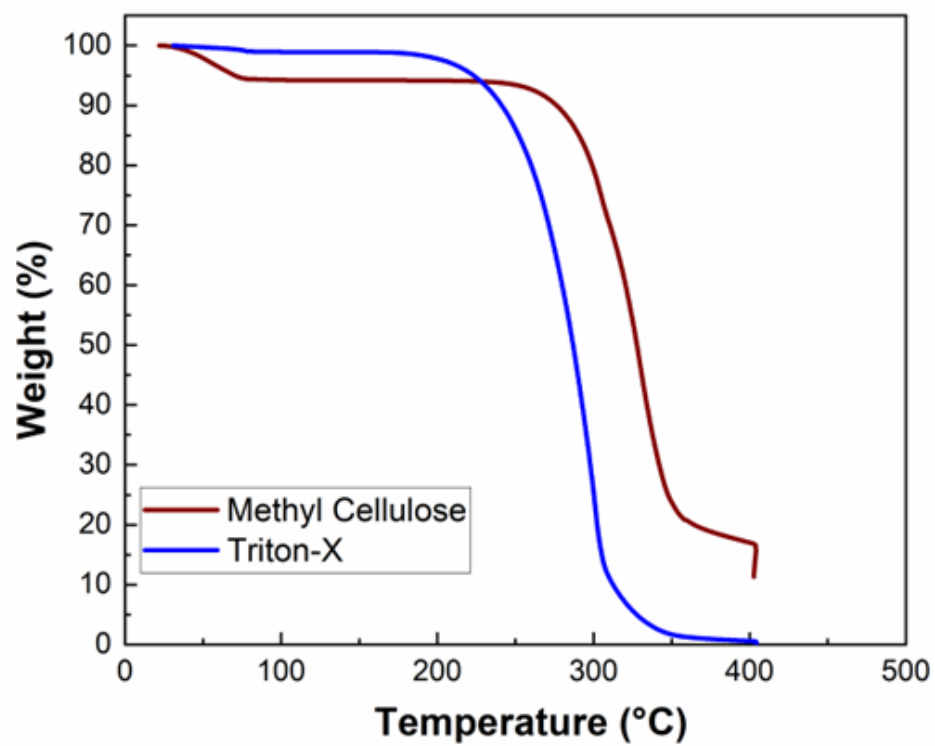


**Figure 4.1 TGA of Methyl Cellulose and Triton-X**

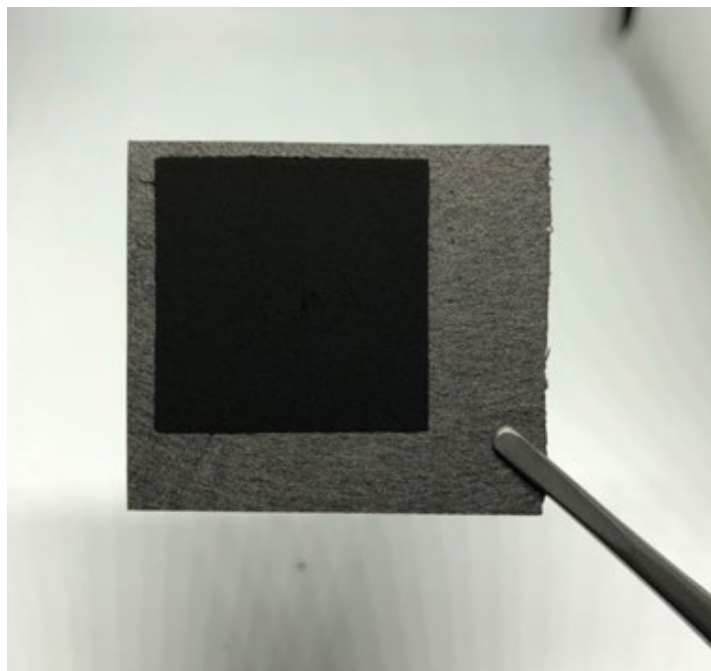


**Figure 4.2 Photo of a MPL coated GDL.**

In addition, free-standing MPLs were fabricated to aid with calculation of the porosity, by coating the slurry directly on a glass plate instead of a GDL, followed by the same drying and sintering steps (Figure 4.3). Several studies have reported an optimized PTFE loading in MPLs of about 20% [29,55,56]. One purpose of this study is to minimize the PTFE loading. Through trial-and-error, we determined that ~5 wt% PTFE loading was the minimum limit required to create mechanically stable free-standing MPLs. Thus, all MPLs used in this study had a thickness of ~35  $\mu\text{m}$  and 5 wt% PTFE content. The MPL porosities were calculated from the thickness, area, mass, and density of the different components using the following equation [22]:

$$\emptyset = 1 - \frac{V_S}{V_{MPL}} = 1 - \frac{m_{MPL} \cdot (\omega_c / \rho_c + \omega_B / \rho_B)}{d_{MPL} \cdot A} \quad \text{Eq. 4.1}$$

where  $\emptyset$  is the porosity of the MPL;  $V_S$  is the volume of the solid components (i.e. either PTFE and CB or PTFE and superhydrophobic fluorinated carbon (SHFC));  $V_{MPL}$  is the geometric volume of the MPL;  $m_{MPL}$  is the mass of the MPL;  $\omega_c$  is the mass fraction of the carbon component (0.95);  $\omega_B$  is the mass fraction of the PTFE binder (0.05);  $\rho_c$  is the density of the carbon component;  $\rho_B$  is the density of the PTFE binder;  $d_{MPL}$  is the thickness of the MPL; and  $A$  is the area of the MPL (1 cm  $\times$  1 cm).

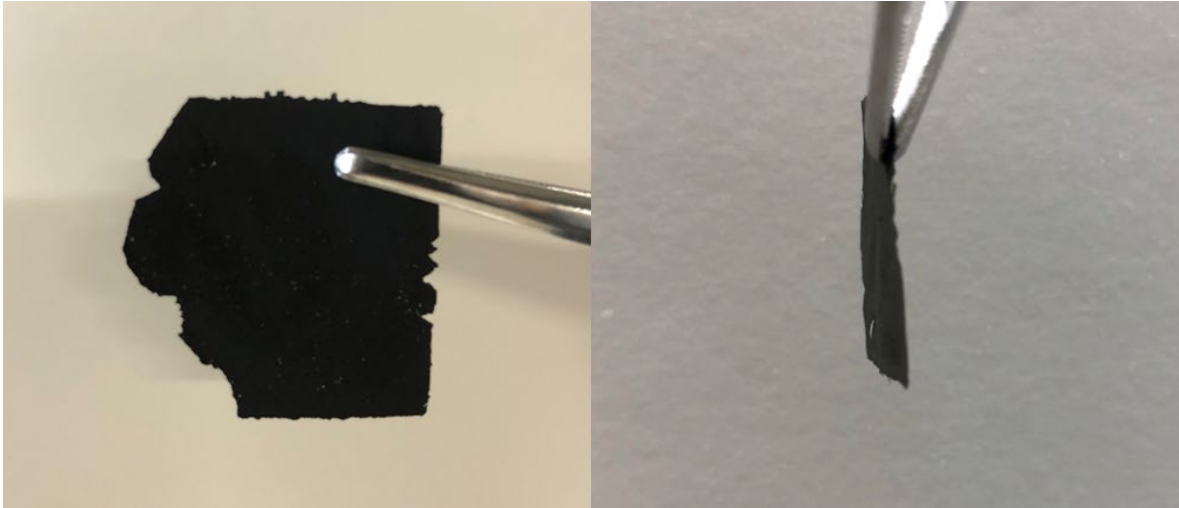


**Figure 4.3 Photo of a free-standing MPL.**

#### **4.2.2 Preparation of the Membrane Electrode Assembly (MEA)**

The catalyst ink was prepared by mixing Pt/C (TEC10E50E, lot 1019-8581, 46.8 wt<sub>Pt</sub>%, Tanaka, Japan) with 5 wt% Nafion solution (Wako, Japan), deionized water, and super-dehydrated ethanol (99.5 vol%, Wako, Japan). The catalyst ink was stirred overnight, then sonicated for 30 minutes just before use (SMT Corporation, Ultra Sonic Homogenizer UH-600). Nafion 212 membranes were placed onto movable-hot plate and masked, leaving an exposed area of 1 cm<sup>2</sup>. The catalyst ink was then sprayed directly onto the Nafion membrane using pulsed spray mode from an automated spraying device (Nordson K.K.), with a catalyst loading of 0.3 mg<sub>Pt</sub>/cm<sup>2</sup> and a Nafion content of 28 wt% [23], at both the anode and cathode. The resulting MEAs were finally hot pressed at 132 °C and 0.3 kN for 180 s (Sinto Digital Press CYPT-10).

#### **4.2.3 Thermogravimetric Analysis Tests**

During preparation the MPL, a slurry was prepared with methyl cellulose and Triton-X to improve the dispersibility and rheological properties for printing onto the GDL. These are assumed to decompose during heat treatment of the resulting MPL-coated GDL at 400°C. To confirm this, TGA was conducted on methyl cellulose and Triton-X under similar heat treatment conditions (Figure 4.1).

#### **4.2.4 Fuel Cell Polarization Tests**

Fuel cell tests were performed using a 1 cm<sup>2</sup> active area single cell obtained from the Japanese Automotive Research Institute (JARI) with serpentine type flow fields. The performance of

the different MPL-coated GDLs was investigated by measuring polarization curves at two different cell temperatures (45 °C and 80 °C). The temperature of 80°C was selected to reproduce conventional PEFCs operating conditions. The lower temperature of 45 °C was selected as an extreme condition in which water condensation readily causes flooding even at lower current density, to highlight the effect of using superhydrophobic MPLs. Three different conditions of relative humidity (RH) were also tested (80 %, 100 %, 120 %) at both the anode and cathode. To reach 120% relative humidity with a cell temperature of 80 °C, the humidifier temperature was maintained at 85 °C. For a cell temperature of 45 °C, the humidifier was held at 49 °C. Fuel cell performance tests at 120% RH and 80 °C are not shown because of water condensation in uninsulated sections of the pipes between the cell and the humidifier (85 °C), disrupting the gas flow and preventing stable cell I-V performance from being measured.

The constant volumetric flow rates were 0.139 L/min hydrogen and 0.332 L/min oxygen at anode and cathode, respectively (counter flow conditions). A fuel cell test station (AUTOPEM-CVZ01, Toyo Corporation, Japan) was used to control the humidification, cell temperature, and gas flow. Polarization curves were measured using an electrochemical interface impedance analyzer (Solartron SI-1287). Prior to the polarization curve measurement, each cell was conditioned at 0.6 V for 5 hours.

#### 4.2.5 Air Permeability Tests

Through-plane (transverse) air permeability tests were conducted under ambient conditions with dry air flow, using the set up summarized in Ref [59], applying Darcy's law (Eq.2): [60]

$$Q = \frac{K \cdot A \cdot \Delta P}{\mu \cdot L} \quad \text{Eq. 4.2}$$

where  $Q$  is the volumetric flow rate ( $\text{m}^3\text{s}^{-1}$ );  $K$  is the air permeability ( $\text{m}^2$ );  $A$  is the area of GDL or MPL coated GDL ( $0.5 \text{ cm}^2$ );  $\Delta P$  is the pressure difference between the inlet and outlet;  $\mu$  is Newtonian viscosity ( $18.37 \text{ kgm}^{-1}\text{s}$ ); and  $L$  is the sample thickness (m). To measure air permeability, a  $1 \text{ cm} \times 1 \text{ cm}$  GDL sample was placed between two plates, each with a  $0.5 \text{ cm}^2$  diameter hole for air flow. To avoid leakage, PTFE gaskets were also used. PTFE gaskets were also used. The compression was set to 1 MPa, similar to the pressure used in PEFC polarization measurements. The air pressure was set by the volumetric flow rate to by 1.23 kPa, as suggested in the Gurley Method [25].

#### 4.2.6 Water Contact Angle Measurements

The water contact angles of the different MPLs were measured in two different ways. In the first method, the surface contact angle was measured using the pendant drop method with an automated analyzer (DMs-401, Kyowa Interface Science Co., Ltd, Japan). All GDLs have a PTFE loading of 5 wt%. Contact angles were measured using the Pendant Drop Method

and to minimize the effect of gravity, the droplet size was fixed at around 1  $\mu\text{L}$ . To measure the contact angle of the fluorinated carbon powder, it was first pressed between two glass plates to create smooth surface.

In the second method, the contact angle of the pores was measured using the same equipment displayed in Fig.1, and by applying the Young-Laplace equation (Eq. 4.3):

$$d = \frac{4 \cdot \sigma \cdot \cos \theta}{P_C} \quad \text{Eq.4.3}$$

where  $d$  is the pore diameter;  $\sigma$  is the surface tension of the liquid;  $\theta$  is the contact angle, and  $P_C$  is the capillary pressure. To measure the contact angle within the largest pore, first the maximum pore size of the MPL was calculated using Eq.3. To measure the maximum pore size, samples were immersed in a low surface tension liquid (Galpore,  $\sigma = 0.0156 \text{ Nm}^{-1}$ , contact angle =  $0^\circ$ ) in a vacuum desiccator for two hours. Then, the MPL sample was carefully removed, placed in the sample holder, and sealed with a PTFE gasket. Then, air flow was supplied through the plane of the sample, and the inlet air pressure recorded. Since the largest pore has the lowest capillary pressure, it can be assumed that this will be the first to be blown out. The pressure at which this first occurs is then used in Eq.3. to estimate the maximum pore diameter [24]. After this maximum pore size calculation, pressurized water was then supplied to the same sample. The pressure at which water starts to flow though the largest pore of the GDL corresponds to the water breakthrough pressure. After determination of water breakthrough pressure, the contact angle of the pores can be calculated via Eq.3.

Here, the surface tension of water at 25° C is assumed to be 0.0720 Nm<sup>-1</sup>, and samples size was 0.5 cm<sup>2</sup>.

#### 4.2.7 Oxygen Transport Resistance

The total oxygen transport resistance was calculated from the limiting current density under the differential relative humidity conditions of the supplied gasses, using the following equation:

$$R_T = \frac{4 \cdot F \cdot P_{O_2}}{i_{lim} \cdot R \cdot T} \quad \text{Eq.4.4}$$

Where  $R_T$  is the total oxygen transport resistance of the cell (sm<sup>-1</sup>),  $F$  is the Faraday constant (96485 C mol<sup>-1</sup>),  $P_{O_2}$  is the oxygen partial pressure (Pa),  $R$  is the gas constant (8314 J mol<sup>-1</sup>K<sup>-1</sup>),  $T$  is the cell temperature (K) and  $i_{lim}$  is the limiting current density at 0.2 V.

The oxygen transport resistance was calculated at both 80 °C and 45 °C cell temperature conditions for each different MPL. At high cell temperature, the oxygen transport resistance was measured at relative humidity of 80, 100, and 120 %. At low cell temperature, the oxygen transport resistance was measured at 80, 100, 120, 160, and 200 % relative humidity. The flow rate of the supplied gases at both the anode and cathode was 1 L/min. The oxygen concentration was 2 vol% at the cathode side, and nitrogen was used as the balance gas.

## **4.3 Results and Discussions**

### **4.3.1 Scanning Electron Microscopy (SEM) and Transmission Electron Microscopy (TEM) Imaging**

The microstructure was investigated by SEM and TEM, revealing a spheroidal microstructure similar to carbon black (Figure 4.4) [17]. The nanoparticles appear to cluster together with a flocculent structure, leaving micron-scale voids. The TEM images show that the particles are spheroidal and solid, with most particle sizes varying between around 50 and 100 nm in diameter. These SEM and TEM images are representative, although several much larger particles around 500 nm in diameter were also observed in some images (Figure 4.5). Meanwhile, Figure 4.6 shows SEM images of graphitized carbon black for comparison, confirming that the microstructure of carbon black and fluorinated carbon are similar.

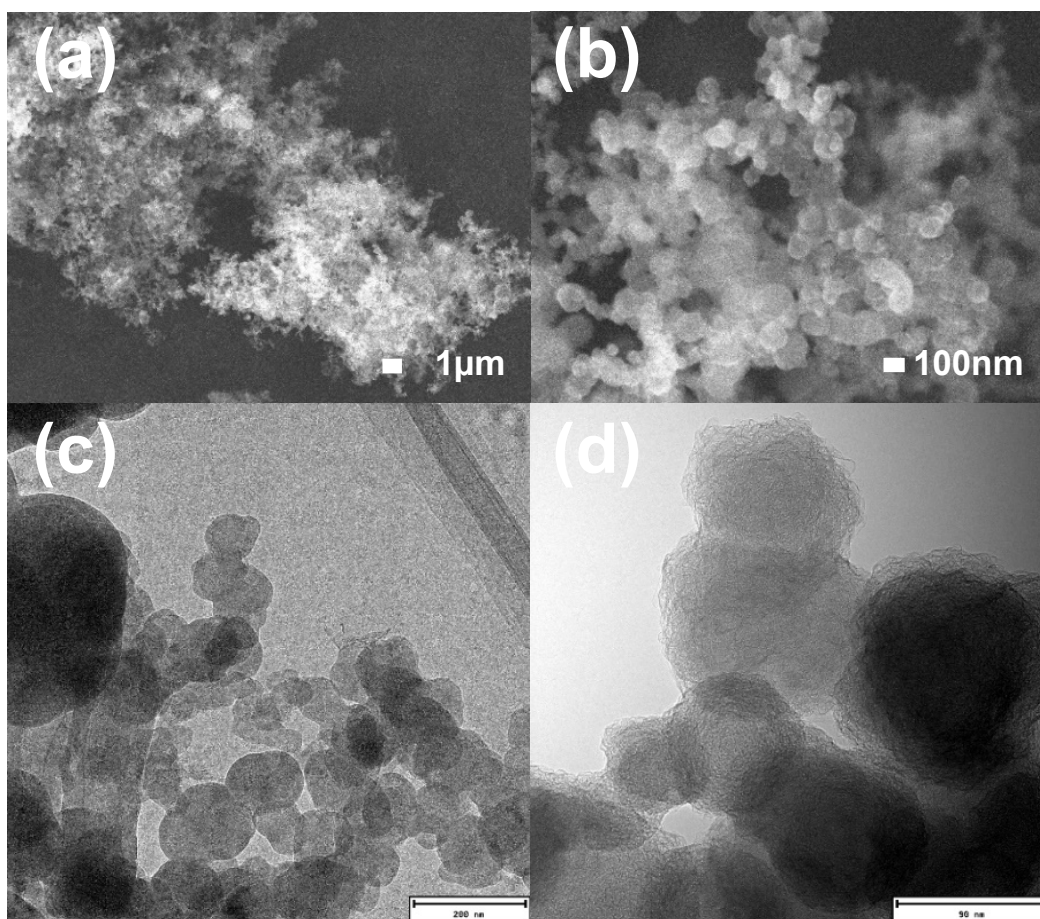


**Figure 4.4** Electron microscopy showing the microstructure of the fluorinated carbons used in this study: (a-b) SEM images, (c-d) TEM images.

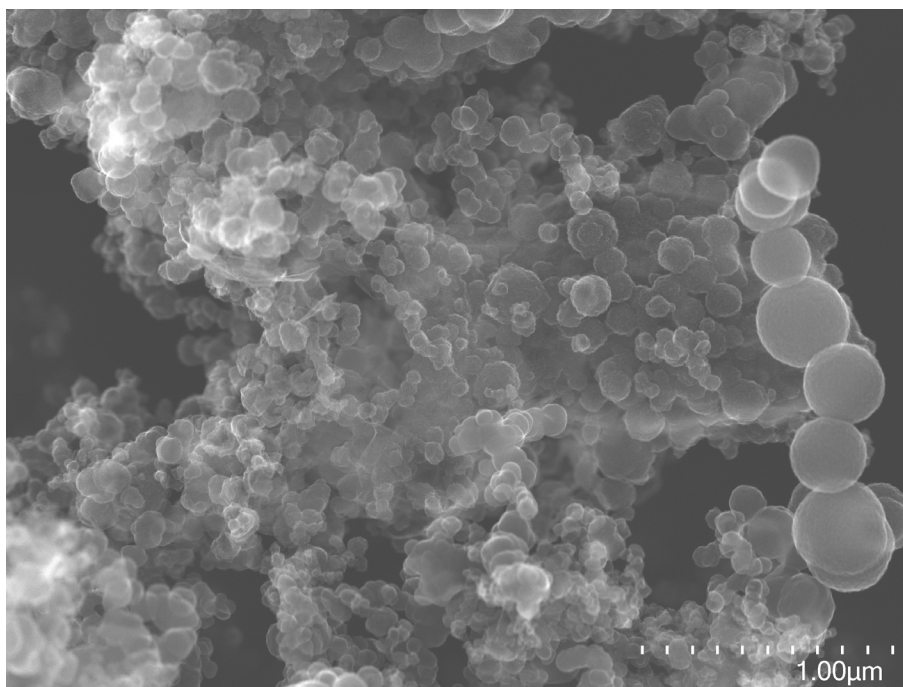


**Figure 4.5 SEM image of fluorinated carbon with large particles**

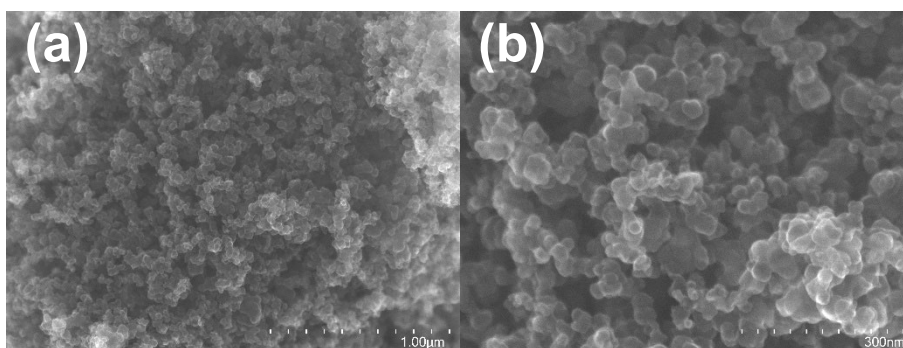


**Figure 4.6 (a-b) SEM images of carbon black.**

### 4.3.2 Surface Area and Porosity

Nitrogen adsorption/desorption isotherms of the fluorinated carbon compared with graphitized carbon black are shown in Figure 4.7. Brunauer-Emmett-Teller (BET) and Barrett-Joyner-Halenda (BJH) methods were used to calculate the specific surface area and pore size distribution. Both samples have Type III isotherms, characteristic of nonporous materials [26]. The specific surface area of the fluorinated carbon is 40 m<sup>2</sup>/g. This is much lower compared to non-fluorinated porous carbons prepared in a similar manner and previously reported by our group [7,45]. This is mainly attributed to the preferential formation of NaF in this case over NaOH, which acts as an activation agent in our unfluorinated carbons. Meanwhile, differences in pressure within the PTFE crucible and the viscosity of the melting precursors as they decompose may also be a factor. Furthermore, fluorination has been previously reported to decrease surface area and pore volume by blocking micropores [27]. Nevertheless, the surface area is of a similar order to that of the graphitized carbon black reference sample (115 m<sup>2</sup>/g), suggesting that this relatively low surface area is not necessarily an issue for MPL-related applications. BJH results also confirm that the fluorinated carbon is non-porous. On the other hand, graphitized carbon black shows a certain pore size distribution between 20 and 100 nm. However, when compared with other porous carbon materials, graphitized carbon black can also effectively be considered as non-porous [6,46].

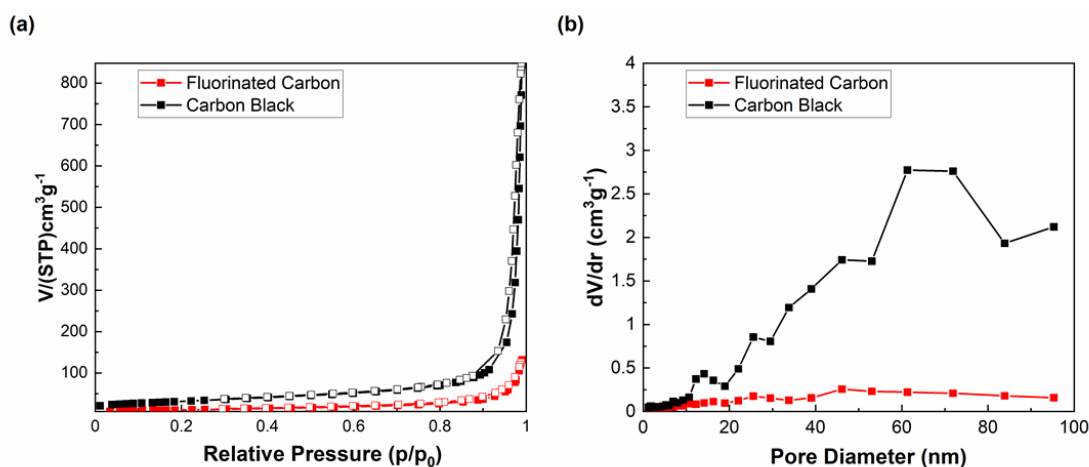


**Figure 4.7 (a) Brunauer-Emmett-Teller (BET) nitrogen adsorption isotherms, and (b) Barrett-Joyner-Halenda (BJH) pore size distribution graphs.**

### 4.3.3 Density Measurement and Calculation

The skeletal density of the samples was measured by adding 5 ml of ethanol into a graduated cylinder, and then sample powder was added until the volume increased by exactly 0.1 ml. The increase in mass was measured and the density calculated by dividing this number by the volume displaced. Using this method, the skeletal density of graphitized carbon black was measured to be  $1.9 \text{ g cm}^{-3}$  which is within the range quoted by the manufacturer (i.e.  $1.5$  to  $1.9 \text{ g cm}^{-3}$ ) [28]. The density of the fluorinated carbon was measured to be  $2.04 \text{ g cm}^{-3}$ . This higher density compared to carbon black is attributed to the fact that fluorine has a higher atomic mass compared to carbon.

Assuming that the carbon particles are spherical and non-porous (as discussed in the previous paragraph), the mean particle size can be calculated using the following equation [29]:

$$L_D = 6000/(\rho_s \cdot a_{s,BET}) \quad \text{Eq.4.5}$$

where,  $L_D$  is mean particle diameter,  $\rho_s$  is the density of the adsorbent, and  $a_{s,BET}$  is the BET specific surface area. According to this equation, the mean particle diameter of carbon black 27.4 nm, in close agreement with data quoted by the manufacturer (24 nm) [30], confirming that this method is reliable. Meanwhile, the mean particle size of the fluorinated carbon sample is calculated to be 74.4 nm, which is in close agreement with the particle size observed in the SEM and TEM images (Figure 4.4).

#### 4.3.4 Thermogravimetric Analysis (TGA)

Figure 4.8 shows thermogravimetric analysis (TGA) of the fluorinated carbon sample and graphitized carbon black, measured under constant air flow. The results show that the fluorinated carbon is thermally stable in air up until 500 °C, above which the material decomposes. This confirms that the material should be resilient to thermal decomposition at typical temperatures used in PEFCs. On the other hand, carbon black shows a slightly higher thermal stability up to 600 °C. This is attributed to the lower thermodynamic stability of covalent C-F bonds compared to the C=C bonds in graphitized carbon black [27].

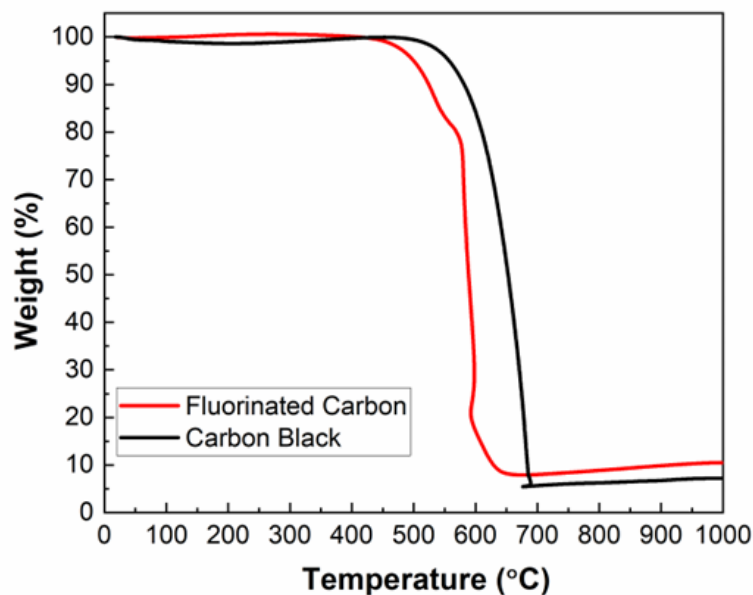


**Figure 4.8 TGA of fluorinated carbon and graphitized carbon black in air.**

## **4.4 Microporous Layer Characterization**

### **4.4.1 Scanning Electron Microscopy Imaging**

The different microstructures of MPLs fabricated using fluorinated carbon (FC-MPL) and graphitized carbon black (CB-MPL) were investigated by SEM (Figure 4.9). In both images, pores of several microns in size are observed, which is attributed to decomposition of the methyl cellulose pore forming agent, as expected. Meanwhile, the surface of the CB-MPL appears to be relatively smooth and uniform compared to that of the FC-MPL. This is attributed to the smaller particle diameter.

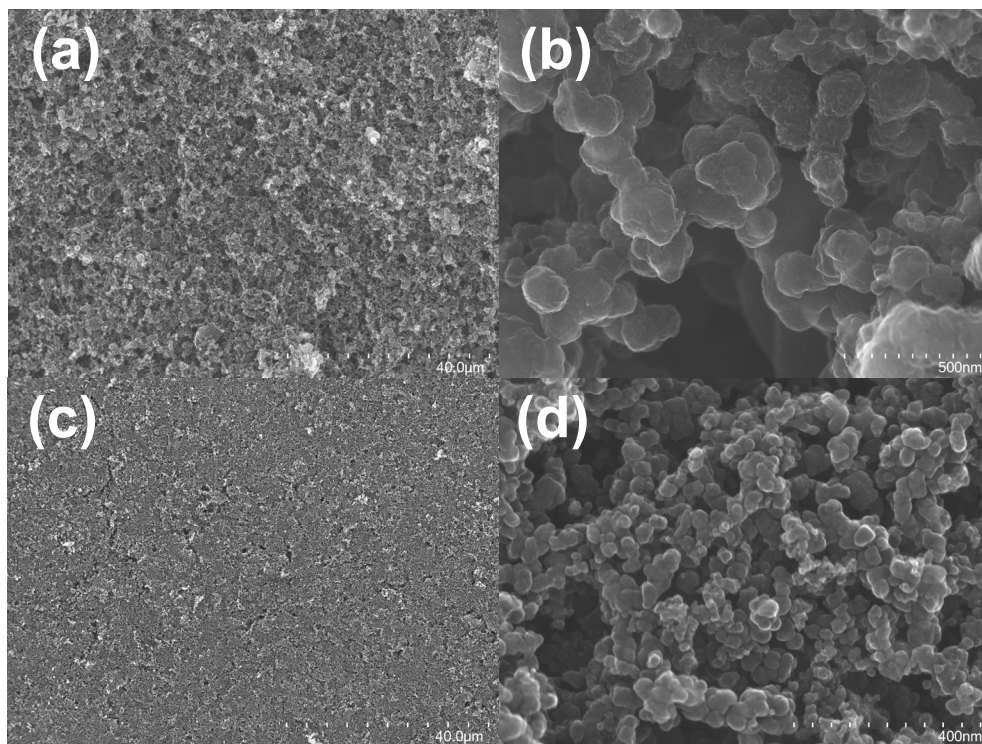


**Figure 4.9 SEM images of MPL surface at different magnifications: (a-b) FC-MPL; (c-d) CB-MPL.**

#### **4.4.2 Water Contact Angle Measurement and Porosity Calculation of MPLs**

To confirm if fluorination of carbon can affect the water repelling properties of the resulting MPLs, the water contact angle (WCA) was measured and compared with other MPL-coated GDLs (Figure 4.10). The WCA of the as-synthesized fluorinated carbon sample (FC) after pressing is  $160^\circ$ , confirming that the synthesized material is indeed superhydrophobic (i.e.  $\theta > 150^\circ$ ) (Figure 4.10 (a)). After incorporating the fluorinated carbon into an MPL (FC-MPL), the WCA is  $151^\circ$  (Figure 4.10 (b)). This slight decrease is attributed to the effect of residual pore forming agent (methyl cellulose) added during slurry preparation, which does not completely decompose during the heating step. Meanwhile, the WCA of the identically

prepared CB-MPL is much lower at  $131^\circ$  (Figure 4.10 (c)). Finally, the WCA of a commercial Toray-GDL (TGP-H-060, Toray, Japan) was measured to be  $130^\circ$  (Figure 4.10 (d)). These results confirm that the high WCA of the fluorinated carbon translates to significantly improved WCA in MPLs incorporating this material. The results also suggest that the WCA of the MPL is not dominated by the presence of the PTFE binder when the PTFE loading is sufficiently low (e.g. 5 wt%), but mainly instead on the properties of the carbon itself. This may not be the case for higher PTFE loading.

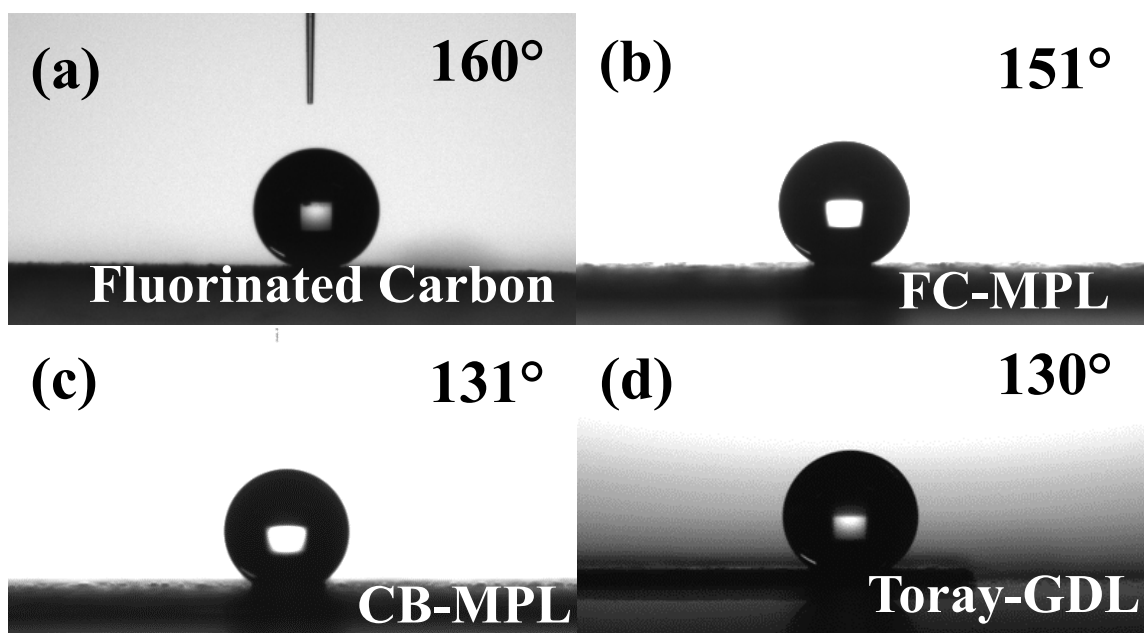


**Figure 4.10** Surface water contact angle (WCA) measurements for: (a) pressed fluorinated carbon (FC); (b) FC-MPL; (c) CB-MPL; and (d) Toray-GDL (TGP-H-060).

Porosity is an important factor which affects mass transport resistance significantly. When porosity is increased, the total resistance to molecular diffusion in the system decreases. Here,

the porosities of the free-standing FC-MPL and CB-MPL samples were calculated according to Eq.1 to be 76% and 83%, respectively, and the maximum pore diameters were similar at 42.5 and 40.5  $\mu\text{m}$  (Figure 4.11(a)). Meanwhile, Toray-GDL had a larger maximum diameter of 61.7  $\mu\text{m}$ , primarily because it does not include an MPL, exposing the larger pores defined by the spaces between carbon fibers.

The experimentally determined WCA above can be described as the *apparent contact angle*, which is dependent on both the surface interaction energy and the surface roughness of the sample. Once the maximum pore size has been determined, the *Young's* contact angle can be estimated using the Young-Laplace Equation (Eq.4.3), and this value is independent of the surface roughness. Especially in this composite material, the Young's contact angle is an important parameter to confirm to what extent the apparent contact angle is due to the hydrophobic nature of the fluorinated carbon and what extent to the surface roughness. Both the Toray-GDL and the CB-MPL have similar Young's WCA of around  $130^\circ$  (Figure 4.11(b)), consistent with the surface WCA measurement, and in agreement with prior studies [13]. In contrast, the Young's WCA for the FC-MPL is much higher at  $151^\circ$ . This agrees with the apparent WCA, confirming that the superhydrophobic nature of these MPLs is due to the nature of the material, rather than any change in surface roughness.

#### **4.4.3 Air permeability and Oxygen Transport Resistance Tests**

The through-plane air permeability of the MPL-coated GDLs and Toray-GDL was also measured (Figure 4.11(c)). FC-MPL has the lowest permeability, and CB-MPL has slightly higher permeability. Since the maximum pore diameter and the thickness of the CB-MPL

and the FC-MPL are similar, the lower air permeability in FC-MPL may be the result of higher tortuosity due to lower porosity, and/or the smaller mean pore diameter. In contrast, the air permeability of Toray-GDL is over an order of magnitude higher, due to the much larger pores in the absence of an MPL. These results show that air permeability is dominated by the MPL rather than the GDL.

Meanwhile, the oxygen transport resistance through the MPL-coated GDLs was measured in situ in a PEFC single cell (Figure 4.11(d)), as summarized in the experimental section. The results clearly show that the FC-MPL has significantly lower oxygen transport resistance compared to CB-MPL, at both temperatures. This seemingly contradicts the air permeability results, but this difference is attributed to the in situ high humidity conditions within the cell and therefore can be directly attributed to the superhydrophobic nature of the FC-MPL. Due to the superior water-repellent characteristic of fluorinated carbon, FC-MPL has a faster water removal rate, which is confirmed by the oxygen transport resistance test. Furthermore, the air permeability test results in Figure 4.11(c) indicate that CB-MPL has better air permeability, which we attribute to lower tortuosity. However, even though the FC-MPL displays lower air permeability, under high humidity conditions it shows lower oxygen transport resistance. This indicates that the available pores for oxygen transport are higher than that of CB-MPL (Figure 4.11(d)). As such, due to the superhydrophobic nature of the FC-MPL, the water produced in the catalyst layer is transferred faster than in the case of CB-MPL, increasing the available pores for oxygen transport. In all cases, the total oxygen transport resistance does not significantly vary with relative humidity, indicating that water

accumulation in the MPL-coated GDLs and the catalyst layers does not change significantly under high humidity conditions [36,37].

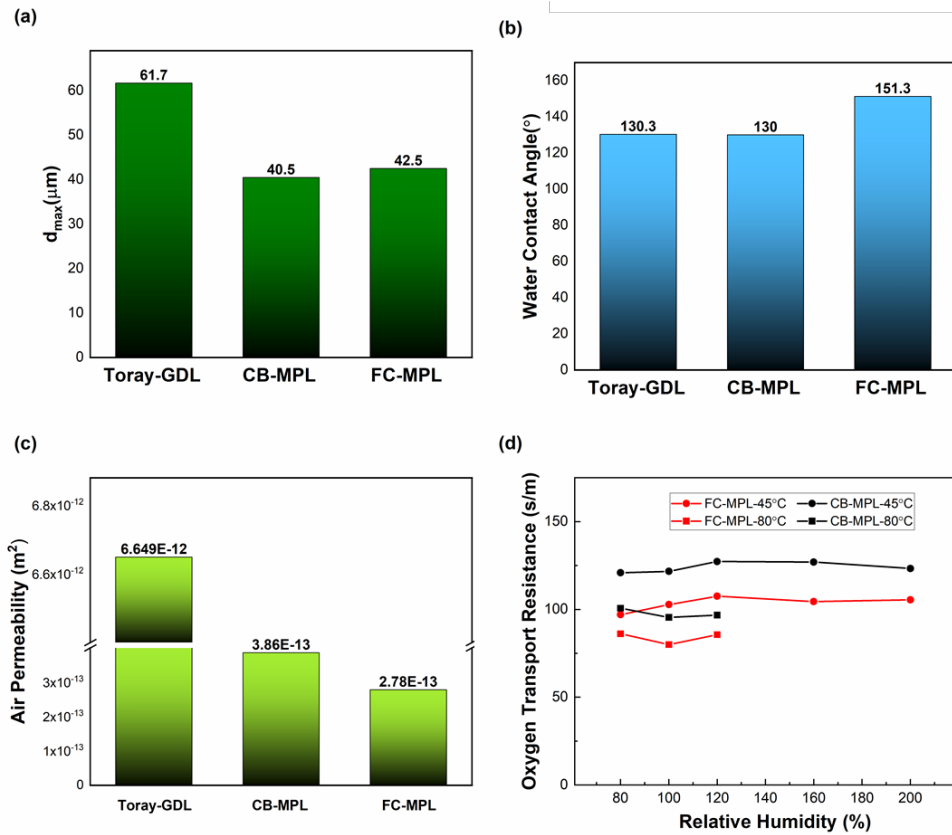


**Figure 4.11 (a) Maximum pore diameter; (b) internal water contact angle; (c) air permeability; and (d) oxygen transport resistance for Toray-GDL, CB-MPL and FC-MPL.**

#### 4.4.4 Single Cell Characterization

Finally, PEFCs were fabricated incorporating the FC-MPL, and compared to identically prepared cells using the CB-MPL, at cell temperatures of 45 °C and 80 °C. At 45 °C, the

performance of the cell was measured at 80, 100 and 120 % RH, whilst at 80 °C the cell was measured at 80 and 100 % RH.

The IR-free polarization curves reveal a clear difference in the mass diffusion limited current density region between the two MPLs, regardless of measurement temperature, with the FC-MPL cell having significantly higher cell voltage compared to the CB-MPL (Figure 4.12 (a-b)). For example, at 80 °C and 100% RH, the limiting current densities were measured to be 1.61 A/cm<sup>2</sup> and 1.72 A/cm<sup>2</sup> for the CB-MPL and the FC-MPL, respectively. Similarly, at 45 °C and 100% the limiting current densities were measured to be ~1.03 A/cm<sup>2</sup> and 1.14 A/cm<sup>2</sup>, respectively. This high current density region is where flooding normally occurs and disrupts oxygen diffusion to the catalyst surface, resulting in the observed voltage drop. However, the use of superhydrophobic fluorinated carbon in the MPL appears to improve removal of water from the cathode side of the cell, suppressing this voltage drop. This is confirmed and highlighted when the concentration overvoltage is separated from the polarization curves (Figure 4.12(c-d)).

Furthermore, when the ohmic regions of the polarization curves are compared, there is little difference between FC-MPL and CB-MPL (Figure 4.12(e-f)). This indicates that the doping of electronegative fluorine atoms into the carbon structure does not significantly lower the electronic conductivity of the material, and therefore that ohmic losses can be avoided. As discussed in the elemental analysis section, this may be because the fluorine atoms are mainly concentrated at the surface of the carbon nanoparticles rather than throughout the bulk.

The effect of humidity on the polarization curves was also investigated. At the relatively low temperature of 45 °C, the limiting current density does not change significantly with

increasing humidity for either MPL-coated GDL. This may be because the amount of water which condenses at the cathode side of the cell does not change significantly between 80 and 120 % RH (as also inferred from oxygen transport resistance test results in Figure 4.12(d)). Meanwhile, at higher cell temperature (80 °C), there is a clear decrease in cell voltage as the relative humidity increase, especially in the mass diffusion limited current density region. This is attributed to a greater degree of water condensation at the cathode side of the cell at higher humidity, resulting in flooding and a corresponding voltage drop due to restriction of oxygen supply to the catalyst.

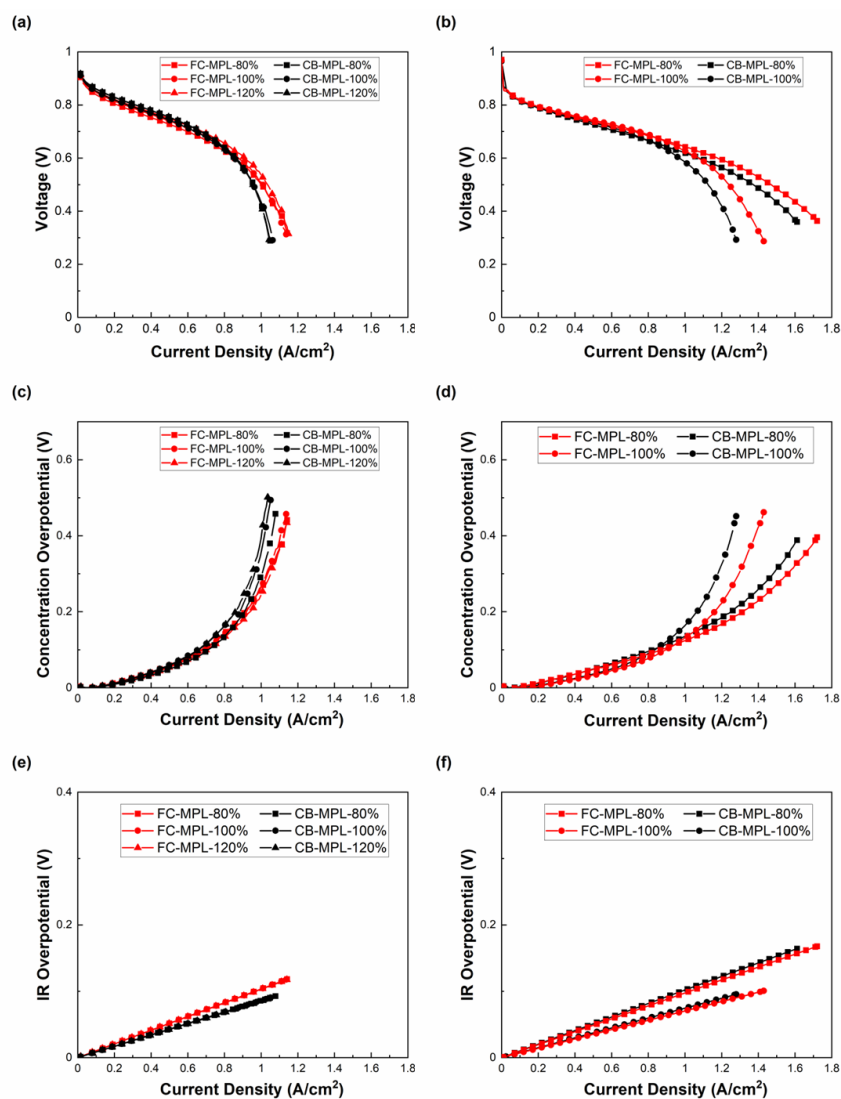


**Figure 4.12** Single cell PEFC measurements under different relative humidity conditions. Polarization curves (IR-free) at cell temperatures of (a) 45 °C and (b) 80 °C. Concentration overvoltage at (c) 45 °C (d) 80 °C. IR overpotential at (e) 45 °C and (f) 80 °C.

## 4.5 Summary and Conclusions

In this chapter, superhydrophobic fluorinated carbon nanoparticles were uniquely synthesized from fluorinated alcohol. The resulting superhydrophobic fluorinated carbon powder had similar microstructure and morphology to commercially available carbon black, but with a fluorine content of 1.9 at.%. This powder was applied to a GDL to create a superhydrophobic MPL with a water contact angle of 150 °, despite the relatively low PTFE loading of 5 wt%. The FC-MPL displayed reproducibly superior I-V performance in a fuel cell at high current density. For example, at 80 °C and 100% RH the limiting current density was 1.61 A/cm<sup>2</sup> for the carbon black-based MPL, increasing to 1.72 A/cm<sup>2</sup> for the FC-MPL. These improvements in performance are attributed to lower oxygen transport resistance in the case of the FC-MPL (105 s/m at 80°C) compared to CB-MPL (125 s/m at 80°C). Therefore, the improved I-V performance is directly attributed to enhanced water removal from the microporous layer due to the superhydrophobic nature of the fluorinated carbon. This work is expected to result in the design of more efficient PEFCs which can operate at higher current density, with lower PTFE content.

## 4.6 References

- [1] P.T. Moseley, Fuel Cell Systems Explained, 2001. [https://doi.org/10.1016/s0378-7753\(00\)00571-1](https://doi.org/10.1016/s0378-7753(00)00571-1).
- [2] H. Li, Y. Tang, Z. Wang, Z. Shi, S. Wu, D. Song, J. Zhang, K. Fatih, J. Zhang, H. Wang, Z. Liu, R. Abouatallah, A. Mazza, A review of water flooding issues in the proton exchange membrane fuel cell, J. Power Sources. 178 (2008) 103–117. <https://doi.org/10.1016/j.jpowsour.2007.12.068>.
- [3] U. Pasaogullari, C.Y. Wang, Two-phase transport and the role of micro-porous layer in polymer electrolyte fuel cells, Electrochim. Acta. 49 (2004) 4359–4369. <https://doi.org/10.1016/j.electacta.2004.04.027>.
- [4] M.S. Ismail, T. Damjanovic, D.B. Ingham, M. Pourkashanian, A. Westwood, Effect of polytetrafluoroethylene-treatment and microporous layer-coating on the electrical conductivity of gas diffusion layers used in proton exchange membrane fuel cells, J. Power Sources. 195 (2010) 2700–2708. <https://doi.org/10.1016/j.jpowsour.2009.11.069>.
- [5] T. Van Nguyen, A. Aghasani, X. Wang, V. Yarlagadda, A. Kwong, A.Z. Weber, P. Deevanhxay, S. Tsushima, S. Hirai, Hydrophobic Gas-Diffusion Media for Polymer-Electrolyte Fuel Cells by Direct Fluorination, J. Electrochem. Soc. 162 (2015) F1451–F1460. <https://doi.org/10.1149/2.0411514jes>.
- [6] J. Zhang, B. Wang, J. Jin, S. Yang, G. Li, A review of the microporous layer in proton exchange membrane fuel cells: Materials and structural designs based on water

- transport mechanism, *Renew. Sustain. Energy Rev.* 156 (2022) 111998. <https://doi.org/10.1016/j.rser.2021.111998>.
- [7] Y. Tabe, Y. Aoyama, K. Kadowaki, K. Suzuki, T. Chikahisa, Impact of micro-porous layer on liquid water distribution at the catalyst layer interface and cell performance in a polymer electrolyte membrane fuel cell, *J. Power Sources*. 287 (2015) 422–430. <https://doi.org/10.1016/j.jpowsour.2015.04.095>.
- [8] F. Aldakheel, M.S. Ismail, K.J. Hughes, D.B. Ingham, L. Ma, M. Pourkashanian, D. Cumming, R. Smith, Gas permeability, wettability and morphology of gas diffusion layers before and after performing a realistic ex-situ compression test, *Renew. Energy*. 151 (2020) 1082–1091. <https://doi.org/10.1016/j.renene.2019.11.109>.
- [9] O.M. Orogbemi, D.B. Ingham, M.S. Ismail, K.J. Hughes, L. Ma, M. Pourkashanian, On the gas permeability of the microporous layer used in polymer electrolyte fuel cells, *J. Energy Inst.* 91 (2018) 894–901. <https://doi.org/10.1016/j.joei.2017.09.006>.
- [10] M.S. Ismail, D. Borman, T. Damjanovic, D.B. Ingham, M. Pourkashanian, On the through-plane permeability of microporous layer-coated gas diffusion layers used in proton exchange membrane fuel cells, *Int. J. Hydrogen Energy*. 36 (2011) 10392–10402. <https://doi.org/10.1016/j.ijhydene.2010.09.012>.
- [11] O.M. Orogbemi, D.B. Ingham, M.S. Ismail, K.J. Hughes, L. Ma, M. Pourkashanian, The effects of the composition of microporous layers on the permeability of gas diffusion layers used in polymer electrolyte fuel cells, *Int. J. Hydrogen Energy*. 41 (2016) 21345–21351. <https://doi.org/10.1016/j.ijhydene.2016.09.160>.

- [12] C. Simon, D. Kartouzian, D. Müller, F. Wilhelm, H.A. Gasteiger, Impact of Microporous Layer Pore Properties on Liquid Water Transport in PEM Fuel Cells: Carbon Black Type and Perforation, *J. Electrochem. Soc.* 164 (2017) F1697–F1711. <https://doi.org/10.1149/2.1321714jes>.
- [13] C.M. Long, M.A. Nascarella, P.A. Valberg, Carbon black vs. black carbon and other airborne materials containing elemental carbon: Physical and chemical distinctions, *Environ. Pollut.* 181 (2013) 271–286. <https://doi.org/10.1016/j.envpol.2013.06.009>.
- [14] J.T. Gostick, M.A. Ioannidis, M.W. Fowler, M.D. Pritzker, On the role of the microporous layer in PEMFC operation, *Electrochem. Commun.* 11 (2009) 576–579. <https://doi.org/10.1016/j.elecom.2008.12.053>.
- [15] C. Li, D. Si, Y. Liu, J. Zhang, Y. Liu, Water management characteristics of electrospun micro-porous layer in PEMFC under normal temperature and cold start conditions, *Int. J. Hydrogen Energy.* 46 (2021) 11150–11159. <https://doi.org/10.1016/j.ijhydene.2020.05.271>.
- [16] C.J. Tseng, S.K. Lo, Effects of microstructure characteristics of gas diffusion layer and microporous layer on the performance of PEMFC, *Energy Convers. Manag.* 51 (2010) 677–684. <https://doi.org/10.1016/j.enconman.2009.11.011>.
- [17] A.T. Najafabadi, M.J. Leeuwner, D.P. Wilkinson, E.L. Gyenge, Electrochemically Produced Graphene for Microporous Layers in Fuel Cells, *ChemSusChem.* 9 (2016) 1689–1697. <https://doi.org/10.1002/cssc.201600351>.
- [18] G. Lin, T. Van Nguyen, Effect of Thickness and Hydrophobic Polymer Content of the

- Gas Diffusion Layer on Electrode Flooding Level in a PEMFC, *J. Electrochem. Soc.* 152 (2005) A1942. <https://doi.org/10.1149/1.2006487>.
- [19] F.A. Viva, G.A. Olah, G.K.S. Prakash, Characterization of Pt supported on commercial fluorinated carbon as cathode catalysts for Polymer Electrolyte Membrane Fuel Cell, *Int. J. Hydrogen Energy*. 42 (2017) 15054–15063. <https://doi.org/10.1016/j.ijhydene.2017.04.255>.
- [20] J.L. Bott-Neto, T. Asset, F. Maillard, L. Dubau, Y. Ahmad, K. Guérin, S. Berthon-Fabry, A. Mosdale, R. Mosdale, E.A. Ticianelli, M. Chatenet, Utilization of graphitized and fluorinated carbon as platinum nanoparticles supports for application in proton exchange membrane fuel cell cathodes, *J. Power Sources*. 404 (2018) 28–38. <https://doi.org/10.1016/j.jpowsour.2018.10.004>.
- [21] S. Berthon-Fabry, L. Dubau, Y. Ahmad, K. Guerin, M. Chatenet, First Insight into Fluorinated Pt/Carbon Aerogels as More Corrosion-Resistant Electrocatalysts for Proton Exchange Membrane Fuel Cell Cathodes, *Electrocatalysis*. 6 (2015) 521–533. <https://doi.org/10.1007/s12678-015-0267-9>.
- [22] L. Cindrella, A.M. Kannan, J.F. Lin, K. Saminathan, Y. Ho, C.W. Lin, J. Wertz, Gas diffusion layer for proton exchange membrane fuel cells-A review, *J. Power Sources*. 194 (2009) 146–160. <https://doi.org/10.1016/j.jpowsour.2009.04.005>.
- [23] M. Okumura, Z. Noda, J. Matsuda, Y. Tachikawa, M. Nishihara, S.M. Lyth, A. Hayashi, K. Sasaki, Correlating Cathode Microstructure with PEFC Performance Using FIB-SEM and TEM, *J. Electrochem. Soc.* 164 (2017) F928–F934.

<https://doi.org/10.1149/2.0581709jes>.

- [24] M.F. Mathias, J. Roth, J. Fleming, W. Lehnert, Diffusion media materials and characterisation, Handb. Fuel Cells. (2010).  
<https://doi.org/10.1002/9780470974001.f303046>.
- [25] J.I.S.C.P. and board D. of air permeance-G. method J.P. 8117 (1998), GURLEY Method for air permeability.pdf, n.d.
- [26] M. Thommes, K. Kaneko, A. V. Neimark, J.P. Olivier, F. Rodriguez-Reinoso, J. Rouquerol, K.S.W. Sing, Physisorption of gases, with special reference to the evaluation of surface area and pore size distribution (IUPAC Technical Report), Pure Appl. Chem. 87 (2015) 1051–1069. <https://doi.org/10.1515/pac-2014-1117>.
- [27] O. V. Boltalina, T. Nakajima, New Fluorinated Carbons: Fundamentals and Applications Progress in Fluorine Science Series, 2016.  
<https://doi.org/10.1016/C2014-0-04885-X>.
- [28] J.H. Chun, D.H. Jo, S.G. Kim, S.H. Park, C.H. Lee, S.H. Kim, Improvement of the mechanical durability of micro porous layer in a proton exchange membrane fuel cell by elimination of surface cracks, Renew. Energy. 48 (2012) 35–41.  
<https://doi.org/10.1016/j.renene.2012.04.011>.
- [29] G. Thiele, M. Poston, R. Brown, A case study sizing Nanoparticles, 234th ACS Natl. Meet. (2007) 316.
- [30] Sigma-Aldrich, Carbon black., (n.d).  
<https://www.sigmaaldrich.com/JP/en/product/saj/051530>.

- [31] E.T. Mickelson, C.B. Huffman, A.G. Rinzler, R.E. Smalley, R.H. Hauge, J.L. Margrave, Fluorination of single-wall carbon nanotubes, *Chem. Phys. Lett.* 296 (1998) 188–194. [https://doi.org/10.1016/S0009-2614\(98\)01026-4](https://doi.org/10.1016/S0009-2614(98)01026-4).
- [32] G. Nansé, E. Papirer, P. Fioux, F. Moguet, A. Tressaud, Fluorination of carbon blacks: An X-ray photoelectron spectroscopy study: I. A literature review of XPS studies of fluorinated carbons. XPS investigation of some reference compounds, *Carbon N. Y.* 35 (1997) 175–194. [https://doi.org/10.1016/S0008-6223\(96\)00095-4](https://doi.org/10.1016/S0008-6223(96)00095-4).
- [33] N. Watanabe, Y. Kita, O. Mochizuki, Fluorination of carbon black, *Carbon N. Y.* 17 (1979) 359–363. [https://doi.org/10.1016/0008-6223\(79\)90009-5](https://doi.org/10.1016/0008-6223(79)90009-5).
- [34] K. Guérin, M. Dubois, A. Houdayer, A. Hamwi, Applicative performances of fluorinated carbons through fluorination routes: A review, *J. Fluor. Chem.* 134 (2012) 11–17. <https://doi.org/10.1016/j.jfluchem.2011.06.013>.
- [35] K.H. An, J.G. Heo, K.G. Jeon, D.J. Bae, C. Jo, C.W. Yang, C.Y. Park, Y.H. Lee, Y.S. Lee, Y.S. Chung, X-ray photoemission spectroscopy study of fluorinated single-walled carbon nanotubes, *Appl. Phys. Lett.* 80 (2002) 4235–4237. <https://doi.org/10.1063/1.1482801>.
- [36] N. Nonoyama, S. Okazaki, A.Z. Weber, Y. Ikogi, T. Yoshida, Analysis of Oxygen-Transport Diffusion Resistance in Proton-Exchange-Membrane Fuel Cells, *J. Electrochem. Soc.* 158 (2011) B416. <https://doi.org/10.1149/1.3546038>.
- [37] T. Kitahara, H. Nakajima, Microporous layer-coated gas diffusion layer to reduce oxygen transport resistance in a polymer electrolyte fuel cell under high humidity

conditions, Int. J. Hydrogen Energy. 41 (2016) 9547–9555.

<https://doi.org/10.1016/j.ijhydene.2016.04.117>.

## Chapter 5. Summary, Conclusion and Future Outlook

In Chapter 3, we successfully synthesized the fluorinated carbon powders from fluorotelomer alcohols with a unique solvothermal method at 150 °C. Even though the reaction temperature was set to 150 °C, during the reaction a sudden increase in reaction temperature to 345 °C was observed. This indicates that the fluorotelomer precursor and sodium react exothermically. Furthermore, generally solvothermal synthesis of doped carbons is involved with a second heat treatment process. For example, when nitrogen doped carbon is synthesized, first a nitrogen containing alkoxide is produced, which is followed by a pyrolysis process to carbonize the nitrogen containing alkoxide. Similarly for the fluorination of carbon materials, first carbon materials are produced then followed with fluorination at desired fluorination conditions. The proposed solvothermal method in this thesis enables combining these two steps since fluorinated carbon powders are synthesized directly from the precursor without the need for another carbonization or fluorination step. This immensely increases the efficiency of synthesis in terms of duration. Four different types of fluorotelomer alcohol were used to evaluate the effect of different types of fluorotelomer alcohol precursors on chemical and physical properties of the final products. All resulting products had similar microstructures and particle size distribution, regardless of the fluorotelomer precursor used. Each of these products were composed almost entirely of spheroidal nanoparticles with similar structure to that of carbon black. The BET measurement showed that all samples are non-porous with a very low specific surface area around 25 m<sup>2</sup>/g. A chemical structure analysis of the final product was investigated with various techniques. Interestingly, four synthesized fluorinated carbon black products consisted of covalently bonded carbon-

fluorine atoms. It was found that the fluorine content of the final product changes depending on the chain length of the fluorotelomer alcohol precursor. Having the fluorotelomer alcohol with a longer chain in the synthesis means having higher fluorine content in the final product. The fluorine content of the sample changes from around 5 at.% to approximately 10 at.%, depending on the used fluorotelomer precursor. Surprisingly, a highly graphitic structure was detected in the synthesized fluorinated carbons by XRD, Raman Spectroscopy, TEM, and SAED techniques. Since there were no catalyst nor high temperature involved to form graphitic structure, a new catalytic effect of HF was proposed for the formation of graphitic structure. Furthermore, the effect of the fluorination on the graphitic structure of the material was investigated. To investigate this effect, fluorinated carbon materials were defluorinated with a thermal annealing step at 700 °C under an inert atmosphere. It was found that heat treatment at elevated temperatures, preferably over 650 °C, is an effective method for defluorination of the carbon materials. It was detected that after defluorination the defect in the graphitic structure decreased considerably. It is concluded that fluorination increases the defective structure in the graphitic domain of carbon due to the  $sp^3$  bonding of fluorine to carbon atoms. Finally, the hydrophobicity of the synthesized fluorinated carbon powders was investigated with the WCA measurements. It was found that with an increase of fluorine content in the material, the hydrophobicity increases and with the defluorination the samples became hydrophilic. All fluorinated samples showed superhydrophobicity (i.e.,  $>150^\circ$ ).

In Chapter 4, we discussed the application of the superhydrophobic fluorinated carbon powder as MPL material with the focus of increasing water drainage rate during high current density PEFC operation conditions at low PTFE binder content (i.e., 5 wt.%). To evaluate

the effectiveness of the synthesized fluorinated carbons as MPL material, we compared it with a graphitized carbon black powder which has similar structural properties. MPLs were coated onto GDLs with a doctor blade method and the thickness of the MPLs was set to 35  $\mu\text{m}$ . The WCA measurement results showed that fluorinated carbon black based MPL's (FC-MPL) water contact angle was  $151^\circ$ , whereas that of carbon black based MPL (CB-MPL) was  $131^\circ$ . WCA measurement results indicated the superior hydrophobicity of the fluorinated carbon black based MPL. Physical characteristics such as porosity and maximum pore size of the MPLs were also investigated. To evaluate and compare the porosity of the MPLs, free standing MPLs were manufactured with the direct coating of MPL slurry onto glass plates. The porosity of the CB-MPL was calculated to be 83% whilst FC-MPL had a 76% porosity. Meanwhile, the maximum pore size of the MPLs were measured to be similar at 40.5 and 42.5  $\mu\text{m}$  in diameter for CB-MPL and FC-MPL respectively. It is assumed that due to the lower porosity i.e., higher tortuosity, FC-MPL had lower air permeability ( $2.78 \times 10^{-13}$ ) compared to CB-MPL ( $3.86 \times 10^{-13}$ ). Furthermore, oxygen transport resistance (OTR) tests were conducted to evaluate and compare MPLs' oxygen diffusivity under high relative humidity conditions (80, 100 and 120%) with an in situ PEFC test at 45  $^\circ\text{C}$  and 80  $^\circ\text{C}$  cell temperatures. The results clearly showed that the FC-MPL has a significantly lower OTR compared to CB-MPL. This can be directly attributed to the superhydrophobic nature of the FC-MPL. Finally, PEFCs were fabricated incorporating the FC-MPL, and compared to identically prepared cells using the CB-MPL at cell temperatures of 45  $^\circ\text{C}$  and 80  $^\circ\text{C}$ . At 45  $^\circ\text{C}$ , the performance of the cell was measured at 80, 100 and 120 % RH, whilst at 80  $^\circ\text{C}$  the cell was measured at 80 and 100 % RH. In all cases, the FC-MPL showed a higher limiting current density due to its superior water repellent properties. Furthermore, since fluorine is

the most electronegative element on the periodic table, the effect of the fluorine content on the conductivity of the MPLs were investigated. Results showed that there are no significant changes in the ohmic region of the polarization curves. This may be because the fluorine atoms are mainly concentrated at the surface of the carbon particles rather than throughout the bulk.

Overall, this thesis provides significant insights into fluorinated carbon synthesis and its application as MPL material for improved water management to increase PEFC performance.

We will further investigate the usage of uniquely synthesized superhydrophobic fluorinated carbons in PEFCs in future outlook. As fluorinated carbons are generally corrosion resistant, we will further investigate fluorinated carbon based MPL with the focus on a corrosion resistance material for MPLs to improve corrosion problem in the MPL structures. The use of this superhydrophobic fluorinated carbon will then be investigated as platinum support to mitigate the carbon corrosion problem in the catalyst layer of the PEFC and polymer electrolyte water electrolysis (PEWE).